INTERGRANULAR STRESS CORROSION CRACKING

OF

SENSITISED AUSTENITIC STAINLESS STEEL

A Thesis Submitted for the Degree of Doctor of Philosophy of the
University of London

Department of Metallurgy
and Materials Science
Royal School of Mines
Imperial College of Science
and Technology

M.G. Lackey

October, 1980

TO MY PARENTS

CONTENTS

ABSTRACT

The objective of this investigation was to determine the possible mechanism(s) of intergranular stress corrosion cracking in sensitised type 304 stainless steel. As the mechanism of SCC has been shown to be hydrogen embrittlement in a variety of metal-environment systems, it was necessary to extend this work to consider the effect of hydrogen on the material. This project encompasses three major areas of research: 1) the characterisation of the sensitisation process; 2) intergranular stress corrosion cracking of the sensitised steel; and 3) to determine the effect of hydrogen on the behaviour of the steel.

Transmission electron microscopy and quantitative microanalysis were employed to examine the sensitised microstructure. Using STEM quantitative microanalytical techniques, the extent of the Cr-depleted zone was experimentally verified. The effects of such variables as temperature and time of sensitisation were also investigated. Preferential formation of martensite was found to be a consequence of the local Cr content. Microanalysis of grain boundary regions provided additional information regarding the nature of the precipitation of $(Cr,Fe)_{23}C_6$ carbides.

The stress corrosion behaviour of sensitised 304 was evaluated through slow strain rate tests conducted in dilute H_2SO_4 + NaCl solutions at room temperature under free corrosion conditions or under potential control. As the emphasis of this investigation was on the morphology of SCC, extensive use was made of electron optical techniques(TEM, HVEM, STEM, SEM). Fractographic examination of stress corroded specimens revealed regions of intergranular and cleavage-like fracture. From the controlled potential tests, this cleavage-like fracture was

found to be associated with hydrogen embrittlement. Specimens polarised anodically exhibited striation-like markings over the entire fracture surface, unequivocally proving the discontinuous nature of crack propagation in this system. Unambiguous interpretation of the mode of crack propagation was provided through the technique of matching opposite fracture surfaces.

The final aspect of this research concerned the effect of hydrogen on the microstructure and properties of sensitised 304. Although laboratory tests conducted in high temperature (340^oC) dry steam were unsuccessful, the existence of a "pre-exposure" effect in sensitised austenitic stainless steel can not be totally dismissed. The effect of a hydrogen-bearing environment (He-H_2O vapour @ 25^oC) was also examined in the Gas Reaction Cell of the HVEM. Similarly, no reaction was observed in deformed or undeformed specimens. Cathodically charging the specimens with hydrogen did promote microstructural changes. The stresses involved in the process of introducing hydrogen into the metal were sufficient to cause significant deformation and induce the $\gamma \rightarrow \varepsilon + \alpha'$ transformation (especially in the vicinity of grain boundaries).

The results of this project indicate that the phenomenon of IGSCC in dilute H_2SO_4 + NaCl solutions is a manifestation of hydrogen embrittlement.

CHAPTER 1

REVIEW OF THE LITERATURE

1.1 STRESS CORROSION CRACKING

Stress corrosion cracking is a technologically important failure process. It is a phenomenon which occurs only under the simultaneous action of stress and environment, and is characterised by brittle delayed fracture. The fracture mode may be transgranular, intergranular or mixed. A multitude of metals in various environments are susceptible to SCC. Although there is an extensive accumulation of observation and data regarding this phenomenon, no single mechanism has been established which adequately explains the phenomenon of SCC in all systems.

A commonly cited parameter for conveying SCC, data in early investigations was 'time to failure' (TTF) for specimens. This enabled very broad comparisons of SCC behaviour to be made, but it was necessary to acquire more quantitative data regarding the cracking process for mechanistic studies. The TTF value includes the crack initiation and propagation stages. Due to the difficulty in detecting crack initiation, it is usually impossible to distinguish between the two stages. During the "incubation period" for SCC, initiation of the crack is proposed to occur at breaks in the oxide film or by pitting. The growth of SC cracks may be monitored optically or through the use of back face strain gauges. In this way, a value of the crack velocity may be obtained. Observed SCC propagation rates range from 10^{-12} m/sec to 10^{-1} m/sec depending on the metal/environment system.

Much information regarding crack morphology and propagation has been provided through microstructural and fractographic examinations of SCC. No investigation can be complete without a visual inspection of the specimen. A wide range of tools available (optical microscope, CEM, STEM, SEM, HVEM) has been successfully employed in mechanistic studies. The fine distinction between crack initiation and propagation, and details of the initiation process itself can be obtained by careful examination of thin specimens exposed to stress corrosive environments.

In this review of the literature, it is proposed to summarise important parameters in the stress corrosion cracking of Fe-Ni-Cr alloys, specifically, Type 304 stainless steel.

1.2 SOME PHYSICAL METALLURGICAL ASPECTS OF AUSTENITIC STAINLESS STEELS

In order to investigate the stress corrosion failure of austenitic stainless steels, it is important to consider the physical metallurgy of these materials. An excellent review of the physical metallurgy of Fe-Ni-Cr alloys - with particular attention to its influence on the SCC and hydrogen embrittlement behaviour - has been compiled by Gordon (1). The major factors which will be considered in this section include compositional effects, and the martensite transformation.

1.2.1 Alloy Composition

Elements present in austenitic steels can be classified in terms of their effect on the stability of the austenite. Also, various additions are made to impart desired properties such as resistance to corrosive attack and good mechanical properties.

Chromium additions of ∿ 14 wt% are required for corrosion resistance of stainless steels. Chromium contents in excess of 14% lead to a drastic decrease in the dissolution rate of the material by promoting the formation of a chromium rich oxide film (25-50Å thick) on the alloy surface, thus isolating it from the environment. This passive film will not form if the chromium content is less than ∿ 12wt %.

These additions of chromium stabilise the ferrite phase in iron alloys. Therefore Ni is added to the alloy as an austenite stabiliser, for, in the presence of carbon (an extremely effective austenite stabiliser), 8 wt % Ni can produce a stable austenite phase at 25°C. This is the basis for the 18-8 class of austenitic stainless steels. Nickel is also useful in improving the high temperature strength of these steels.

Other additions to the Fe-Ni-Cr alloys include manganese, nitrogen, molybdenum, and silicon. Mn and N act as austenite stabilisers, while the effect of Mo and Si is additive to that of Cr in stabilising the bcc structure.

1.2.2 Martensite

1.2.2a α' Martensite

Most commercial austenitic stainless steels are metastable at ambient temperatures, transforming to α' martensite (bct) at very low temperatures (M_s). Deformation or strain-induced martensite, however, will form at substantially higher temperatures (M_d).

Four types of α' martensite have been reported in the literature: lath, plate, surface, and massive (1). It is agreed, however, that surface and massive martensites are actually special forms of lath martensite (2). Lath martensite is usually observed in low carbon Fe-Ni-Cr alloys, and for chromium contents of approximately $\sim$ 10 to 16 wt % (3). This type of martensite contains a high dislocation density, but no regular substructure. The habit plane has been reported to be $\sim \{225\}$ (4). Plate martensite is favoured by high carbon contents, low chromium contents ($< \sim$ 7 wt % Cr), and nickel concentration of $\sim$22 to 35 wt.%. The martensite plates are internally twinned.

Martensite may exhibit a Kurdjimov-Sachs ($(111)_\gamma \| (011)_{\alpha'}$ and $[\bar{1}01]_\gamma \| [\bar{1}11]_{\alpha'}$, or a Nishiyama-Wassermann ($(011)_{bcc} \| (1\bar{1}\bar{1})_{fcc}$ and $[100]_{bcc} \| [110]_{fcc}$) orientation relationship with the austenite.

1.2.2b ε Martensite

ε martensite is an hcp structure which forms in Fe-Ni-Cr austenites upon cooling or deformation. It has been described as regularly faulted austenite. As the stacking fault energy of the austenite is decreased, ε formation is enhanced. Mangonon (5) demonstrated that ε is an intermediate stage in the $\gamma \rightarrow \alpha'$ transformation. Lath type α' martensite was observed to nucleate preferentially at the intersection of two ε bands. The ε transformation mechanism is proposed to be pure shear in the $(111)_\gamma$ plane (6). The orientation relationship of the ε with the parent γ and α' is:

$$(111)_\gamma \,||\, (0001)_\varepsilon \,||\, (101)_{\alpha'}$$

$$[110]_\gamma \,||\, [1210]_\varepsilon \,||\, [111]_{\alpha'}$$

1.3 IMPORTANT PARAMETERS IN SCC

1.3.1 Microstructure

Microstructure has a pronounced effect on the corrosion behaviour of austenitic stainless steel. Through thermomechanical processing, microstructures may be developed which are either relatively passive or extremely susceptible to SCC, particularly intergranular stress corrosion. In the solution annealed (and quenched) condition, austenitic steels are susceptible to transgranular SCC, and, in certain oxidising environments, intergranular corrosion. Stress-relief anneals, however, can result in the formation of a very susceptible or a rather resistant microstructure.

1.3.1a Sensitisation

Heat treating of austenitic stainless steels in the temperature range 500°C-800°C results in precipitation of chromium carbides ($M_{23}C_6$ type) along the grain boundaries.

In this condition, austenitic steels are extremely susceptible to intergranular corrosion and intergranular stress corrosion cracking. The term "sensitisation" is used to describe this microstructural condition and accompanying loss of corrosion resistance.

The carbon content of the steel is the most significant factor in determining the degree of sensitisation and ultimate susceptibility to intergranular attack (7). Susceptibility to sensitisation is increased by nickel additions, and decreased by molybdenum and chromium. Nb and Ti additions decrease the degree of sensitisation by reducing the amount of $Cr_{23}C_6$ precipitation.

It has been reported in the literature that continuous grain boundary carbides are formed during sensitis This had been questioned by other investigators (8) who observed discrete chromium carbides along the grain boundaries. Mahla and Niel sensitisation (7). a bromine-methanol technique for the chemical separation of the carbides in sensitised steel. They observed that the carbides had nucleated in the grain boundaries, but grew into adjacent grains. The carbides initially had pronounced dendritic shapes, but, if sufficient time was allowed, these carbides would acquire regular geometrical shapes. The work of Stickler and Vinckier (10) on sensitised type 304 steel confirmed Mahla and Nielsen's results. Cihal and Kasova (11) characterised the morphology of the chromium carbides formed in type 304 steel. Elongated plate and needle-like carbides were observed to precipitate on incoherent twin boundaries, and spatially developed arrays of carbides were formed on high angle grain boundaries. Younger et al. (12) observed that the grain boundary carbides ($M_{23}C_6$) had a crystallographic relationship with one of the adjacent austenite grains. The carbides are actually semi-coherent with the austenite; their lattice parameter being three times that of the austenite. It has also been determined that the composition of the carbides is approximately $(Cr_{.7-.8}Fe_{.2-.3})_{23}C_6$.

Sensitised microstructures are generally reported to promote intergranular failures. Several investigators, however, have observed no difference in the SCC behaviour of sensitised and non-sensitised austenitic stainless steels. Denhard (13) noted transgranular cracking in annealed and sensitised type 304 steel during SCC testing in 154°C $MgCl_2$ solutions. Similar observations regarding SCC of austenitic steels were obtained by Hänninen (14). Intergranular fracture of sensitised steel specimens was always observed by Berry and co-workers (15) in their study of the effect of oxygen in SCC. They concluded that the occurrence of intergranular fracture was irrespective of the type of sensitisation treatment. A similar observation was reported by Theus and Cels (16) as a result of their examination of intergranular SCC in F^- solutions. Hishida and Nakada (17), investigating the effect of Cl^- in the SCC of type 304 steel in high temperature H_2O, concluded that the change in the observed fracture mode was dependent upon the degree of sensitisation and Cl^- concentration. Kowaka (18) has reported that the potential range for intergranular SCC exists below that for transgranular SCC. This range becomes wider as the concentration of $MgCl_2$ (test solution examined) decreases, and as the temperature decreases. The coexistence of transgranular and intergranular cracks in sensitised stress corroded specimens suggests that there may be a critical combination of environmental and material effects which determine what fracture mode will predominate (19).

1.3.1b Stabilisation

The presence of carbides along grain boundaries in austenitic stainless steel does not necessarily indicate that the material is susceptible to intergranular attack. It is possible to modify the nature of the chromium depleted zone so that the material will be immune to grain boundary corrosion. This can be accomplished by an ageing treatment in the temperature range 850°C ∿ 950°C known as stabilisation. The precipitates which form in this temperature range tend to be large, discrete particles.

The difference in the corrosion behaviour between the stabilised and sensitised steels has been attributed to the elimination of the chromium depleted zone due to the high diffusivity of Cr at these temperatures. Prolonged anneals (several hundred hours to several years) in the sensitising temperature range are necessary before the susceptible material may be "desensitised". This method of desensitisation is also concerned with increasing the chromium content in the grain boundary region.

1.3.2 Alloy Composition

Frequent attempts have been made to improve the SCC resistance of austenitic stainless steels by compositional modifications. The major alloying elements examined towards this goal have included Ni, Mn, P and Cr.

Nickel has been reported to be the mose effective alloying addition for inhibiting SCC in chloride environments (20). It has been observed, however, that small Ni additions to Fe-Cr alloys, which were immune to SCC, resulted in SCC susceptibility (13). By increasing the Ni content, alloys exhibited more resistance to caustic SCC (21).

Although manganese is used to replace Ni in certain austenitic steels (AISI 200 series), its effect on SCC susceptibility is detrimental rather than additive to that of Ni (particularly for Mn contents greater than 5 wt.%).

Other elements which are deleterious to SCC resistance include nitrogen, phosphorous, sulphur, and the Group V-A elements. The role of N is thought to be associated with its effect on the repassivation kinetics of the steel (21). It has been shown that P increases the rate of hydrogen evolution at clean steel surfaces (22). Staehle et al (23) observed crystallographic dissolution of P-containing thin-foil specimens, and postulated that the effect of P was to promote hydrogen entry into the metal by preventing the hydrogen recombination step.

Chromium and molybdenum have variable effects on SCC resistance (24). Chromium contents less than $\sim$15wt.% and greater than $\sim$25wt.% were found to be beneficial. Similarly, additions of Mo greater than $\sim$5wt.% improved resistance to SCC. The effects of these elements on the SCC behaviour of Fe-Ni-Cr alloys is dependent upon the nature of the stress corrosive environment.

The effects of Ni, Mn, Mo, Ti and C on SCC have been interpreted in terms of their influence on the stacking fault energy (SFE) and dislocation coplanarity (25). Swann (26) suggested that a increase in dislocation coplanarity and a decrease in SFE enhanced susceptibility to SCC in austenitic stainless steels. This correlation, however, is inapplicable for Si and N (27).

1.3.3 Stress

Without the presence of a tensile stress, SCC will not occur. Therefore, it is essential to determine the role of stress in this phenomenon. Failure times in SCC tests are decreased as the applied tensile stress increases. It is believed that the growth rates of stress corrosion cracks are controlled by the crack tip stress intensity rather than the applied stress.

A rather standard method of presenting kinetic SCC data is through the use of crack velocity vs. stress intensity (V-K) curves, (Figure 1.1)(28). Three distinct regions can be defined in this diagram. In the first stage (I), the crack tends to propagate so that its plane remains ∿90° to the tensile axis. The crack growth rate is nearly independent of stress intensity in stage II, and it is possible that crack branching may occur. The crack velocity then increases with increasing K in stage III until K_{I_C} is reached and the specimen fractures.

It has been reported that a threshold stress exists for SCC, but this has been the subject of much discussion (29, 30). Standard techniques have been employed to

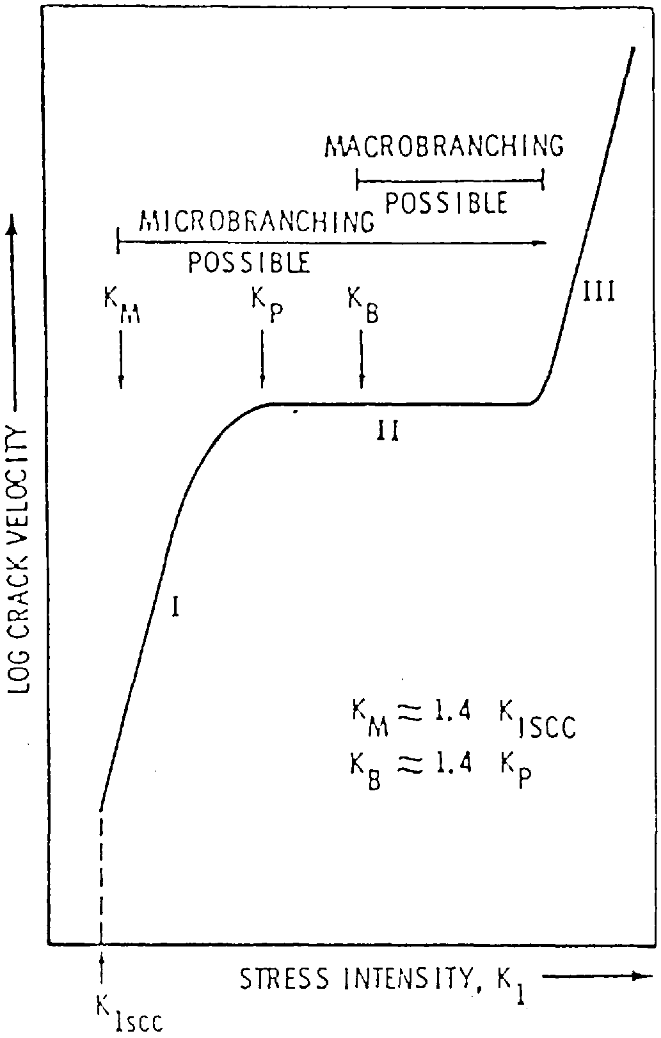

Figure 1.1 Schematic Representation of the Effect of Stress Intensity on Stress Corrosion Crack Velocity, Microbranching, and Macrobranching. (from ref.28)

determine the $K_{I_{SCC}}$ value (31). The observation that SCC can occur in the absence of an applied tensile stress prompted investigations into the role of residual stresses in the material, and stresses which are induced by corrosion product. Stresses which were considerable fractions of the yield stress resulting from the accumulation of corrosion product had been detected by Pickering, Beck and Fontana (32).

A comparison of SCC and deformation behaviour of various alloys indicates that properties which increase susceptibility to SCC also promote coarse slip. Plastic deformation results in the formation of long active slip bands, and slip steps at the surface. The precise role of slip processes in SCC is unclear,. but several theories have been proposed (these will be discussed in Section 1.4). Silcock and Swann (33) examined SCC initiation in single crystals of austenitic stainless steels in boiling $MgCl_2$ solutions. Preferential attack and crack nucleation was observed at emergent edge dislocations. The rate of slip step formation had a pronounced effect on crack nucleation, but not all crack nuclei were found to develop from corroded slip-steps.

Honkasalo and Hänninen (34) have demonstrated that the cleavage-like fracture morphology produced during SCC of type 304 steel in boiling $MgCl_2$ is not related to the slip planes. They also observed preferential dissolution of slip planes and α' martensite in stress corroded material after immersion in acidic solution (simulating the crack tip environment).

1.3.4 Environment

Numerous parameters are involved in the examination of environmental effects on SCC. It is often difficult to isolate specific factors for a precise investigation. The effect of major environmental variables in the process of SCC will be briefly summarised.

1.3.4a Temperature

General observations from stress corrosion cracking studies indicate that cracking is enhanced by increased temperatures

1.3.4b Solution Composition

It is well-documented that stress corrosion occurs in chloride environments. A widely reported observation is that failure times in SCC tests decrease as the Cl^- concentration increases. The chloride ion concentration, however, is not the only factor which is important in SCC. Rhodes (35) observed that no SCC occurred in anhydrous $AlCl_3$, KCl, and $FeCl_3$ melts. This implies that H_2O is critical in the SCC of austenitic stainless steels in that it provides a readily reducible species (H^+ or O_2). The role of Cl^- has been postulated to involve the local destruction of passive surface films, and the retardation of their formation. Through radioactive tracer studies, chloride ions have been observed to accumulate at highly stressed regions (36).

The most commonly used solutions for evaluating SCC susceptibility include boiling $MgCl_2$ and boiling LiCl. In order to simulate real operating environments (particularly nuclear reactor cooling water), the stress corrosion behaviour has also been investigated in high temperature water (200°C to 374°C) with chloride contents ranging from 0.01 ppm to 1000 ppm Cl^- and varying O_2 contents. Increasing the Cl^- or O concentration promotes stress corrosion, especially for sensitised steels (21). The effect of dissolved oxygen in solution on the SCC behaviour of austenitic stainless steels is significant. Berry and co-workers (15) noted that increasing the dissolved oxygen content promoted cracking. Similar conclusions were drawn by Clarke and Gordon (37) in their investigation of heavily sensitised Type 304 steel. Intergranular SCC was enhanced for O contents greater than 0.1 ppm in slow strain rate tests (29,38). The effect of oxygen is electrochemical in that its presence has been related to a shift in the corrosion potential to more positive values.

The effect of Cl^- on SCC is not shared by the other halides. Louthan (39) did not observe SCC in iodide environments, but SCC was found to occur in $MgBr_2$ solutions - at a much reduced rate (35). Intergranular SCC has been observed in sensitised austenitic stainless steels in F^- - bearing environments (40,41). This occurs at room temperature, and at low F^- concentrations (1-10 ppm).

Intergranular SCC can also be promoted by low (<10 ppm) concentrations of sulphate ions, and inhibited by high SO_4^{-2} contents (29).

1.3.4c pH

SCC (predominantly initiation) can be accelerated by reducing the pH of the test solution. It is important to realise that bulk solution conditions are not identical to those existing in the highly localised crack tip environment. The pH of the solution at the crack tip is independent of that of the bulk solution. This has been demonstrated by Sandoz et al.(42) for a variety of alloy steels in 3.5% NaCl solution (pH=6). A crack tip pH of ∿3.5 was measured using indicator papers. The acidity of the crack tip was confirmed by Baker et al.(43) and Suzuki et al.(44), reporting values of ∿1.5, and -0.13 respectively in austenitic stainless steel. Suzuki et al.(44) quantitatively analysed the solution within pits in Type 316L and 304L steels in 0.5N NaCl at 70°C. In the active condition, they observed pH values from -0.13 to 0.8 with corresponding chloride concentrations of 3.78 to 6.47N. They explained the low pH values by the presence of hydroxy-chloro complexes of dissolved metal ions, and the high concentration of chlorides.

The presence of an oxide film on the internal crack surfaces led Baker et al.(43) to postulate that this film was the result of metal ion - oxide hydrolysis:

$$2\ Cr^{+2} + 3H_2O \rightleftarrows Cr_2O_3 + 6H^+$$

A low pH in the crack tip region can be maintained, and the H^+ will be reduced at cathodic areas away from the tip. The observation of Wilde (45) that the Cr content of $MgCl_2$ solution after SCC tests was significantly lower than that based on the corrosion of the alloy tends to support the proposed hydrolysis reaction.

1.3.5 Surface Films

Generally, materials susceptible to SCC are known to form surface films. The presence of a pssive film on austenitic stainless steel in aggressive environments is the reason for its good corrosion resistance. The nature of the protective films which form on stainless steels in hot chloride environments (SCC test environments) has been the topic of considerable research (45-49).

Rockel and Staehle (49) have observed that nickel was preferentially depleted from the surface of type 304 stainless steel when exposed to 154°C $MgCl_2$ solution. The surface film on exposed stainless steel is composed of corrosion product rather than Ni (49). Shimodaira (47) detected CrOOH, but no Ni or Fe compounds on the surface of austenitic steel in boiling $MgCl_2$ solution. Szklarska-Smialowska and Lukomski (48) employed AES to determine the composition of the surface films formed on type 304 steel in Cl^- media. It was observed that the film contained Fe, Cl, O and S, and was enriched in Cr.

When steel is immersed in boiling $MgCl_2$ solution, the open circuit potential is known to drift (45). Due to film formation, a transition has been observed to occur from a maximum value of the anodic current density to smaller residual current densities. Numerous investigations have shown that the film formed on stainless steels during exposure to stress corrosive environments changes in composition and passivity (45,49). It is most probable that these changes are important in stress corrosion cracking.

1.3.6 Electrochemistry and Hydrogen

Numerous observations regarding the electrochemical nature of stress corrosion cracking have been reported. Measurement of the corrosion potential vs. time of stress corroding specimens have shown that SCC is accompanied by a shift in potential (50). The specimen potential varies from an active value to a more noble potential where it reaches a maximum before returning to an active state, as the specimen fails. This behaviour has been attributed to various stages of the SCC process.

It is well-known that stress corrosion cracking can be reduced or inhibited by the application of a cathodic current (50,51). Cathodic protection (polarisation) involves reducing the value of the mixed corrosion potential of the specimen to the reversible potential of the anodic reaction (Figure 1.2) (52). It is possible that there will still be a small degree of corrosion during cathodic polarisation. This technique has been successfully employed on alloys susceptible to SCC.

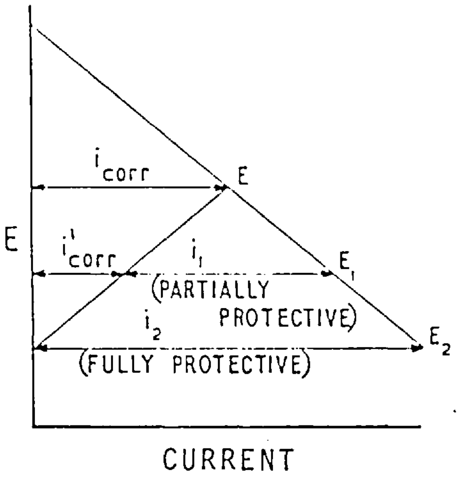

Figure 1.2 Cathodic Protection. Applied cathodic current i_1 reduces the corrosion rate from i_{corr} to i'_{corr} partially protecting the metal, while applied cathodic current i_2 produces complete protection. (from Scully, ref.52)

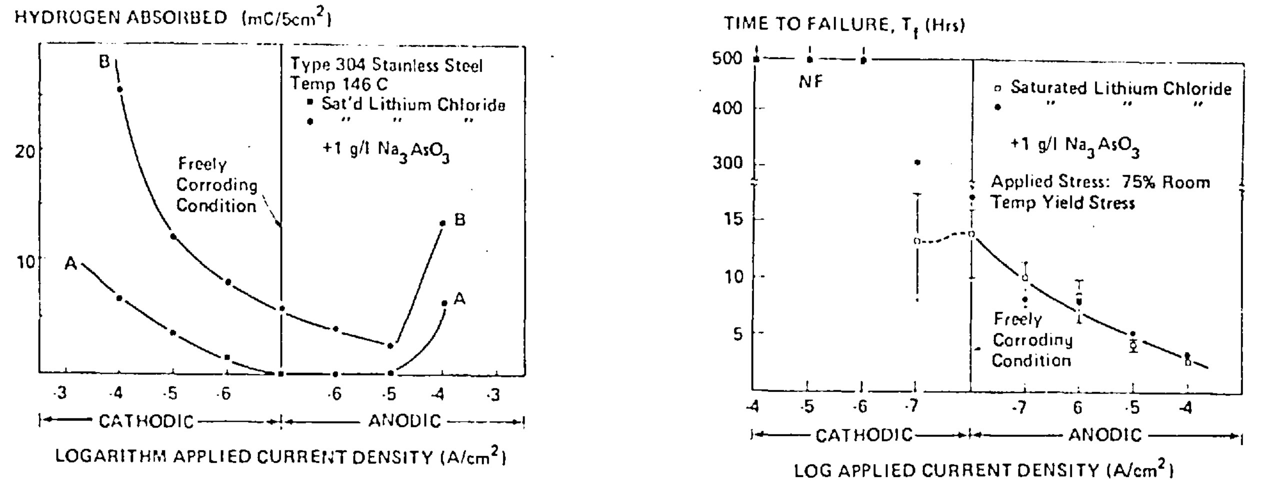

The influence of applied current on the degree of hydrogen absorption into Type 304 stainless steel in lithium chloride solutions at 146 C.

The effect of applied current on the stress corrosion cracking behavior of Type 304 stainless steel in lithium chloride solutions at 146 C.

Figure 1.3 The Experimental Results of Wilde and Kim(57) Which Demonstrate the Effect of Applied Potential on H-absorption and SCC in LiCl.

The application of anodic polarisation, however, will enhance cracking due to anodic dissolution. Anodically polarised specimens exhibit reduced crack initiation periods and an increased density of cracks (52).

In SCC of austenitic stainless steels, hydrogen ion reduction is agreed to be the primary cathodic reaction. During cathodic polarisation, the increased rates of H_2 evolution have been attributed to the presence of an adsorbed species on the surface. It is believed that substantial cathodic potentials are required to bias the competitive adsorption process in favour of hydrogen to result in desorption of the anions. Shively et al.(53) have demonstrated conclusively that hydrogen can be absorbed by austenitic stainless steel when held under anodic polarisation. It was also observed by Barth, Steigerwald and Troiano (54) that hydrogen could be evolved from SC cracks, and that hydrogen could also enter martensitic steels during anodic polarisation. Dix (55) has studied the entry of hydrogen into steel under free corrosion conditions. Barth and Troiano (56) examined the cathodic protection phenomenon and SCC with respect to the effect of oxygen, and observed that the presence of oxygen inhibited hydrogen absorption at low to moderate cathodic overvoltages (the range employed for cathodic protection). In anodically polarised specimens, hydrogen permeation only occurred when oxygen was present. Results of SCC tests indicated that the extended failure times generally associated with cathodic protection were directly related to the presence of oxygen in the solution, as the removal of oxygen completely eliminated any indication of cathodic protection. The SCC failures were directly related to the presence of hydrogen.

The question regarding the role of hydrogen in hot chloride SCC of austenitic stainless steel prompted Wilde and Kim (57) to investigate hydrogen absorption during SCC in boiling (146°C) LiCl solutions. They had previously demonstrated that at potentials more noble to the reversible hydrogen potential, the oxidation of absorbed H in steels occurs and produces an increase in the applied current (under potentiostatic conditions) (58). By comparing the number of coulombs passed to achieve a steady-state passive current density (at 0.1 V SCE in 1N H_2SO_4) for specimens tested in boiling LiCl (with and without a hydrogen recombination poison - 1g/l Na_3AsO_3), they concluded that more hydrogen was absorbed in the presence of the poison under anodic and cathodic conditions. The effect of absorbed H on the SCC behaviour was also evaluated by conducting tests under potential control in the LiCl solutions. The results of the H-absorption and SCC experiments are presented in Figure 1.3. The conclusion drawn by Wilde and Kim from this investigation was that hydrogen was not involved in the mechanism of SCC in hot chloride solutions.

Wilde and Kim's experiments clearly show that SCC is inhibited by the application of a cathodic current, and is accelerated under anodic conditions. The absorbed H content apparently has no effect on the time to failure of the stress corroding specimens. The conclusions of Wilde and Kim, however, are only valid when discussing the mechanism of crack initiation, not propagation. By adding a hydrogen recombination poison to the LiCl solution, hydrogen absorption is increased and, importantly, no local anodic sites can develop on the specimens surface. These local anodes are essential for the initiation of SCC (59). Therefore, it is impossible for the stress corrosion cracks to develope.

The observation that no hydrogen was absorbed under free corrosion conditions in type 304 steel does not necessarily eliminate a hydrogen embrittlement mechanism of SCC. Wilde (45) has demonstrated that type 304 steel in boiling LiCl solution is in the passive state. As oxide films have been shown to greatly reduce hydrogen penetration into austenitic stainless steels (60), it is not surprising that no absorbed hydrogen was detected. In stress corrosion cracking, the passive film would be broken due to either emergent slip steps or strain in the film itself. Once the film is cracked, hydrogen could enter the metal. These results give no indication of the possible role of hydrogen during crack propagation.

The conclusions of Wilde and Kim (56) are only applicable to crack initiation. The importance of dissolution in crack initiation has been demonstrated by several detailed investigations (14,33,61,62,63).

1.4 THEORIES OF STRESS CORROSION CRACKING

Any mechanism of stress corrosion cracking must explain all of the observation concerning this phenomenon. Numerous theories have been proposed, yet no single theory has been able to rationalise all of the documented observations for this type of failure. Basically, there are two categories of SCC theories: 1) active path models; and 2) mechanical/embrittlement models. Active path cracking encompasses those theories which rely on anodic dissolution at the crack tip for crack propagation, such as stress-accelerated corrosion, strain-enhanced corrosion, and slip dissolution. Corrosion product wedging, adsorption-induced cleavage, strain-induced transformation, and hydrogen embrittlement belong to the second group of SCC mechanisms. These models were postulated and developed with the intention of explaining the phenomenon of SCC in all materials, and shall be reviewed in this context. It is essential to remember, however, that it possible for more than one mechanism to operate during SCC.

In this section, the 'active path' and mechanical models will be considered. Hydrogen embrittlement will be discussed in Section 1.5.

1.4.1 Stress-Assisted Localised Corrosion

By definition, stress corrosion cracking involves the simultaneous action of stress and a potentially aggressive environment. Separation of stress and environmental effects may possibly offer insight into the mechanism(s) of stress corrosion cracking.

It is believed by some investigators that SCC is actually stress-assisted localised corrosion. The tensile stress merely accelerates the mechanical failure of corroding material. As is the case with SCC, austenitic stainless steel is susceptible to intergranular corrosion when sensitised, but is immune in the stabilised condition. This suggests that the microstructure developed during the sensitising heat treatment imparts susceptibility. Three major theories have been proposed to explain this type of localised attack: 1) Chromium Depletion Theory; 2) Noble Carbide Theory; and 3) Solute Segregation Theory.

1.4.1a Chromium Depletion Theory

In 1933, Bain et al (64) devised a model to explain the poor corrosion resistance of sensitised stainless steels. They proposed that the susceptibility of the material to intergranular corrosion was the result of a chromium depleted zone which had formed in the regions adjacent to the intergranular chromium carbides. A major assumption in this model is that a minimum chromium content of approximately 12% is required for passive film formation. During the sensitisation treatment, chromium-rich carbides from along the grain boundary and locally deplete the austenite of chromium. Bulk diffusion of chromium from the matrix is too sluggish to permit replenishment in these zones, so the local chromium content falls to a value less than that necessary to form a protective film, and the intergranular zones corrode preferentially.

Two excellent theoretical treatments of the Chromium Depletion Theory of intergranular corrosion have been presented by Stäwstrom and Hillert (65) and Tedmon et al (66). Stäwstrom and Hillert derived a diffusion-controlled model which considered grain boundary precipitation, and the formation and development of the chromium depleted zone. They assumed that the Cr content in the region adjacent to the carbide is thermodynamically determined by the alloy-C-$M_{23}C_6$ local equilibrium. It was shown that, for short sensitisation times, the minimum Cr content of the zone was dependent upon the carbon content of the steel and the annealing temperature. They predict that desensitisation (the elimination of the depleted zone by Cr diffusion from the matrix observed after long term anneals) should occur simultaneously with gradual precipitation of carbide. These calculations are in close agreement with previously published observations on the intergranular corrosion of sensitised and desensitised austenitic stainless steels.

Tedmon and co-workers presented a similar but more general model. Unlike the Stäwstrom and Hillert analysis, Tedmon et al did not assume a uniform chromium composition between grain boundary carbides. Through a thermodynamic analysis, the Cr concentration in a grain boundary could be calculated as a function of distance from the carbide. It was shown that a chromium concentration gradient exists between carbides within a grain boundary, so that under certain conditions a grain boundary may not be uniformly sensitised. Continuous carbide precipitation along the boundary is unnecessary for complete sensitisation. This analysis was also confirmed experimentally through the intergranular corrosion of thin film specimens. It was observed that the carbides themselves were inert to corrosion attack, and that non-uniform attack occurred along grain boundaries.

Numerous observations have been reported which indirectly support the Chromium Depletion Theory, but only since the advent of STEM-EDX microanalysis has it been experimentally possible to detect Cr-depleted zones.

1.4.1b Noble Carbide Theory

An electrochemical theory of intergranular corrosion of sensitised austenitic steel was proposed by Stickler and Vinckier (67). They postulated that the corrosion process is an electrochemical reaction between the carbide particles and the matrix which proceeds rapidly along the grain boundaries where there is a path of continuous chromium carbides. The presence of a Cr-depleted zone is not considered in this theory.

Two significant experimental observations invalidate the noble carbide theory. Firstly, it has been demonstrated that stabilised austenitic stainless steel with continuous grain boundary precipitates is immune to intergranular attack. Also Tedmon et al's (66) thin foil observations of patchy intergranular corrosion is sensitised steels is in contradiction to this proposed model.

1.4.1c Solute Segregation Theory

Observations that solution-annealed and sensitised specimens were susceptible to intergranular attack in HNO_3-Cr_2O_7 solutions led Aust et al (68-70) to propose a more general theory of intergranular corrosion. The solute segregation theory attributes susceptibility to the presence of either a continuous region of solute, or to the formation of a second phase with concomitant solute depletion. The corrosion experiments of Aust et al indicated that intergranular corrosion was not solely related to carbide morphology, but was favoured by "continuous carbide precipitation" or by continuous solute segregation at the grain boundary. The immunity to attack exhibited by stabilised microstructures was explained in terms of redistribution of deleterious solute by preferential solution in the carbides, or by preferential segregation of the solute at the carbide/matrix interface. A high rate of intergranular attack was observed for specimens which had been slowly cooled from 1300°C to 900°C, stabilised for 1 hour, and quenched. According to the Cr-depletion theory, this treatment would have eliminated the depleted zone. Therefore, a mechanism of non-equilibrium solute segregation was proposed which is based on interactions between the solute atoms and the excess vacancy concentration. Depending upon the solute-vacancy binding energy, the solute-vacancy complexes could diffuse to the boundaries, resulting in annihilation of the vacancies and solute enrichment at the boundaries.

From the results of various investigations, four general models of grain boundaries have been presented (Figure 1.4) (70). The structures which are immune to intergranular corrosion are characterised by clean or stabilised boundaries, while solute-enriched or sensitised grain boundaries, exhibit susceptibility. The only

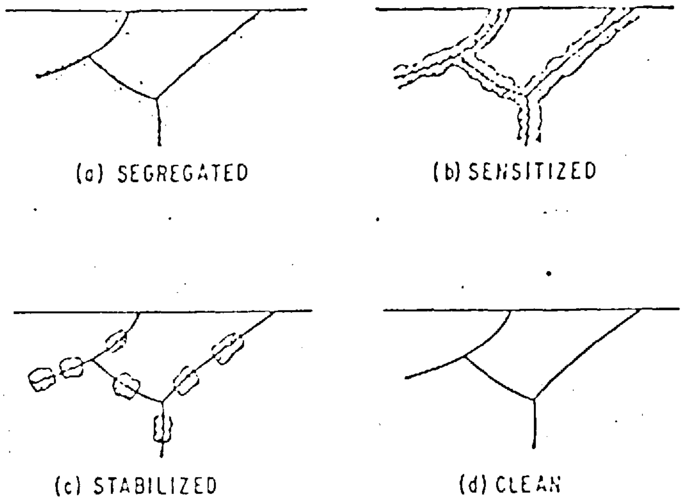

Figure 1.4 General Models of Grain Boundary Segregation Proposed by Aust et al(70).

supporting evidence of the solute segregation theory presented, other than the intergranular attack, are microhardness measurements in the grain boundary area (71). A pronounced hardening of the boundary region was observed in solution annealed specimens. No direct evidence of solute segregation was obtained due to lack of suitable microanalytical techniques.

This theory has been criticised for inadequately considering the importance of the oxidising power of the corroding environment (7,66). Austenitic stainless steels may not be passive in the HNO_3-Cr_2O_7 solution, and therefore both bulk and localised attack may occur. Solute segregation, however, would accelerate this attack.

The frequently cited theory of Bain et al (64) for explaining intergranular corrosion still appears to be valid. The excellent agreement between theoretical predictions and experimental observations of intergranular corrosion is the most convincing evidence in support of the Cr-depletion theory.

1.4.2 Strain Enhanced Corrosion

An enhanced corrosion rate on certain plastically deformed electrodes was observed by Hoar (72). It was postulated that rapidly yielding, clean metal would dissolve more quickly than static metal because of the increased concentration of "surface defects" in the former. Several investigators have proposed a strain-enhanced corrosion theory to explain the phenomenon of stress corrosion cracking.

In this theory, enhanced corrosion resulting from strain is due to repetitive surface film rupture and repair. In support of this theory, it has been demonstrated that the limiting corrosion rate is dependent upon the strain rate up to 3 x 10^{-2}/sec. Also the time required for film (monolayer) formation is approximately 10^{-3} sec. (73,74).

The effect of strain has been attributed to a local breakdown of a passive surface film, possibly by slip step emergence at the surface, or by brittle mechanical failure of the film. This would result in the exposure of fresh, clean metal to the environment, and localized electrochemical attack.

It is also possible that the effect of strain may be an energetic one (36). The energy imparted to the system as a result of the application of stress could cause a variation in the electrode potential of a metal:

$$\Delta E = \frac{{}^{2}M}{2Y\rho nF}$$

ΔE = change in electrode potential
σ = applied stress
Y = Young's Modulus
ρ = density
n = number of electrons
F = Faraday's constant

This equation predicts that the same potential shift will occur for tension and compression. Therefore, the same SCC behaviour would be expected if compressive stresses are applied to a specimen. This is not observed.

1.4.3 Film-Rupture/Slip-Dissolution

This model is, to date, the most widely accepted active path theory for SCC, particularly in the Fe-Ni-Cr alloy system. The mechanism, originally proposed by Champion (75), is based upon the rupture of a passive surface film by localised plastic deformation at the crack tip, and the rapid dissolution of the exposed metal. This preferential dissolution sharpens the crack tip, permitting further localised deformation and subsequent film-rupture. In the model of Champion, the crack tip is not assumed to completely repassivate, so that crack propagation is continuous.

The film-rupture model was developed by Vermilyea (76,77) and Staehle (49) to consider a crack tip which completely repassivates. Vermilyea attributed cracking to the rupture of the passive film itself due to strain in the film; local slip events are not considered. This modified theory considers cracking from a macroscopic approach.

Staehle (49) proposed that the protective surface film is ruptured by the emergence of slip steps, at which sites anodic dissolution occurs. Film rupture by emergent slip steps have been detected by recording the current transient under potentiostatic conditions (78,79). Important factors in this model include the slip mode of the alloy (determines the height of the slip step), repassivation rate, crack tip potential, and the strain rate (controls the rate of slip step formation) (78).

Electron microscopy of stress corroded foils has illustrated the effectiveness of active slip steps as nucleating sites for stress corrosion cracks (80). The importance of the slip step height in transgranular crack initiation was demonstrated by Silcock and Swann (33,63) who observed slip step attack at emergent edge dislocations in SCC tests of Type 316 steel single crystals. Silcock and Swann also noted the presence of two types of cracks in the initial stages of stress corrosion of Type 316 steel: those which occurred along slip traces, and cracks transverse to the slip traces which could be the result of stresses involved in corrosion sponge growth.

The slip-dissolution model has recently been applied to SCC of austenitic stainless steel (type 304) by Ford and Povich (81-83) to quantitatively explain the stress corrosion behaviour of the material in H_2O, and in dilute sulphate solutions at 97°C. In this model, the crack propagation rate is related to the bare surface dissolution rate of the metal. The agreement between the calculated and observed crack propagation rates was poor for potentials more noble than 0 mV SCE. The model was only applicable in the range 0 to -150 mV SCE (81). Numerous variables were added to rationalise the breakdown of the model. Doig and Flewitt (84,85) in their study of SCC of Fe-Ni alloys in 5M NaOH at 100°C demonstrated the importance of the electrode potential distribution within a growing SC crack. This potential drop is often ignored in many analyses of SCC, and so additional parameters must be included to adequately describe SCC via the slip dissolution model (i.e. undue emphasis is placed on micro-creep, solution chemistry and flow, oxide repassivation rate, etc.) (86).

Observations that preferential corrosion does not continue (beneath the surface) along the original slip traces have been the basis for discounting the significance of slip in SCC propagation by the slip -dissolution mechanism (61). An alteration of the local stress pattern by the formation of corrosion slots was proposed by Silcock and Swann to explain the halt of corrosion along the original slip trace (33). Slip along the original trace would no longer be favoured.

Nielsen (25), and Swann and Embury (80) have observed pits which had initiated at slip lines develop into tubular cavities (or tunnels) in stress corroded thin foil specimens. Tunnels are proposed to form because the dissolution rate along certain crystallographic directions is greater than the dissolution rate in other directions. Also, one element must dissolve more rapidly than the other elements present in the alloy for tunnel formation to occur. Tunnels appear to grow along slip traces. Stress corrosion cracks have been proposed to advance as a result of tunnel formation and mechanical tearing of the metal ligaments between the tunnels. Shallow parallel trenches on the fracture surface are believed to be the result of a tunnelling mechanism of SCC.

The slip-dissolution/film-rupture model can rationalise most fractographic observations for IGSCC (smooth, 'featureless' surfaces with some slip steps) by assuming that repassivation is slower at grain boundaries than grain interiors, a valid assumption for sensitised type 304 steel. Although this model is widely applied to examples of TGSCC, Bursle and Pugh (87) have shown that the fractography of these failures is not readily reconciled with the slip- dissolution mechanism.

Of all the active path mechanisms, slip-dissolution / film-rupture appears to be the most applicable for stress corrosion cracking. There is, however, considerable controversy in this area, and a need for additional research.

1.4.4 Corrosion Product Wedging

Pickering et al (32) proposed that the build up of solid oxide corrosion products in the stress corrosion crack produces a considerable stress which could lead to the propagation of the SC crack. Ronnquist (88) and Nielsen (25) believed that the oxide products could enhance the existing tensile stress at the crack tip. This theory is predominantly a corrosion-assisted mechanical failure mechanism. The initiation process of the SC crack is not treated.

1.4.5 Adsorption Induced Cleavage

Based on the mechanism of liquid metal embrittlement, this theory involves Cl^- adsorption in conjunction with corrosion to reduce the stress required for crack propagation (89). Surface active species adsorb on the crack tip surface and reduce the surface energy of the metal, weakening the metallic bonds. Support for this mechanism is cited from the observation by Uhlig and Cook (89) that ions which adsorb preferentially on stainless steel surfaces (i.e. iodide, nitrate and acetate ions) tend to inhibit SCC by reducing or eliminating adsorption by Cl^- or other active species. Also, the influence of electrochemical potential is explained by its effect on specific ion adsorption (90). As corrosion is not required for SCC in this theory, it is a purely mechanical failure mechanism.

The adsorption-induced cleavage model has been criticised by numerous proponents of dissolution mechanisms for failure to consider the crack-tip blunting which would occur in such ductile materials as austenitic steel (49). The fact that the observed potential range for cracking varies significantly with composition has been cited by Staehle as one of the objections to adsorption-induced cleavage (49).

1.4.6 Strain-Induced Martensite Formation

The fact that strain does promote martensite formation in metastable austenitic stainless steels led to the proposal by Edeleanu (91) that martensite formation was essential to SCC. This would assist in rationalising the path of crack propagation in transgranular SCC, as the martensite would act as the pre-existing path. Kamide and Sugawara (92) investigated the relationship between SCC and deformation structures in type 304 stainless steel using a stress relaxation method. The role of strain-induced martensite in SCC was also studied using thin-foils of pre-strained Type 304 stainless steel. After immersing the foils in 2.4 M H_2SO_4 + 0.4 M NaCl for 5 minutes, corrosion pits were observed to form along the martensite bands. Martensite corroded in preference to the austenite. It was concluded that the martensitic structures (α' and ε) contribute to the initiation and propagation of stress corrosion cracks in H_2SO_4 + NaCl solutions. Similar results were obtained by Hänninen (93) on Type 304L stainless steel. Selective dissolution of deformation structures was observed in 2.5M H_2SO_4 + 0.1M NaCl solutions. Both ε and α' martensites were preferentially attacked.

Whether the stress intensity at the crack tip is itself sufficient to induce the martensitic transformation zone ahead of the crack, or rather a combination of mechanical and environmental factors are required for the transformation is not clear. The results of Kamide and Sugawara (92), and Hänninen (93) strongly indicate that the stress itself is sufficient. A similar theory which concerns hydrogen-induced transformations also seems appropriate in that the effect of the environment is critical in SCC. This theory is treated in the Hydrogen Embrittlement section.

The strain-induced martensite theory is generally dismissed on the fact that SCC is known to occur in alloys at $T > M_{\alpha}$, and in stable austenitic stainless steels (94). The possible role of ε martensite is ignored by many investigators. It is agreed, however, that martensite may have a secondary role in SCC of austenitic stainless steels.

1.5 HYDROGEN EMBRITTLEMENT

The effect of hydrogen on the mechanical properties of metals has been the subject of numerous investigations (95-98). It is accepted that hydrogen leads to premature failure which may or may not be accompanied by a change in fracture mode. "Hydrogen Embrittlement" (HE) is the term used to describe this phenomenon. A wealth of information has been accumulated in this field, but, as of yet, no single mechanism concerning this failure process has been conclusively established.

Metals which have been embrittled by hydrogen exhibit a decreased reduction of area (RA) at failure. Other characteristics include a reduction in K_{Ic} and the possibility of a lower fracture stress. Although the term "embrittlement" connotes a brittle fracture, it has been noted that metals embrittled by hydrogen can still fail by microvoid coalescence. In other cases, a change of failure mode from ductile dimpling to intergranular or transgranular cleavage has been observed. HE may be reversible in certain conditions.

The importance of hydrogen in the process of stress corrosion cracking (SCC) has not yet been definitely settled, and is the topic of much discussion and research. There is indeed the possibility that the two phenomena are related. Therefore, it is extremely important that hydrogen embrittlement be more fully understood.

It has been stated frequently that there are two major types of HE. These are internal HE (IHE) and embrittlement due to environmental H_2. Internal hydrogen embrittlement can result from the transport of atomic hydrogen through the lattice. Intermittent cracking and delayed fracture are usually observed.

Environmental H_2 failures occur when susceptible materials are subject to stress in the presence of H_2. Cracking can occur at low K and p_{H_2}. Prior specimen exposure in H_2 is only slightly damaging, and the crack origin is usually at the surface. Van Leeuwen (99) has noted that there is little, if any, delayed failure and intermittent cracking. This, however, is the subject of some disagreement. Briant has observed brittle, intergranular fracture in static loading tests of HE susceptible stainless steels in H_2 environments (100).

Whether or not this distinction is truly valid is of little significance. It appears that the difference between these two categories of HE lies in the adsorption to adsorption reaction. In environmental HE, there are several proposed reaction steps. These are:

1) $H_2(g) \rightleftarrows H(g) + H(g)$

2) $H(g) \rightleftarrows H_{ad}$

3) $H_{ad} \rightleftarrows H_{ab}$

Of these reactions, the rate controlling reaction has been taken to be reaction (3) (101). Toya described two types of hydrogen adsorption on metals (102). Figure 1.5 illustrates the various states of hydrogen and relative energies (103). The two classes of adsorption are r-type and s-type. The r-type "ad-atoms" have a lower energy than

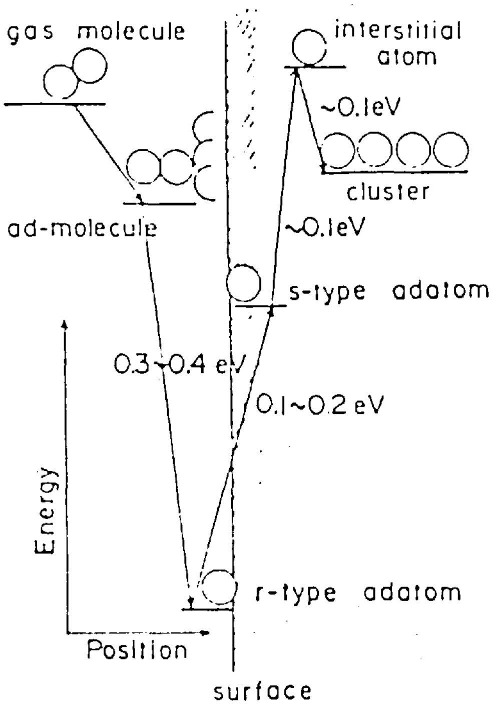

Figure 1.5 Various States of Hydrogen and Relative Energies.(from Fujita, ref.103)

energy than both gaseous H and s-type "ad-atoms". No lattice strain is associated with the r-"ad-atoms", while the hydrogen-expansion of the metal lattice involved with the formation of s-"ad-atoms" results in a higher energy state. As the s-"ad-atom" diffuses into the lattice, it increases its energy (due to the strain energy) and now becomes an interstitial atom. The lattice expanding strain could drive excess H-atoms to aggregate in a platelet form within the metal. In the case of austenitic stainless steels, there is an expansion of the fcc lattice as a result of the occupation of the tetrahedral interstices by absorbed H.

Cathodic charging of H in IHE eliminates the first reaction, so the remaining reactions are H-adsorption and H-absorption. Similarly, the absorption step is rate-controlling.

1.5.1 Theories of Hydrogen Embrittlement

Of the numerous suggestions and theories regarding the role of hydrogen in material behaviour, four major theories have been proposed and developed which merit serious consideration. These are the lattice decohesion theory, the hydrogen adsorption theory, the theory of hydrogen-induced transformations, and the void pressurisation theory.

1.5.1a Lattice Decohesion Theory

The lattice decohesion theory (LDT), originally proposed by Troiano, is the most widely cited for explaining brittle failures involving hydrogen in steels (104). It postulates that absorbed H caused a reduction in the cohesive force of the metal lattice. In this theory, for H-induced crack propagation, the crack advances when a maximum elastic tensile stress in the non-Hookean region of the crack tip equals the maximum cohesive resistance force between atoms. Stress redistribution due to plasticity in cracked and notched specimens leads to a region at the crack or notch tip where the stresses are maximum. These elastic stresses can be a significant fraction of the yield stress. This region has been termed the "decohesion enclave" by Boyd (105). There will be a flux of hydrogen into the decohesion enclave, due to the reduced chemical potential of hydrogen. In van Leeuwen's analysis of hydrogen-induced cracking, it was shown that Fick's Laws can be used to calculate the stress-induced hydrogen concentration in the decohesion enclave. If the hydrostatic stress can be determined from the stress distribution, Fick's second law can be solved to yield a time-dependent H concentration profile. At equilibrium, the stress-induced H concentration can be given by the following equation.

$$C_s = C_B \exp \frac{V^*\sigma}{RT}$$

where C_s = stress-induced H content
V^* = partial molar volume of H

This large stress-induced concentration lowers the maximum resistive cohesive force F_c so that the stress attained in the decohesion enclave can equal the maximum lattice cohesive force. Crack propagation will commence if a critical combination of local stresses and hydrogen content is attained. This has been demonstrated by Troiano (104), Gilpin et al.(106), and Oriani and Josephic (107). Oriani and Josephic examined the effect of stress intensity and hydrogen fugacity on crack propagation. From decohesion theory, it may be inferred that a small variation in either K or p_{H_2} should result in a change in the rate of crack propagation. Experimental confirmation was obtained in that small decreases in K were found to halt crack propagation, and increasing p_{H_2} caused reinitiation of cracking. The results of their acoustic emission tests were interpretted as support of the decohesion theory since they believed that decohesion should be an atom-by-atom process, and therefore "silent". The interpretation of these results is dubious, as similar acoustic emission data would be expected by an adsorption mechanism of hydrogen embrittlement.

The question as to the effect of alloying elements or impurities on the maximum lattice cohesive force merits further consideration. Work by McMahon and Rellick (108), and Bernstein et al.(109) has been interpreted as confirming the deleterious effects of segregated elements on F_c. Insufficient data are available, however, for conclusive evaluation.

The importance of hydrostatic tensile stress has been demonstrated by St.John and Gerberich (110) through testing circumferentially notched round bars in tension and torsion. There was no evidence of hydrogen embrittlement for specimens tested in torsion. Gerberich and Hartbower

(111) have correlated the crack increment with the minimum width (l) of the plastic zone ahead of the crack for intermittent cracking.

In the simplified approach to the lattice decohesion theory, stress fields are predicted on an atomic scale from the plasticity solution for a sharp crack tip, and the material under consideration would fail in a brittle manner if the critical cleavage stress is reached before the critical shear stress. Therefore, a sufficient lowering of σ_c for the interface by adsorbed or absorbed H would allow an atomistically sharp crack to advance on inter faces for which it would not normally be stable against blunting. Oriani had presumed in his analysis that the reduction in cohesive strength was a linear function of the local hydrogen concentration.

Van Leeuwen (112), and Rice and Thomson (113), have analysed the mechanical and thermodynamic aspects of hydrogen embrittlement in detail. Van Leeuwen (112) used the more complicated Li-Oriani-Darken expression for the stress dependent chemical potential, and then calculated the crack tip radius without neglecting blunting due to plasticity. The Creager-Paris equations were employed in the calculation of the stress-redistribution. He also assumed that the reduction in cohesive strength was a power function of the hydrogen concentration. In his analysis of IHE, the location of the decohesion enclave was found to be approximately at the elastic/plastic interface as determined through fracture mechanics. The axial stresses in this enclave will equal the constrained yield stress. The incubation time for stresses at and above the threshold can be described analytically. Van Leeuwen's model was successfully applied to previous experimental data and observations. For environmental H_2 embrittlement, he concluded that kinetics of cracking may be affected by adsorption. In both cases, however, it appears that lattice decohesion is the basic cause of hydrogen embrittlement.

The Rice and Thomson analysis (113) considers basic energetic aspects of sharp crack-tip stability and the activation energy for dislocation nucleation at the crack tip. The nucleation energy is linearly related to the dislocation loop self energy, the energy of the ledge produced, and the energy decrement due to the introduction of dislocations into the crack tip stress field. The most important parameters in the interfacial separation processes are the separation (surface) energy γ and the cohesive strength. For cleavage, the magnitude of the stresses on the interface must be locally equal to the cohesive strength, and the stress concentrating source ($\perp$s or $\sigma_{app.}$) must be able to supply the required separation energy to a unit area of interface for crack propagation to occur. Clarification of the effect of H on the cohesive strength and separation energy was attempted by Rice and Thomson in a thermodynamic analysis. Since the fracture parameters σ_c and γ_c depend on the variation of the chemical potential and interfacial excess concentration with separation, the two limiting cases (as proposed by Oriani) were treated. These cases involved separation at constant interfacial excess concentration, of "fast" separation which would prohibit transport to the interface, and separation at constant chemical potential (slow separation). Using the Gibbs Adsorption Isotherm and the Maxwell reciprocal relations, Rice and Thomson found agreement with the predictions of the lattice decohesion theory (LDT).

1.5.1b Hydrogen Adsorption Theory

The aspect of adsorption of hydrogen is largely neglected in LDT since, in that theory, the important species is absorbed H. The H- Adsorption Theory of Petch and Stables (114,115) attempts to link cracking susceptibility with a reduction in surface energy which, in turn, is related to surface chemisorption through the Gibbs Adsorption Equation. Although the LDT and HAT attribute failure to the effect of atomic hydrogen, there is a distinction in the mode of interaction of this atomic hydrogen. The form of the relationship between the reduction in fracture toughness and hydrogen pressure is dependent upon the dominant reaction, i.e. surface or interstitial.

In order to clarify the importance of adsorbed H, Petch first assumed that the Griffith crack stability relationship was valid. This was sharply criticised by those who cited the work of Orowan which claimed that the dominant factor in controlling crack growth was the work of plastic deformation (γ_p) which was assumed not to be a function of crack length. Their modified equation was of the form:

$$(I - \nu^2)\ \pi\sigma^2\ c^* = 2(\gamma_s + \gamma_p)E$$

where c^* = crack length, ν = poisson's ratio, E = Young's modulus.

Since γ_p was much greater than γ_s, and if hydrogen did decrease γ_s, they claimed it would not necessarily follow that $\pi\sigma^2 c*$ would decrease. Rice (116) later clarified the role of γ_p by demonstrating that γ_p was a function of c* and that it was dominated by product of the local flow stress and the crack opening displacement. Therefore, the Irwin-Orowan assumption was false for describing crack equilibrium in the presence of limited plasticity. The corrected expression, valid in the presence of an adsorbing species, is:

$$K_{I_{scg}} = K_{I_c} \left(\gamma_s{}^a/\gamma_s\right)^{\frac{1}{2}}$$

where $K_{I_{scg}}$ = plane strain stress intensity due to an agressive environment

$\gamma_s{}^a$ = γ_s measured after equilibrium adsorption.

Heady (115) analysed another major objection to the HAT, questioning the validity of the proposed inherent relationship between surface energy and fracture toughness. The HAT was criticised for the existence of the $K_{I_{scg}}$ equation which constitutes a necessary and sufficient criterion for cracking. It had been argued that: 1) Petch's analysis had merely produced a necessary condition for cracking; and 2) that there must be free, continuous access of adsorbate to the crack tip. Heady showed that the $K_{I_{scg}}$ equation did fulfill the requirements for a necessary and sufficient cracking condition. For cracking in hydrogen-bearing environments, the problem of adsorbate access is eliminated. A unit of crack extension can occur only with the immediate expenditure of γ_s/unit area (ignoring γ_p). Only hydrogen satisfies the γ_s and the size requirements necessary for embrittlement.

There was much criticism of Petch's initial analysis of HAT. This concerned the details of the analysis, particularly Petch's selection of values for various parameters such as γ_s and the adsorption function, and his use of p_{H_2} for hydrogen fugacity. These factors have been corrected in the light of recent data (unavailable to Petch). The corrected results are similar to Petch's calculations of anticipated embrittlement.

Heady (115, 117) attempted to resolve the role of adsorbed H in crack propagation by eliminating the hydrogen-induced damage which would occur in a critical region ahead of the crack tip as described by Johnson, Mortlet and Troiano (118). This was accomplished by using a crack growth rate of 0.27 cm/sec. Results of the critical stress intensity measurements in H_2 indicated that there was a decrease in fracture toughness due to environmental change. The reductions in K were approximately 2.7%, which was much lower than the theoretically predicted value of 10%, but it is most likely that H-damage had not been completely eliminated. The mode of failure was unchanged in hydrogen. This tends to support the Petch-Stables HAT although there is an order of magnitude difference between theoretical prediction and experimental observation.

For the H-absorption damage observed by Mortlet, Johnson and Troiano, changes in embrittlement are supposedly proportional to changes in the lattice concentration of H, and, from Seivert's Law:

$$\frac{d \ln K_{I_{scg}}}{d \ln P} \cong - 0.5$$

However, if the H-adsorption damage described by Petch and Stables is controlling, the relation is:

$$\frac{d \ln K_{I_{scg}}}{d \ln P} \cong - \Gamma_{sat} \frac{kT}{4\gamma(P)}$$

where $\gamma(P)$ = surface energy in equilibrium with hydrogen at pressure P. The low embrittlement behaviour of $K_{I_{scg}}$ where the fracture morphology is constant can unequivocally distinguish between crack stability controlled by H-adsorption on the crack tip surface, and H-adsorption. The experimental difficulties are extremely great in the determination of the role of adsorbed hydrogen in the process of hydrogen embrittlement.

Recently, the data of Oriani and Josephic (107) has been re-evaluated with respect to the adsorption theory (119). By applying the Temkin adsorption isotherm to their data, Sieradzki and Ficalora (119) have shown that the adsorption theory adequately explains the dependence of K_{th} on p_{H_2}. Ransom and Ficalora (120), investigating the adsorption of hydrogen on iron, demonstrated by magnetic measurements the existence of chemisorbed H_2^+ ions at ∿ 77°K, and H^- at temperatures above 300°K. The observed dependence of the crack growth rate (in hydrogen) with temperature can be explained by the H_2^+ and H^- species. An increase in pressure (at constant temperature) will increase the H^- concentration and enhance cracking. Ransom and Ficalora proposed that as the pressure of hydrogen gas increases, the point at which desorption becomes rate determining shifts towards higher temperatures.

Hydrogen adsorption, however, does not appear to be solely responsible for all failures attributed to hydrogen embrittlement.

1.5.1c Hydrogen-Induced Transformations

It was previously stated that there is a strain energy associated with the presence of atomic hydrogen in the austenite lattice resulting from the occupation of the tetrahedral intersticies by hydrogen. This strain may be able to induce a martensitic transformation in the austenite. Research has been conducted to clarify the role of hydrogen-induced transformations (HIT) in the hydrogen embrittlement of steel. The theory of HIT enjoys limited acceptance because it is only applicable to the austenitic alloys which could accommodate a martensitic micro-constituent. In this theory, a combination of low H diffusivity, high H fugacity, and austenite stability result in a spontaneous transformation to either ε or α' martensite due to the severe internal strains which had developed. The material subsequently undergoes intergranular or transgranular fractures.

It is necessary to determine the role of H in martensitic transformations and the importance of austenite stability. Eliezer et al (121) attempted to do this by examining metastable (type 304) and stable (type 310) austenitic stainless steels during cathodic charging and exposure to H_2. Specimens were mechanically tested in tension above and below the M_D temperature, and the amount of α' produced on the fracture surface was measured using a commercial ferrite detector. The ductile shear fracture observed in type 304 specimens tested in air contained 2 ± .6% α' while a 4.5 ± .5% α' content was detected for the same material after failure in H_2. The latter fracture surfaces were transgranular and cleavage-like, and the α' was confined to a region approximately 3mm on either side of the crack. Similar behaviour was observed for cathodically charged specimens of type 304 steel. In all tests, no α' could be detected for type 310 specimens. Testing above the M_D resulted in ductile failure. These results strongly indicate the importance of α' for hydrogen-induced slow crack growth of type 304 stainless steel.

There are several possible roles of martensite in crack growth. Since the lattice diffusivity of H is $10^{-5} cm^2/sec$ in a bcc structure as compared with $10^{-12} cm^2/sec$ in a fcc structure, the α' formed ahead of the crack tip could provide a rapid diffusion path for H. This idea is supported by measurements of H-induced crack velocities (∿ 2.5μm/sec) which would require a hydrogen diffusivity of $5 \times 10^{-8} cm^2/sec$ for H transport to the γ. Birley and Tromans (122) postulated that hydrogen embrittlement of unstable austenitic stainless steels could be autocatalytic - the martensitic structure aiding hydrogen entry, followed by the cracking of the embrittled material which would lead to a stress-induced concentration of H at the crack tip and the formation of strain-induced α'.

As α' martensite is highly susceptible to hydrogen embrittlement, it could be possible for the crack to propagate through the α' plates or along the α'/γ interface. This hypothesis is rather unlikely for explaining the embrittlement behaviour of all austenitic stainless steels because no martensite could be detected on the brittle fracture surface of the type 310 specimens.

The hcp martensite, ε, has been observed in several investigations of austenitic steels. It is the intermediate structure in the $\gamma \rightarrow \alpha'$ transformation: (fcc) γ(fcc) $\rightarrow$ ε(hcp) $\rightarrow$ α'(bct). McCoy (123) claimed that ε is resistant to HE from his experiments with high Mn steels. The presence of ε did not change the fracture mode when tested in H_2; failures were ductile. Thompson (124), however, could not confirm McCoy's hypothesis. This discrepancy could have been caused by the formation of α' in the Fe-Mn alloys and, also, the variations in testing conditions.

A fractographic investigation of the effect of pre-existing α' martensite in the hydrogen embrittlement of type 304 stainless steel was conducted by Hänninen and Hakkarainen (125). The presence of α' martensite prior to charging significantly increases susceptibility to H embrittlement.

By cathodically charging thin foils of type 304 stainless steel, Holzworth and Louthan (126) demonstrated that hydrogen promotes the $\gamma \rightarrow \varepsilon + \alpha'$ transformation. The transformation products were found to be the same as those obtained after low temperature (-196°C) deformation.

Hänninen et al.(127) examined three austenitic stainless steels (304, 310 and 316) after hydrogen charging, and observed transformation products similar to those reported by Holzworth and Louthan (126). Both α' and ε martensites were detected in type 304 stainless steel, while only ε martensite was present in the stable austenitic stainless steels. Hydrogen-induced cracks were found to follow γ/α' or γ/ε phase boundaries. No evidence of hydride formation was observed in these investigations, although it had been reported in previous studies (128-130).

The Hydrogen-Induced Transformation theory requires further experimentation so that its importance in the hydrogen embrittlement of austenitic steels may be evaluated. At the present, the effects of hydrogen on the behaviour of the parent austenite or the martensite microconstituent can not be distinguished. Although this theory has been widely dismissed on the basis of limited applicability, the existence of hydrogen-induced ε and α' in susceptible materials cannot be denied. Clearly, more information is required for experimental verification of H in hydrogen embrittlement.

1.5.1d Void Pressurisation Theory

The preceeding theories concerning hydrogen embrittlement have only been concerned with the effect of atomic hydrogen on material behaviour. No theory has dealt with the possibility of gaseous H_2 in the metal and its subsequent effect on the properties of the metal. The Void Pressurisation Theory (VPT) attempts to explain the role of

H_2 in hydrogen embrittlement of materials whose failures are ductile. Hydrogen has been reported to cause a decrease in ductility parameters (specifically 'reduction of area' (RA)) without changing the mode of failure. The role of hydrogen in ductile fracture is nonetheless significant in the study of hydrogen embrittlement.

Important processes in ductile failure are the nucleation and growth of voids, and shear band localization. Sheets of small voids can nucleate in the shear bands, in addition to the nucleation of larger voids at inclusions and other second phase particles. Since void formation is initiated by the decohesion of the particle from the matrix, it is plausible that atomic hydrogen could cause a reduction in the interfacial strength and promote decohesion, as stated in LDT. Another possible effect of hydrogen could be the stabilisation of atomic spearations at the interfaces which occur prior to the opening of the interface. Hydrogen has been reported to produce an increase in the volume fraction of particles observed on a ductile fracture surface (131). This could be taken as support of a hydrogen effect on void nucleation.

The growth of voids preceeding fracture could be enhanced by the presence of H_2 in the growing void. The recombination of atomic hydrogen in a void would result in an increasing pressure of H_2 exerted in the void, assisting its growth. An essential process in P_{H2} - assisted void growth is the transport of atomic hydrogen to the particles and voids. In this theory, a dislocation-transport mechanism is assumed in order to explain the rapid build-up of hydrogen at sinks (particles, grain boundaries). (This mechanism will be fully discussed in the next section). If the arrival rate of hydrogen at the sink is greater than the rate of lattice diffusion away from the sink, it will be possible to attain a large non-equilibrium hydrogen concentration (high P_{H_2}). The rate of hydrogen pressurisation ($\dot{P}$) of voids is dependent upon strain rate and temperature. $\dot{P}$ is inversely proportional to the particle size and the volume fraction of particles. If the hydrogen pressure assistance of void growth accelerates void coalescence, there should be a reduction in RA (131).

In the absence of external stresses, the H content in excess of the equilibrium solubility limit for large amounts of dissolved H (>1 ppm) can be written as (132):

$$C_{ppm} = 42.7\, P_{H_2}^{\frac{1}{2}} \exp\left(\frac{-6500}{RT}\right)$$

This will precipitate as H_2 and, in so doing, sets up a concentration gradient so that more H diffusion and H_2 pressure accumulation occurs until the interface and lattice concentrations are equal. The pressure effect is dominant above 1 ppm concentration of dissolved H.

The clustering of hydrogen has been treated recently by Fujita (133). It is postulated that the lattice expanding strain around each interstitial H atom could drive excess H atoms to aggregate in platelet form in the lattice. The platelet-type aggregates or clusters have a lower free energy than do interstitials. Mossbauer spectroscopy has shown that inhomogeneous distributions of hydrogen do exist, in H-charged Fe-base alloys. Kamachi (133, 134) has also observed aggregation of excess H in steel in the form of platelets.

In order to distinguish whether the void nucleation or growth process is affected by hydrogen, Thompson (131) proposed that the dimple size on the ductile failure surface should correspond to the particle spacing obtained from the effective volume fraction of particles, rather than increase in size. However, hydrogen accelerated hole growth would affect the number of particles which act as nucleating sites, because failure would occur before voids could be nucleated at the most strongly bonded or smallest particles. Therefore, the fracture surface would be composed of larger dimples. Measurements of dimple diameters in H-charged and uncharged carbon steel specimens support this claim. Thompson cites this as evidence that the nucleation behaviour of particles which do act as void origins is unaffected by hydrogen. Additional support is obtained from measurements which show no effect of hydrogen on the interfacial strength of that particular steel. Fujita's model (133) of hydrogen clustering, however, postulates that when a hydrogen cluster is formed in the Fe-lattice, the conduction electrons are repelled from the cluster due to lattice expansion and therefore the iron lattice bonding will be considerably diminished. Direct evidence of the effect of hydrogen on the electronic state of Fe has been produced through measurements of internal magnetic fields. It has been proposed that hydrogen affects the 3-d state of the Fe atoms and the bonding nature of the Fe atoms.

The mechanism of void pressurisation by H_2 cannot be definitely distinguished from effects of lattice decohesion with experimental observations obtained to date. This is another area for further investigation. At present, the material parameter which appears to determine whether void nucleation and growth, or only void growth will be affected by hydrogen is the nature of the second phase particles. If a wide variety of particle sizes exists, then hydrogen can affect the nucleation behaviour, whereas materials containing a dispersion of relatively uniform particles will experience pressurisation accelerated void growth.

Recent reviews (135,136) concerning the effect of hydrogen on the behaviour of materials have indicated that the embrittlement process may, in fact, involve all of the previously described mechanisms. This proposition is reasonable considering the similarities of these mechanisms.

1.5.2 Hydrogen Transport: Dislocation Sweeping Mechanism

Essential to most hydrogen embrittlement theories is the transport of atomic hydrogen through the metal. Diffusion of hydrogen is a possible mechanism, but embrittlement data indicate that this process alone is incapable of suitably explaining the rates of hydrogen transport required. In austenitic steels particularly, the diffusivity of hydrogen at room temperature is approximately $6 \times 10^{-10} cm^2/sec$. There is also evidence that grain boundaries are not short circuit paths for significant diffusion at ambient temperature for Fe and Fe-base alloys (137). Permeation and mechanical relaxation techniques have been utilized to obtain data for the diffusivity of H, but since H is readily trapped at external surfaces and internal sinks, these measurements are not completely valid (137).

To explain the rapid transport of hydrogen through a metal, a Dislocation Sweeping Mechanism (DSM) has been proposed (137). When present in the material, hydrogen can interact with dislocations resulting in the formation of Cottrell atmospheres. Then as the dislocations move, the hydrogen can be redistributed to certain microstructural locations (sinks) which can be the critical path for H-induced fracture.

A comparison of the diffusion penetration depth from the Random Walk Analysis, and the maximum penetration distance due to dislocation sweeping suggests the validity of the DSM for hydrogen transport. In the DSM, the distance of maximum penetration X_c is related to a critical velocity $\bar{V}_c$ of the H-bearing dislocation and the duration of dislocation movement:

$$\bar{X}_c = \bar{V}_c t$$

There is a limited range of V_c values which are applicable to the H-dislocation transport model. When the velocity of the dislocation exceeds the critical value $\bar{V}_c$, the dislocation will break away from the Cottrell atmosphere, depositing the hydrogen in the matrix. For dislocation velocities less than or equal to $\bar{V}_c$, the hydrogen will be effectively swept through the matrix. Hydrogen appears to reduce the lattice friction stress so that a dislocation with a hydrogen atmosphere can be more mobile in the lattice than would a clean dislocation, or one with a C or N atmosphere.

In addition to the velocity considerations, the DSM will only operate when the force between the hydrogen and dislocation is greater than the force driving the dislocation (difference between the applied force and forces due to internal stresses). Another significant variable is the strain rate $\dot{\varepsilon}$ (138). The dislocation mobility is determined by the strain rate. There exists a critical $\dot{\varepsilon}$ above which no hydrogen will be transported. Assuming that the total dislocation density is approximately equal to the density of mobile dislocations, calculations have shown that dislocation transport will be operable over the range of $\dot{\varepsilon}$ commonly used in the laboratory. For fcc materials (Ni- base alloys and austenitic stainless steels) with a dislocation density of $10^{10}/\mathrm{cm}^2$, the critical strain rate above which dislocation transport will not operate is 10^{-1}/sec. Experimentally, it has been shown that ductility losses due to HE in type 310 diminish with strain rates greater than 10^{-1}/sec (137).

Additional support of DSM has been found in tests involving tritiated specimens of type 304 stainless steel (137). The initially rapid tritium release rate occurring during tensile tests was directly related to the onset of plastic deformation. As deformation progressed (and the dislocation density increased), the release rate decreased until a sharp increase was observed at fracture. This behaviour has been explained via the DSM in that, initially, dislocations would carry a saturated load of tritium until the dislocation density reaches $10^9/\mathrm{cm}^2$ (initial stages of plastic deformation). As the deformation progresses and the dislocation density increases, the H content of the dislocations would decrease on the average. During work hardening, the decrease in the tritium release rate could be due to the reduction in the mean free path of dislocation travel, and the subsequent decrease in dislocation transport capacity. The sudden increase in the release rate observed at necking and fracture is attributed to the rupture of voids which were pressurised with tritium as a result of dislocation transport (139).

For hydrogen embrittlement to occur in the metal, particularly in plastic zones, the mobile dislocation must lose its hydrogen (137, 140). This can be accomplished by one of three possible mechanisms. The first possibility is that the dislocation exceeds its critical velocity $\bar{V}_c$ and, in so doing, dumps the hydrogen. This mechanism is dependent upon dislocation dynamics. If the period during which the $\bar{V}_c$ value is exceeded is brief, as experienced in dislocation break-away from pinning points, H can be deposited locally in the matrix, and may then be picked up by another mobile dislocation, or the H may diffuse to a sink.

The second mechanism deals with dislocation annihilation. Annihilation of H-bearing dislocations results in H-enriched areas. This hydrogen would be available for sweeping by other dislocations, or could diffuse through the material.

Through the third possible mechanism, decrease in ductility attributed to hydrogen embrittlement, as described in the VPT, can be rationalised. In this mechanism the hydrogen-carrying dislocation encounters an inclusion or second phase particle and strips H from the dislocation. The amount of H removed corresponds to the H content on the dislocation line which intersects the particle. This hydrogen can then seep into voids, recombine, and balance the local fugacity inside the void. Void pressurisation can occur if the arrival rate of hydrogen to the void is greater than the hydrogen diffusivity.

1.5.3 Hydrogen Embrittlement and SCC

The primary reason presented for excluding Hydrogen Embrittlement as a mechanism of SCC was that under anodic polarisation, the direct deposition of hydrogen was believed to be impossible. The behaviour of susceptible materials under anodic and cathodic potentials is the major observation in support of dissolution mechanisms. As was previously discussed (Section 1.3.6), the work of Barth and Troiano (56) explained the effect of cathodic protection in terms of O, and demonstrated that SCC failures were related to the presence of hydrogen. Electrochemical conditions are still important in an HE mechanism of SCC in determining the rate of hydrogen evolution on the alloy surface. The highly acidic conditions observed at the crack tip favour proton reduction. It is very likely that this hydrogen could be absorbed and produce a readily corrodible or mechanically weak path which would result in crack propagation.

Some investigators have proposed hydrogen embrittlement as a mechanism of SCC, in which crack propagation and brittle fracture would occur as described by either the decohesion, adsorption or H-induced transformation theories (Sections 1.5.1a-c) (141-145). Evidence in support of a hydrogen and strain-induced transformation in type 304 austenitic stainless steel has been presented by Vaughan et al. (141), Birley and Troiano (122), and Keys et al. (142). Previous investigations into the SCC of austenitic stainless steel had led to the erroneous conclusion that SCC was accompanied by hydride formation in the crack tip region (141). This "hydride" is actually ε- martensite. It is still believed by some investigators that a hydride phase does exist in the austenite (146,147), but evidence for the existence of a hydride is far from conclusive. An extensive study of hydrogenated surface layers in 304L, 310, and 316L using x-ray diffraction and Mossbauer spectroscopy was recently conducted by Mathias et al (148). They concluded that hydride formation does not occur in austenitic stainless steels. Rhodes (35) proposed that the hydrogen evolved at the SCC tip may be absorbed into the γ lattice causing an expansion of the lattice which would promote martensite formation. Crack propagation could then occur at the interface between parallel sheets of laths. Micro autoradiographic studies of hydrogen trapping in Fe-Cr alloys (7 ∿ 9.4 wt% Cr) have revealed that hydrogen segregates to the α'/ferrite interfaces (149), so it may be expected that H segregation would occur at grain boundaries and at α' or ε/γ interfaces. The hydrogen cracking observed by Hänninen et al. (127)

indicates that this does occur. Vaughan et al.(141) has observed that H - charged foils of 304L are attacked more readily than uncharged specimens in 154°C $MgCl_2$. Since the fracture behaviour of α' martensite is unable to account for all of the SCC morphologies observed, it is likely that other processes may be involved in SCC.

The major criticism of this mechanism is its limited applicability to metastable austenitic stainless steels (94, 141, 150). The observation of Wilde and Kim (57) that no absorbed hydrogen was detected in specimens exposed to boiling Cl^- solutions is frequently cited when dismissing any hydrogen embrittlement mechanism of SCC. Their evidence (57), however, is not sufficient for such a statement regarding SCC mechanisms.

Hydrogen embrittlement and SCC are both manifestations of environmental fracture. The similar effects of alloying and thermomechanical processing on the susceptibility of steel to HE and SCC have been sited by some investigators as an indication that, indeed, the two phenomena are related (94, 143). An increasingly prevalent opinion is that SCC involves two basic mechanisms - anodic dissolution and hydrogen embrittlement. Anodic dissolution (slip-dissolution) is generally accepted as the dominant mechanism for crack initiation. Crack propagation is proposed to occur as the result of hydrogen embrittlement, with crack-tip sharpening occurring by anodic dissolution (94). The balance between these competing mechanisms is a delicate one. Variations in microstructure, composition, environment, etc. may favour one mechanism over the other. If this is correct, it is not difficult to understand the confusion which has arisen in the past due to attempts to define a single mechanism for SCC.

1.6 SUMMARY

The importance of alloying, environment, stress and electrochemistry in this complex failure phenomenon has been demonstrated. Numerous investigations have resulted in several proposed mechanisms to explain SCC. Of the 'active-path' mechanisms, slip-dissolution has received the most support, but this does not eliminate other potential mechanisms. The similarities between SCC and HE suggest that these two processes are indeed related. From the available data, the proposed existence of two competing mechanisms in SCC appears to have some sound basis. Which mechanism dominates in a particular system would be dependent on the nature of the alloy, electrochemical, environmental and mechanical effects. Still, there is much to be done in defining the role of hydrogen in SCC before a conclusive theory of SCC can be established.

CHAPTER 2

MATERIALS AND EXPERIMENTAL TECHNIQUES

2.1 MATERIAL

Type 304 stainless steel was supplied in the form of mill-annealed sheet (1.0 mm in thickness). The composition of the material is presented in Table I. The steel was cold-rolled on a bullion mill to a final thickness of approximately 0.5mm.

TABLE I

Composition of Type 304 Stainless Steel (wt.%)

C	Cr	Ni	Mn	Mo	Si	S	P	Cu
0.7	19.0	9.0	1.55	0.25	0.54	0.03	0.025	0.2

2.2 SAMPLE PREPARATION AND HEAT TREATMENT

Miniature sheet tensile specimens and 3.0mm. diameter discs were punched from the cold rolled sheet. Figure 2.1 contains a diagram of the tensile specimen with relevant dimensions.

All specimens were encapsulated in quartz, and evacuated to $\sim$ 50 millitorr pressure prior to each heat treatment. The cold rolled material was then solution annealed for ½ hour at 1110°C and water quenched. The sensitisation treatments examined were conducted at 675°C and 600°C. A detailed schedule of heat-treatments is presented in Table II.

After sensitisation, the miniature tensile specimens were abraded with 600 grit SiC paper to remove the oxide film. Specimens were not pickled as residual fluoride ions from pickling have been demonstrated to affect the SCC behaviour of the material (40). After lacquering the ends of the specimens, the gauge length regions were electro-polished in 95% Acetic Acid - 5% Perchloric Acid solution at 30V at 20°C. The gauge length of each polished specimen was carefully scribed prior to testing.

Figure 2.1

Diagram of Miniature Tensile Sepcimen

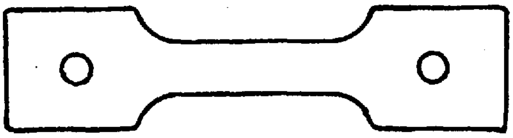

Specimen Dimensions

Gauge Length	*20.0 mm*
Thickness	*0.5 mm*
Width	*6.0 mm*

TABLE II

Sensitisation Schedule

Temperature / Time	15min.	30min.	2hrs.	24hrs.	72hrs.	100hrs.
600°C			X	X	X	
675°C	X	X	X	X	X	X

2.3 MECHANICAL TESTING

2.3.1 Solution-Annealed and Sensitised Material

The mechanical properties of the solution-treated and sensitised steels were evaluated through conventional tension tests conducted on an Instron machine. A crosshead speed of 0.05 cm/min was selected, which resulted in a strain rate of 2.6×10^{-4} $\sec^{-1}$.

2.3.2 INTERGRANULAR STRESS CORROSION CRACKING

The stress corrosion cracking susceptibility of the sensitised material in dilute H_2SO_4 + NaCl solutions was evaluated through static load and slow strain rate tests. The effect of pH (concentration of H_2SO_4 + NaCl solution) on the SCC behaviour was also examined. The slow strain rate experiments were comprised of two series of tests: 1) those conducted at the free corrosion potential (no potentiostatic control), and 2) controlled potential tests.

Preliminary SCC tests were conducted on simple U-bend specimens of sensitised 304 in boiling $MgCl_2$ (150°C) and LiCl (120°C) solutions. Neither solution promoted intergranular failure. Additional tests were conducted in 5N H_2SO_4 + 0.5N NaCl solution at room temperature, an environment reported to promote integranular SCC (151). Examination of the fracture surfaces revealed that excessive dissolution had occurred.

It was decided to continue with room temperature SCC tests in dilute H_2SO_4 + NaCl solutions. Environments employed in this investigation were 0.12 M H_2SO_4 + 0.02 M NaCl (pH =1) to 1.2×10^{-4} M H_2SO_4 + 2×10^{-5} M NaCl (pH =4). Dilute H_2SO_4 + NaCl solutions promoted intergranular SCC, but caused minimal general attack. These acidic environments are also more applicable to real SCC failure conditions, in contrast with the artificial $MgCl_2$ and LiCl solutions.

All test solutions were prepared with Analar grade reagents and distilled H_2O.

2.3.2a) Static Load SCC Tests

Creep rigs were slightly modified to facilitate environmental testing. All specimen grips and screws were machined from Type 304 stainless steel to eliminate any reaction between the specimen and the grips. Figure 2.2 illustrates the experimental arrangement. The stress corrosion environment was contained with Quickfit cone adapters as shown in Figure 2.2.

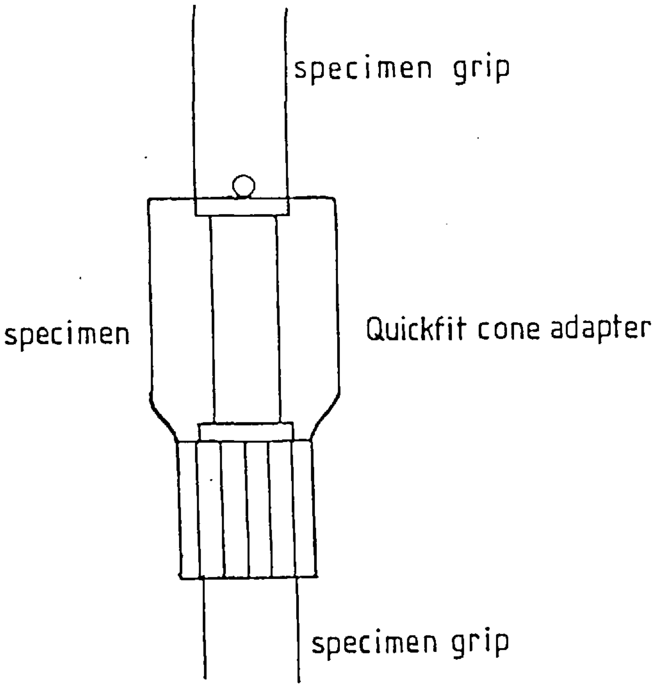

Figure 2.2 Sustained Load SCC Test Apparatus

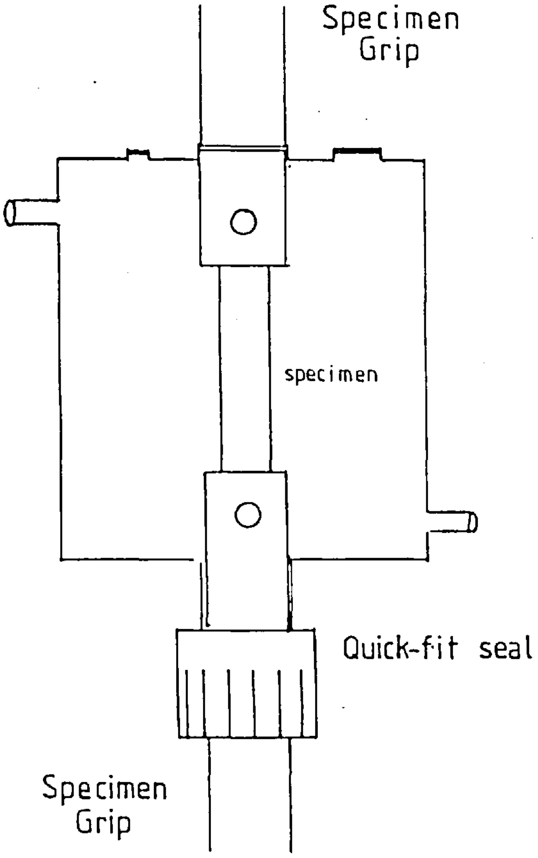

Figure 2.3 Slow Strain Rate SCC Test Apparatus

Loads used in this series of tests were 45 kg, 100 kg, and 145 kg.

As the data obtainable in these tests are limited, most of the SCC testing involved the slow strain rate technique (152).

2.3.2b) Slow Strain Rate SCC Tests

Slow strain rate SCC tests are most advantageous in that all tests end in specimen failure. By examining the mechanical behaviour of the material in the SCC environment and comparing this with the response of the material in an inert environment, a measure of the SCC susceptibility may be obtained. The extent of SCC in the failure can be readily determined by studying the fracture surfaces; stress corrosion fracture will be brittle (trans or intergranular) while failure due to exceeding the UTS will occur by microvoid coalescence.

All slow strain rate tests were conducted on an Instron machine. A crosshead speed of 0.0005 cm/min was selected; the strain rate was approximately 2 x 10^{-6} $\sec^{-1}$. Environmental testing was accomplished by using a specially designed pyrex cell, which is illustrated in Figure 2.3. The glass-metal connection is a standard Quickfit screw-on seal. The cell was designed so that tests could be potentiostatically controlled, if required.

2.3.2c Controlled Potential Slow Strain Rate Tests.

The final series of SCC experiments involved controlled potential slow strain rate tests. Of prime importance in a purely dissolution mechanism for SCC is the fact that the application of a cathodic potential inhibits cracking. Controlled potential tests were conducted in pH=1 and pH=2 H_2SO_4+ NaCl solutions. A Wenking Potentiostat was used in these tests. All potentials were measured with respect to a saturated calomel electrode.

2.4 METALLOGRAPHY

2.4.1 Optical

Standard metallographic polishing techniques were employed for optical metallography. Specimens were mounted in bakelite and polished on SiC papers (200-600 grit) followed by a fine polish on diamond paste polishing wheels (3µ and 1µ).

Occasionally, specimens were electropolished in a 95% Acetic Acid - 5% Perchloric Acid solution at 30V at room temperature.

2.4.2 Electron (TEM)

Heat treated 3.0mm diameter discs were polished manually on 600 grit SiC papers to a final thickness of approximately 0.2mm. For strained, and stress-corroded specimens, 3.0mm discs were spark cut from the tensile specimen of interest. Thin-foil specimens were prepared by jet polishing in a Struers Tenupol polishing unit. A 95% Acetic Acid -5% Perchloric Acid solution was used for polishing this material at ∿ 15°C. The voltage employed was 70V with a current of ∿ 0.12 amps.

Nickel-Plating

As the SCC specimens were sheet tensile specimens, it was necessary to plate the stress corroded specimen with nickel in order to build up a sufficient thickness for preparing TEM foils of the specimen cross-section. The plated specimens were sliced perpendicular to the tensile axis using a high speed slitting wheel, and discs were subsequently spark cut.

The methods of thinning used for these specimens included jet polishing in 30% Nitric Acid ∿ 70% Methanol at -30°C and 20V. Some specimens were prepared by ion-beam thinning.

Microscopy

Transmission electron microscopy was conducted on an AEI-7 1 MeV electron microscope, a JEOL 120 CX TEMSCAN, and a Philips EM 301.

2.4.3 Fractography

After fracture, all specimens were washed in distilled H_2O, and methanol. Fracture surfaces were prepared for examination in a JEOL 120 CX TEMSCAN operating at 40 kV. A thin layer of gold was evaporated on to the mounted specimens to reduce charging.

2.5 "PRE-EXPOSURE" TESTING

As the existence of "pre-exposure" embrittlement of Al-Zn-Mg alloys in water vapour has been well-documented (153 , 154 , 155), it was thought that a similar mode of hydrogen embrittlement may occur in sensitised stainless steel. In order to determine whether this was the case, "in-situ" experiments were conducted on sensitised specimens using the Gas Reaction cell (GRC) in the AEI-7 HVEM. Sensitised specimens were also tested in a specially designed steam cell.

2.5.1 Gas Reaction Cell

The GRC provides a unique opportunity to study gas-metal reactions in the electron microscope. The cell employed in this investigation is a differentially pumped, aperture-limited cell (156). A gas reservoir of approximately 500 ml capacity is created near the specimen between the upper and lower pole pieces. The pressure within the cell can be varied. A diagram of the GRC is presented in Figure 2.4. Development of the the Gas Reaction Cells and related 'in-situ' experiments have been reviewed extensively (157 , 158,159).

For the experiments on type 304 steel, strained and unstrained TEM specimens were used. The cell environment was water-saturated He at 20°C at a pressure of

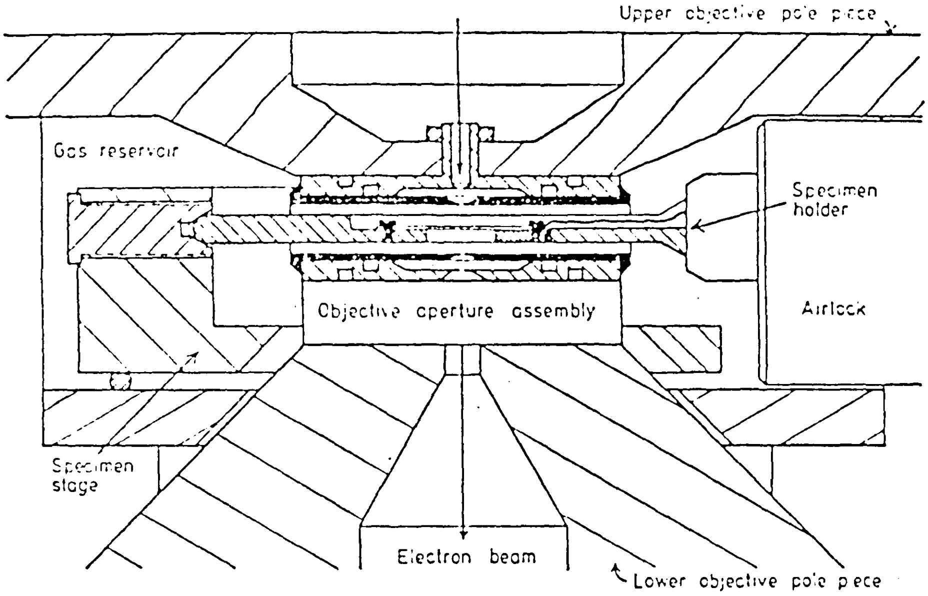

Figure 2.4 Cross Section of a Differentially Pumped Aperture -Limited Environmental Cell With a Single Tilt Hot Stage Inserted. (159).

∿ 100 torr. Experiments were performed at 500 kV and 1 MeV. Video facilities were available for filming the reaction.

2.5.2 High Temperature Steam Cell

The suseptibility of sensitised austenitic stainless steel to intergranular cracking in BWR cooling pipes prompted further study into H_2O vapour as an SCC/HE environment. It was not possible in this investigation to accurately simulate the conditions in BWR cooling pipes: H_2O at 343°C. Therefore, an apparatus was built which enabled the specimens to be exposed to superheated dry steam at atmospheric pressure.

The cell (Figure 2.5) consisted of a 30 mm, diameter quartz tube (sealed at one end) which was inserted in a tube furnace. The open end of the quartz tube, which extended ∿ 1cm outside of the furnace, was sealed with a silicon rubber bung. Two 4.0 mm. diameter pyrex tubes inserted into the furnace enabled the steam to pass over the specimens in the quartz tube. The tube inlet was considerably longer than the outlet tube (located in the cool end of the cell so that the steam would attain furnace temperature before reaching the specimens. The outgoing steam was carried via the outlet tube to a reflux condensor. As the steam condensed, it was collected in a funnel and fed back to the steam source (water-filled flask on hot plate). A thermocouple was inserted into the quartz tube so that the temperature of the steam cell could

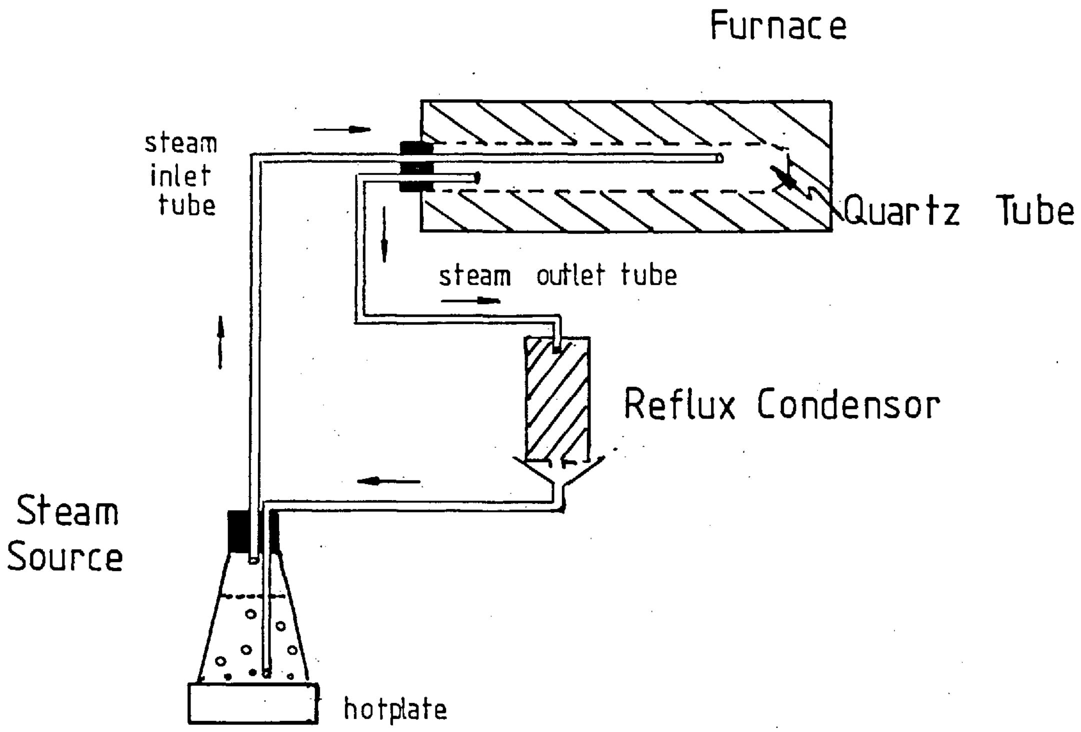

Figure 2.5 Schematic Diagram of High Temperature Steam Cell

be monitored. The temperature during the tests was approximately 320°C.

Two types of specimens were used for these experiments: unstressed, stressed, and pre-stained (5% ε). All specimens were electropolished prior to testing. The specimens tested under stress were U-bend specimens held in a stainless steel clamping device (a Type 304 stainless steel threaded bolt and 2 Type 304 threaded discs).

2.6 EXPERIMENTAL "Fe-Ni-Cr" ALLOYS

The most widely accepted theory for explaining the susceptibility of sensitised austenitic stainless steel to intergranular stress corrosion cracking is based on the existence of a zone where the chromium content is less than the 12 wt.% required for the formation of a passive film. Since the Cr-content is assumed to be the factor determining IGSCC susceptibility, a series of special Fe-Ni-Cr alloys were prepared from pure Fe, Ni and Cr. The compositions of the alloys are presented in Table III.

2.6.1 Alloy Preparation

The "grain-boundary" alloys were melted in a non-consumable electrode arc furnace. The electric arc furnace chamber was evacuated and flushed with argon, after which a Ti getter was melted in order to absorb any residual oxygen. The operating pressure during melting was approximately 5 psi of Argon. The alloys were initially melted in a semi-circular water-cooled hearth, the molten metal being stirred by the action of the Tantalum arc. The alloys were then remelted and cast into ingots in the long flat-bottomed hearth. Each ingot was inverted and remelted several times to ensure a homogeneous melt and minimise porosity through the ingot.

After the final casting, the ingots were homogenised under Ar for 24 hours at 1200°C. Ingots were hot-rolled to a final thickness of ∿ 2mm. and annealed at 1100°C under an Ar atmosphere. Some material was cold rolled to a final thickness of 0.5mm on a bullion mill and annealed at 1100°C for 30 minutes in evacuated quartz capsules. Miniature sheet tensile specimens and 3.0 mm diameter TEM specimens were produced from the cold-rolled sheet prior to the final solution-anneal. All material was water-quenched after heat-treating.

2.6.2 Sample Preparation

Specimens for optical microscopy, transmission electron microscopy, and mechanical testing were prepared in the same manner as described for sensitised austenitic stainless steels.

2.6.3 Polarisation Specimens

Specimens for polarisation experiments were prepared from the 2mm. thick sheet material. The samples were approximately 1 cm^2 in area, and mounted in bakelite. After mounting, a 2mm. diameter hole was drilled and tapped from the back of the mount to the specimen in order to ensure electrical contact between the alloy and the potentiostat. The connection for the working electrode was a plastic encased rod whose tip was threaded. When screwed into the mounted specimen, good electrical contact could be maintained.

The counter electrode for the polarisation tests was a platinum foil. Potentials were measured with respect to a calomel electrode. A Luggin probe completed the cell. All polarisation curves were conducted at a sweep rate of 100mV per min. in dilute H_2SO_4 + NaCl environments (0.12 M H_2SO_4 + 0.024 M NaCl, and $1.x10^{-2}$ M H_2SO_4 + 2 x 10^{-3} M NaCl.)

TABLE III.

Compositions of Experimental Fe-Ni-Cr Alloys

(wt. %)

Fe	Ni	Cr
80.1	10.6	9.2
77.2	10.2	12.5
74.9	10.5	14.5
74.9	9.1	16.0

C ∿ 0.025 in all alloys

CHAPTER 3

STEM MICROANALYSIS

The desire for accurate compositional information of microstructural features has led to the development of analytical electron microscopy - particularly STEM thin foil microanalysis. Other electron beam techniques widely employed for chemical analysis such as electron probe microanalysis and auger electron spectroscopy lack the high spatial resolution required for most microstructural applications. However, by combining microprobe facilities with transmission electron microscopy, it has become possible to improve the spatial resolution for microanalysis and to image desired microstructural features simultaneously. Quantitative chemical analysis combined with high spatial resolution is a relatively recent development, and the technique is still the subject of considerable research. Thus, in this chapter it is proposed to consider in detail the technique, data analysis and experimental calibrations.

3.1 MICROANALYTICAL TECHNIQUE

3.1.1 STEM Analytical Microscope System

The STEM analytical microscope system includes a conventional/scanning transmission electron microscope fitted with an energy dispersive x-ray spectrometer. X-rays from the specimen pass through a Be window to a detector which is a single crystal slice of lithium-drifted silicon. The detector is located between two electrodes across which a bias of several hundred volts is applied. Electron-hole pairs are created by photoelectric absorption and impact ionization. The number of electron-hole pairs is proportional to the x-ray energy. The individual electric pulses are shaped by a resistance-capacity network which also integrates the signal over a short time interval to reduce the effect of noise. The pulses are passed into a multi-channel analyser which separates them on the basis of amplitude so they may be stored in appropriate memory channels. During the analysis period, a histogram is built up in the core store from the pulse signals. This is generally displayed on a CRT screen, the coordinates of the histogram being energy (eV) (horizontal axis) and intensity (vertical axis).

Energy dispersive analysis has the advantages of speed in acquiring a spectrum, and mechanical simplicity. Only one detector is required for analysis, unlike crystal spectrometry. The detector and FET (field effect transistor) are mounted in a small vacuum chamber next to the microscope column. One of the disadvantages of the technique is that the detector must be kept at low temp.(-196°C) to prevent redistribution of lithium under the influence of the polarising field. The Be window isolates the detector from the microscope vacuum, protects the detector head from light, water and oil vapours, and absorbs backscattered electrons. In addition, there is significant absorption of low energy X-rays by the Be window.

3.1.2 Spatial Resolution

A major advancement in microanalysis was the development of EMMA (160) which permitted simultaneous imaging and analysis of microstructural features. Microanalysis, however, was hampered by the poor spatial resolution (approximately 150nm). Although spatial resolution of EMMA and EPMA was limited by the size of the incident electron probe, in STEM (with its probe sizes of ∿2- 20nm) the scattering within the specimen of the incident electrons away from their direction of incidence is the major factor in determining the spatial resolution in microanalysis. A resolution of several hundred angstroms is readily attainable in STEM thin-foil microanalysis (161, 162, 164).

Calculations of spatial resolution have involved Monte Carlo simulations of electron trajectories (163). The Monte Carlo technique has been used to derive depths of x-ray production and backscattering data. Rather than describe the average behaviour of a number of electrons in the specimen, this method sums the effect of a large number of individual electrons. Kyser and Geiss (164) have successfully applied this model to determinations of spatial resolution in Au foils, and in Si_3N_4-Y_2O_3 specimens. The experimental spatial resolution of 180Å was consistent with the results of Monte Carlo calculations.

Reed (165) derived a simple analytical expression to approximate beam spreading in thin foils:

$$b = \tfrac{1}{2}\ 625 \times 10^{7}\ \frac{Z}{E_o}\left(\frac{\rho}{A}\right)^{\frac{1}{2}}\ (t \times 10^{-7})^{3/2}$$

where b = beam spreading in nm

Z = atomic No., E_o = incident beam energy

ρ = density; t = thickness (nm); A = azimuth angle

For most analyses, this simplified expression is adequate.

The factor determining the practical attainable spatial resolution is the beam current of the incident probe. For extremely fine probe sizes, the generation of x-rays (counting rate) is too low for quantitative analysis. Therefore, the use of a larger probe size (and a decrease in resolution) is necessary. Values of 300Å to 500Å for spatial resolution in quantitative thin-foil microanalysis have been reported in the literature (161, 164).

3.1.3 Energy Resolution

The x-ray energy spectrum obtained during the analysis will contain distorted Gaussian peaks centred at the characteristic lines of the particular elements under examination. The width of such peaks is measured at half-maximum peak height (FWHM: full width- half maximum) (Figure 3.1) and is expressed in electrons volts.

Figure 3.1 Illustration of FWHM Parameter for Energy Resolution

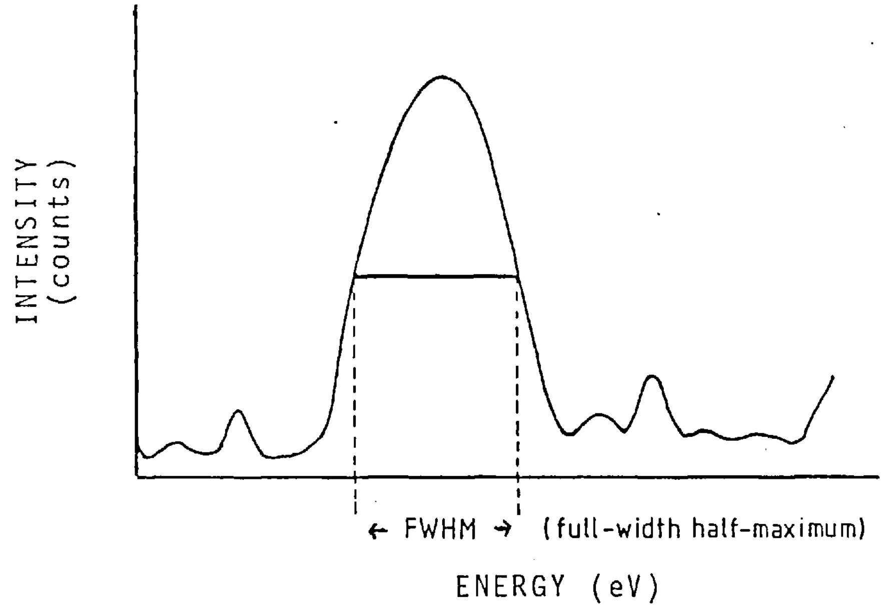

Peak broadening results from statistical fluctuations in the number of electron-hole pairs produced by quanta of a particular energy, and the superimposed amplifier noise (166):

$$\text{energy resolution} = \text{FWHM} = [(\text{FWHM})^2_{\text{noise}} + (\text{FWHM})^2_{\text{statistics}}]^{\frac{1}{2}}$$

The energy resolution decreases as the energy increases; ie. the FWHM value increases due to the increase in the $\text{FWHM}_{\text{statistics}}$ term. The contribution of the noise to energy resolution is constant for all energies.

In energy dispersive x-ray analysis, the energy resolution is a major factor in determining the accuracy of the analysis.

3.1.4 Spectrum Treatment

3.1.4a) Background Subtraction

The principal source of background in the x-ray energy spectrum is the x-ray continuum emitted by the specimen. This background radiation is composed of stray radiation including bremsstrahlung which is generated in the Be window and in surfaces which are not shielded from the detector (167). The overall distortion of a spectrum due to bremsstrahlung will be a unique function of the particular system (167).

For quantitative microanalyses, it is necessary to subtract the background radiation from the x-ray spectrum in order to determine peak areas. Statham (168) has discussed four major techniques for background subtraction: 1) Simple Interpolation and Extrapolation; 2) Empirial Modelling; 3) Background Calculation; and 4) Filtering.

1) Simple Interpolation and Extrapolation

Background subtraction involving interpolation and extrapolation is the least accurate of all methods. Significant errors are produced when the background is not linear - particularly near an absorption edge or in a low energy region.

2) Empirical Modelling

In the empirical modelling method, an expression is obtained which simulates the background shape more closely. An example of such a function derived by Statham (168) to fit the background for various specimens with atomic numbers less than 30 is:

$$B(E) = k \exp\left(- \frac{3.65}{E^2} - 0.26E\right)$$

where B = background

E = energy (keV)

k = constant

Such expressions rely on theoretical and experimental results. Constants are related to the operating conditions and the particular microanalysis system. The equation is of limited use because it only applies over a specific composition range. This method does not consider absorption steps.

3) Background Calculation

This technique provides an expression for the background shape based on theoretical calculations. An equation describing background shape developed by Ware and Reed (169) includes terms for: 1) the generation of photons at a particular accelerating voltage; 2) a self-absorption correction; 3) a correction term for absorption in the Be window, gold surface layer, and Si dead layer; and 4) an empirical correction term. This particular technique also suffers from composition dependence, and it neglects the effect of back-scattered electrons.

Lifshin (170) modified this technique by initially applying absorption corrections and subsequently fitting the background to a quadratic expression. The advantages of this method are that only 2 points are required to define the curve, and that a wide range of compositions can be evaluated. This proceedure, however, is time consuming.

4) Filtering

The final technique, filtering, involves taking the Fourier transform of the spectrum, multiplying the result by a filter, and reversing the transform. In background subtraction, the low frequencies are suppressed by multiplication by weighting factors. When the reverse fast fourier transform of the spectrum is calculated, the resulting spectrum contains no 'low frequency' components i.e. no background. The major limitation of this method is that when some frequencies are common to the background and peaks, a distortion near the baseline will result. These distortions become more important when overlapping peaks are present.

Of all background subtraction techniques, filtering is most effective. It is this subtraction technique which is employed in spectra treatment in the Link System Program employed in this investigation.

3.1.4b Deconvolution of Peaks

Four techniques have been developed to treat the individual peaks.

(1) Integration with Overlap Correction

The 'Integration with overlap correction' technique (168) relies on the proportionality of an integral over a peak (fixed number of channels) to peak area. It is then possible to use ratios of the integrals for the specimen and the standard to determine apparent concentrations in the specimen. The problem of overlapping peaks is reduced by including an overlap factor which is defined as the fraction of integral B over peak B which is included in the integral A over peak A. The resultant correction for sample AB would be:

$$I'_A = I_A - K_{AB}I_B$$

where I'_A = corrected I_A

I_A , I_B = integrated intensities of A, B

K_{AB} = overlap correction factor

(2) Least Squares Fitting

In Least Squares fitting, the experimental data is fitted to a number of model functions (one per peak). the statistical accuracy is slightly improved over the previously described technique, and this method requires no correction factors.

The shape of the peak profile can be obtained from standards, and used as a model in subsequent analyses. The principal advantage of this technique is that the analytical form of the peak need not be determined. However, computer storage facilities are required for the profiles. The background must be subtracted from both standard and sample spectra before fitting the peaks.

The final peak deconvolution technique involves simulating the peak shape by a mathematical expression. With Si (Li) detectors, the peak shapes are generally Gaussian. Difficulties arise when the peaks exhibit deviations from Gaussian shape or when an inappropriate function has been used. Non-linearity in the detector and electronics are additional sources of error.

3.1.4c Iterative Spectrum Stripping

In order to eliminate the difficulties and inaccuracies in determining the background via mathematical functions, Statham developed an 'iterative spectrum stripping' technique. A model for each peak, either calculated or stored, is required, and the area above the local background level is estimated for each particular peak. This area is then subtracted from the spectrum. The major reason for the success of the technique lies in its ability to reduce the local background for all peaks. This stripping technique is illustrated schematically in Figure 3.2. The area subtraction technique is applied to all peaks in the spectrum,

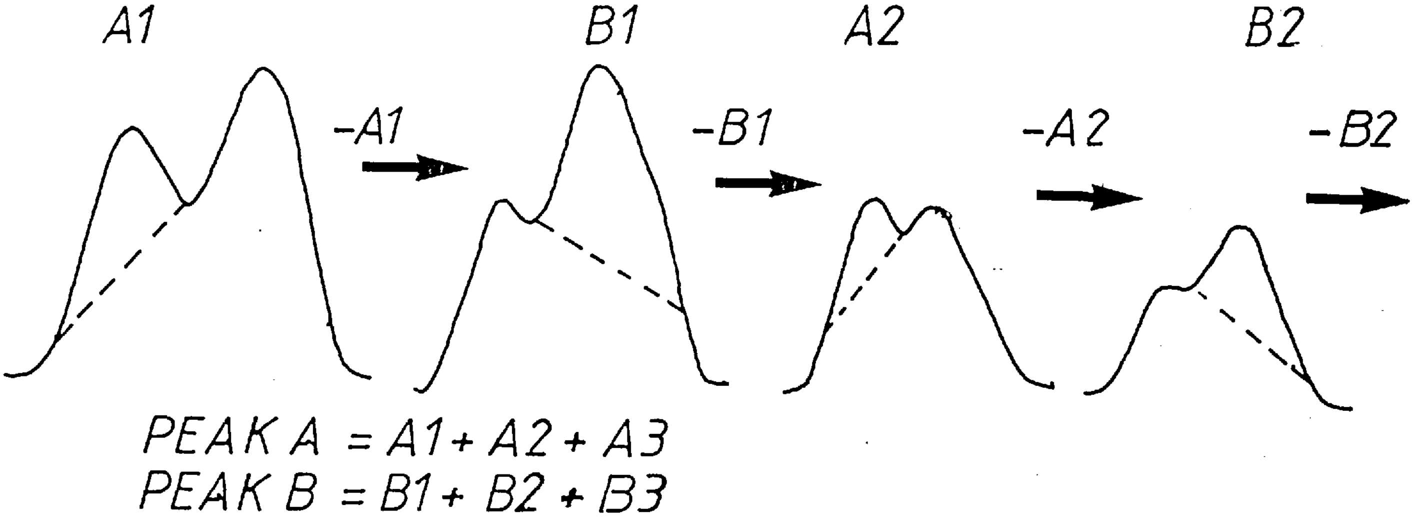

Figure 3.2 Diagram of the Iterative Stripping Principle. Two overlapping peaks are resolved by assessing and subtracting repeatedly until neither peak can be detected.(from Statham, ref. 168)

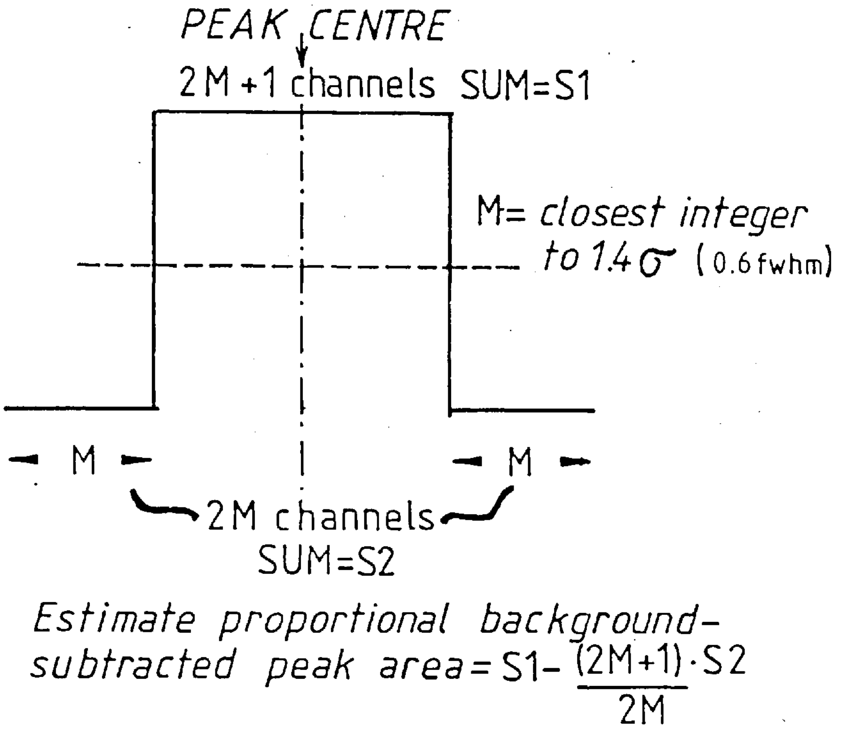

Figure 3.3 'Top Hat' Function For Estimating the Area of a Peak Above Its Local Background. The width is chosen so that, after stripping a peak with slightly incorrect parameters, the net sum only becomes zero when the correct height has been removed. (from Statham, ref. 168)

and the cycle is then repeated. The procedure is completed when no peaks can be detected. Peak heights are determined by summing the areas removed at each iteration.

Peak estimation

Simple interpolation techniques for assessing peak heights can result in erroneous peak area estimates. The stripping process may terminate before the entire peak has been subtracted so that the measured peak height and area will be significantly lower than the true values.

Peak areas can also be estimated by another technique in which the sum of areas over a certain number of channels about the peak is compared with the sum over same number of channels in the wings. This is known as the "top hat" function for determining the peak area above its local background, and is depicted schematically in Figure 3.3.

This technique is limited in that only peaks which are separated by more than 0.66 fwhm can be deconvolved. For K_α/K_α determinations, this limitation is unimportant since all K_α/K_α overlaps are resolvable.

The iterative spectrum stripping techniques is particularly useful in that the background need not be calculated explicitly, and can therefore be applied to any x-ray spectrum. Errors will arise when the background is not linear over the peak range, near absorption steps, or in the low energy region (significant absorption by the Be-window).

3.1.5 Absorption

X-rays generated within the specimen by the incident electron beam may be absorbed by the specimen, so that the measured intensity will be reduced. Absorption is dependent upon the absorption coefficients for each element in the specimen, and the path length traversed by the x-rays within the specimen.

To correct the analysis for absorption effects, the x-ray absorption coefficients and specimen thickness must be known. Techniques for determining the specimen thickness include the Hall method (171) whereby the total intensity in a single energy band of continuum is used as a measure of mass thickness, convergent beam diffraction, or parallax measurements of contamination spots (on top and bottom surfaces).

In thin-foil quantitative analysis, the effect of absorption is generally ignored. The "thin-film" approximation of Philibert (172), applied to electron-transparent specimens (at 100kV), is based upon the assumption that the path length of the x-rays through the specimen is so small so that very little, if any, absorption would occur. Bentley and Kenik (173) have demonstrated that absorption effects are not significant in austenitic stainless steel if a "viewable image" can be obtained at 120kV. This criterion is subject to qualifications regarding microscope operating conditions (174). Although the "viewable image" criterion is not exact, it provides a general indication as to whether absorption effects will be significant.

The effect of absorption on the measured intensity of a characteristic x-ray line is described by (175,176) :

$$I'_A = I_A \, e^{-(\mu/\rho)^A_{spec} \, \mathrm{cosec}(\psi) \, \rho\frac{t}{2}}$$

where I_A = generated intensity of A x-rays

$(\mu/\rho)^A_{spec}$ = mass absorption coefficient of A by the specimen.

μ = take-off angle

ρ = density of the specimen

t = specimen thickness

This expression, evaluated for chromium in the Fe-Cr-Ni austenite near sensitised grain boundaries confirmed the "viewable image" criterion of Bentley and Kenik (173). For a foil ∿ 2000Å in thickness (a relatively thick foil), absorption of Cr x-rays by the specimen was minimal.

3.1.6 Fluorescence

Absorption of characteristic a continuous x-rays by an element results in the enhancement of the measured x-ray intensity due to fluorescence. Fluorescence of one element A by the characteristic radiation of another element B in the specimen will arise only if the energy of the radiation from B is greater than the energy of the absorption edge of A. This additional characteristic radiation of A is indistinguishable from the primary A radiation.

There are corrections for fluorescence resulting from characteristic and continuum radiation. The most significant type of fluorescence, however, is due to characteristic x-rays rather than the continuum radiation. The contribution of the latter to the measured spectrum is generally small, so the correction is usually neglected.

It has been demonstrated by Lorimer (177) that corrections for fluorescence will be required in thin specimens if strong bulk fluorescence effects occur. Nockolds et al (178) derived an expression relating the intensity of A radiation fluorescence in an annulus by B radiation from a point P (see Figure 3.4) :

$$I_F^A = I_B \frac{T}{2} (0.923 - \ln(\mu_B T)) C_A \mu_B^A \omega_{K_A} \frac{r_A - 1}{r_A}$$

where T = mass thickness of specimen = Z(thickness). ρ(densit)

$\mu_{B1}\mu_B^A$ = mass absorption coefficients of B radiation in the specimen, and in element A

C_A = weight fraction of element A

ω_{K_A} = fluorescence yield of A; r_A = absorption edge jump ratio.

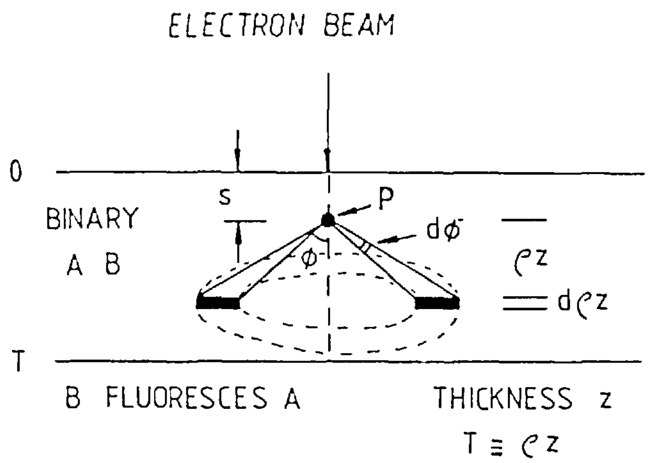

Figure 3.4 Schematic Model of Fluorescence in a Thin Foil (from Nockolds et al.(178))

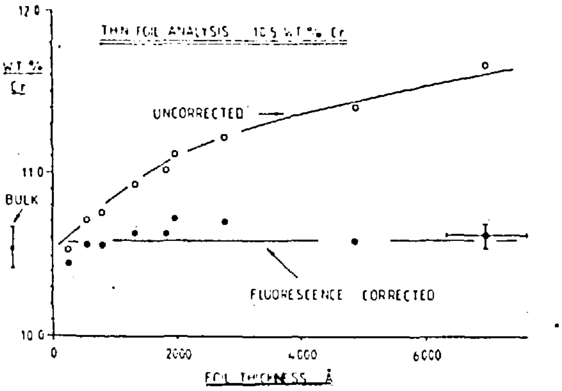

Comparison of uncorrected and fluorescence corrected data as a function of thickness for a 10.5 wt%Cr - 89.5 wt%Fe alloy.

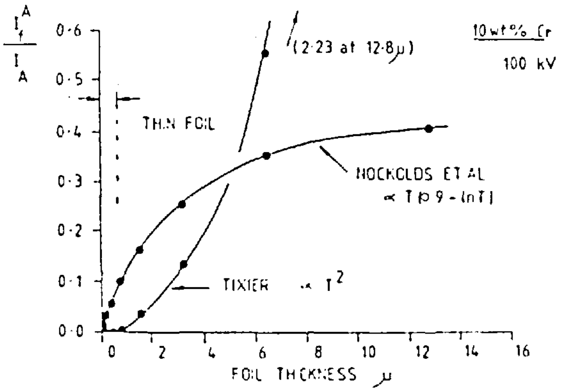

Comparison of fluorescence correction predicted by the present model and that of Tixier for a 10 wt%Cr - 90 wt%Fe alloy as a function of thickness.

Figure 3.5 The Effect of Fluorescence in Quantitative Analysis of Thin Foils of 10.5 Cr - 89.5 Fe. (from Nockolds et al (178))

Nockolds et al.(178) demonstrated the effect of fluorescence in quantitative analyses of thin-foils of 10.5% Cr- 89.5% Fe. Figure 3.5 illustrates the effect of fluorescence on the apparent Cr concentration, and the result of applying the fluorescence correction.

3.1.7 Quantitative Microanalysis

There are two techniques available for quantitative microanalysis: "standard" and "standardless" processes (179). In "standard" microanalysis, the sample is analysed by comparing its x-ray spectrum with that of a thin-foil "standard" of known composition. The mass fractions of the elements present can be calculated after applying the necessary corrections for absorption , atomic number effects in the standard and the ionisation cross-section of the specimen.

With the 2nd technique it is possible to determine the composition of a sample by using the integrated intensities of the k peaks of the elements, and particular detector data. Basically, the ratio of the characteristic integrated intensities of 2 elements is directly proportional to the ratio of concentration of theose elements(180):

$$\frac{I_x}{I_y} = k_y^x \frac{C_x}{C_y} \qquad \text{(neglecting absorption + fluorescence)}$$

where I_x, I_y = integrated intensities of elements x,y.

C_x, C_y = compositions of x, y in wt%.

The proportionality constant K is a function of the relative characteristic intensities generated, and the relative efficiency of the detector in measuring those intensities. It is independent of kV and t. K can be calculated, or experimentally determined for thin-film standards. A comparison of calculated K_{Si} values (for Silicon-based systems) with experimental constants obtained by various workers (181) has shown that there is close agreement in values from energies greater than 3 keV. Below (Si K_α), the calculated values are lower than those experimentally determined.

The question of accuracy in quantitative microanalysis using "standard" and "standardless" programs was examined by Bengtsson and Easterling (179). A variety of specimens were analysed, and it was concluded that there were no major advantages in employing analysis programs based on standards. Indeed, in the case of austenitic stainless steel, greater accuracy was obtained through the use of a "standardless" program (179).

3.1.8 Contamination

During the course of an analysis, it is possible to build up significant peaks of contamination. These cones which develop on the foil surfaces can form as a consequence of the localised heating of the specimen by the electron beam and the subsequent decomposition of hydrocarbons (182). Silicon has been detected in x-ray analyses of contamination spots, which suggests that the contamination arises from vacuum pump oils or grease. Zaluzec and Fraser (183) observed a small Si K_α peak in a spectrum from a thin β- NiAl specimen, and correlated it with the accumulated contamination on the specimen.

A serious effect of contamination is reported to be a loss in spatial resolution arising from beam broadening occurring as the probe passes through the contaminant (183). In an investigation of grain boundary segregation in Fe-Ni alloys, Doig and Flewitt (182) additionally examined the effect of contamination on analysis. After detecting Sn at the grain boundary, a region 200Å from the boundary, but still within the contamination spot, was analysed. The absence of a Sn K_α peak in the spectrum enabled them to conclude that the spatial resolution was not measurably reduced by the presence of significant contamination.

Preferential absorption of low energy x-rays by the surface contamination has been reported by Zaluzec and Fraser (183). Their results are based upon anlayses of NiAl (Ni K_α - medium energy line; Al K_α - low energy line). An additional effect of contamination may be the generation of bremsstrahlung x-rays as the probe interacts with the contaminant. This can affect quantitative measurements of peak-to-background ratios, and therefore mass sensitivity.

In addition to these disadvantages, there are benefits of contamination. Firstly, contamination spots clearly indicate the area of analysis so that an accurate record of the location may be obtained. Contamination spots are also useful in detecting specimen drift during an analysis. Finally, an indication of the specimen thickness may be ascertained from contamination markings. This method involves tilting the specimen through a fixed angle and measuring the displacement of the contamination spots on the top and bottom surfaces of the specimen.

By improving the vacuum system of the microscope, it is possible to eliminate the Si-contamination. The extent of contamination can also be substantially reduced by exposing the specimen to a fully overfocussed beam ("flooding the specimen") for approximately 15 minutes prior to analysis (184). This prevents the local decomposition of hydrocarbons.

3.2 EXPERIMENTAL PROCEDURE

The quantitative microanalyses performed in this project were conducted on a JEOL 120 CX Temscan equipped with Link Energy Dispersive X-ray Microanalysis facilities. The operating voltage for all microanalytical experiments was 100kV.

A series of essential calibrations were performed so that the system could successfully be employed for accurate microanalytical studies. This section is therefore sub-divided into two parts: 1) calibration and 2) experimental quantitative analysis.

The Link EDX Microanalysis equipment includes the RTS-2/FLS (Ratio-Thin Section/Fitted Least Squares) series of programs for quantitative analysis which were used in this investigation. After proper calibration, all overlapping K, L, or M series peaks can be deconvolved. These programs are valid for normal or non-normal beam incidence, and also consider the possiblity of non-normal incidence of x-rays at the detector surface.

3.2.1 Calibration

3.2.1a Standard Calibration

Program 5 is selected for construction of a standard file. Before the standard spectra are acquired, a Co standard (bulk) specimen is analysed so that the spectrometer gain can be established. The standards, prepared from pure elements (thin-foil or bulk specimens), are analysed and the values of the highest and lowest energy peaks in the series are submitted for each spectrum. This enables the background to be subtracted, so that the profiles can be stored on disc and used in subsequent quantitative microanalyses, as described in Section 3.1.4.

3.2.1b Hole Counts

The result of x-ray continuum fluorescence can be monitored through the 'hole count' for the microscope. A 'hole count' refers to the positive x-ray count obtained when the incident electron probe is positioned in a hole in the specimen. These x-rays are characteristic of the specimen and surrounding environment. Uncollimated radiation (resulting from electron scattering around the condenser aperatures) can cause fluorescence in the thick areas of the specimen.

Tests were conducted in the JEOL 120X to determine the hole count during analysis. Relative intensities were the sample, and finally bulk material. A slight improvement was noted when condenser aperature 2 (300 μm) was used rather than condenser aperature 3 (200 μm). The hole count, however, was minimal - contributing approximately 0.5% to the x-ray spectrum from a typical analysis.

3.2.1c Determination of K^{Cr}_{Fe} and K^{Ni}_{Fe}

Having the necessary standard profiles on disc, it is possible to perform RTS analyses on thin-foil specimens. The Cliff-Lorimer method described previously (Section 3.1) relied on theoretically or experimentally determined constants based on Silicon. It is possible to use any element as a base, and so in this research all constants have been determined with respect to Fe.

The K^{x}_{Fe} values were obtained experimentally from x-ray spectra of Fe-Ni-Cr alloys, the compositions of which had been determined by two independent chemical analyses. Thin-foil specimens of each alloy were prepared by the jet-polishing technique described in Section 2.4. The count time for all analyses was 100 sec. A series of 7 general analyses for each alloy were conducted. For each acquired spectrum, the particular K_{Fe}^{Cr} and K_{Fe}^{Ni} values were calculated. The mean values for the Fe/Cr and Fe/Ni constants were determined after the elimination of the highest and lowest individual values. The results of these analyses are presented in Table IV.

3.2.1d Fit Index

In the quantitative microanalysis program (No.2), a measure of the degree of fit between the standard profile and the unknown spectrum is calculated. The Fit Index is the ratio of the systematic errors in the fit to the random statistical errors, and is defined as:

$$F.I. = r^2/\sigma^2$$

where $\underline{r}$ = residual left after subtraction of filtered peak profile from the filtered spectrum.

σ = standard deviation for a given channel.

Poor fit indices can arise from sources such as spectrometer drift or inaccurate standard profiles. For all quantitative analyses, only processed spectra which had a Fit Index of approximately 2 or less were considered to be valid.

TABLE IV.

Experimental Determination
of
K_{Fe}^{Cr} and K_{Fe}^{Ni}

I_{Cr}	% error	I_{Fe}	% error	I_{Ni}	% error	K_{Fe}^{Cr}	K_{Fe}^{Ni}
Fe- 10.2 Ni- 12.5 Cr							
5216	2.9	27210	1.2	3331	4.5	0.845	1.078
5037	2.5	27001	1.2	3041	3.3	0.867	1.171
5945	2.8	32611	1.1	3981	4.1	0.889	1.081
6331	2.6	33418	1.0	4346	3.9	0.855	1.016
5716	2.8	29805	1.1	3770	4.1	0.845	1.043
6362	2.6	32000	1.1	3835	4.2	0.815	1.101
Fe- 10.5 Ni- 14.5 Cr							
6988	2.5	33378	1.1	4061	4.0	0.927	1.150
6157	2.7	29337	1.2	3657	4.2	0.924	1.121
7477	2.4	34393	1.1	3979	4.1	0.892	1.210
7167	2.9	32179	1.1	4038	4.0	0.871	1.116
6693	2.5	31023	1.1	3851	4.1	0.899	1.128
7913	2.4	36020	1.1	4314	4.0	0.883	1.169
Fe- 8.6 Ni- 18.0 Cr							
8401	2.2	31924	1.1	3280	4.6	0.901	1.100
7839	2.3	29610	1.1	3029	4.8	0.895	1.105
8666	2.2	32465	1.1	3212	4.7	0.888	1.142
8200	2.3	30269	1.1	2890	5.1	0.875	1.183
9014	2.1	33475	1.1	3670	4.2	0.880	1.031
8446	2.2	31422	1.7	3174	4.7	0.882	1.119

Average value of $K_{Fe}^{Cr} = 0.890$

Average value of $K_{Fe}^{Ni} = 1.110$

3.2.2 Experimental Quantitative Microanalysis

3.2.2a Tilt Angle

Preliminary tests were conducted on thin foil specimens of known composition in order to evaluate the effect of specimen tilt on the measured composition. Although a tilt of 40° towards the detector is recommended, there was no significant effect of deviations of ± 7°. This flexibility is important for quantitative studies in the vicinity of grain boundaries, as the boundary plane should be oriented parallel to the incident beam. The diagram in Figure 3.6 illustrates the specimen - detector geometry.

3.2.2b Probe Size and Spatial Resolution

All analyses were conducted at either 'low mag' (200Å) or 'standard' spot size (100Å). No effect of probe size on measured composition was observed.

The spatial resolution of the analysis was determined from beam broadening calculations to be approximately 300Å. The contamination spots produced were ∿ 500Å in diameter, so analyses were conducted at 500Å intervals.

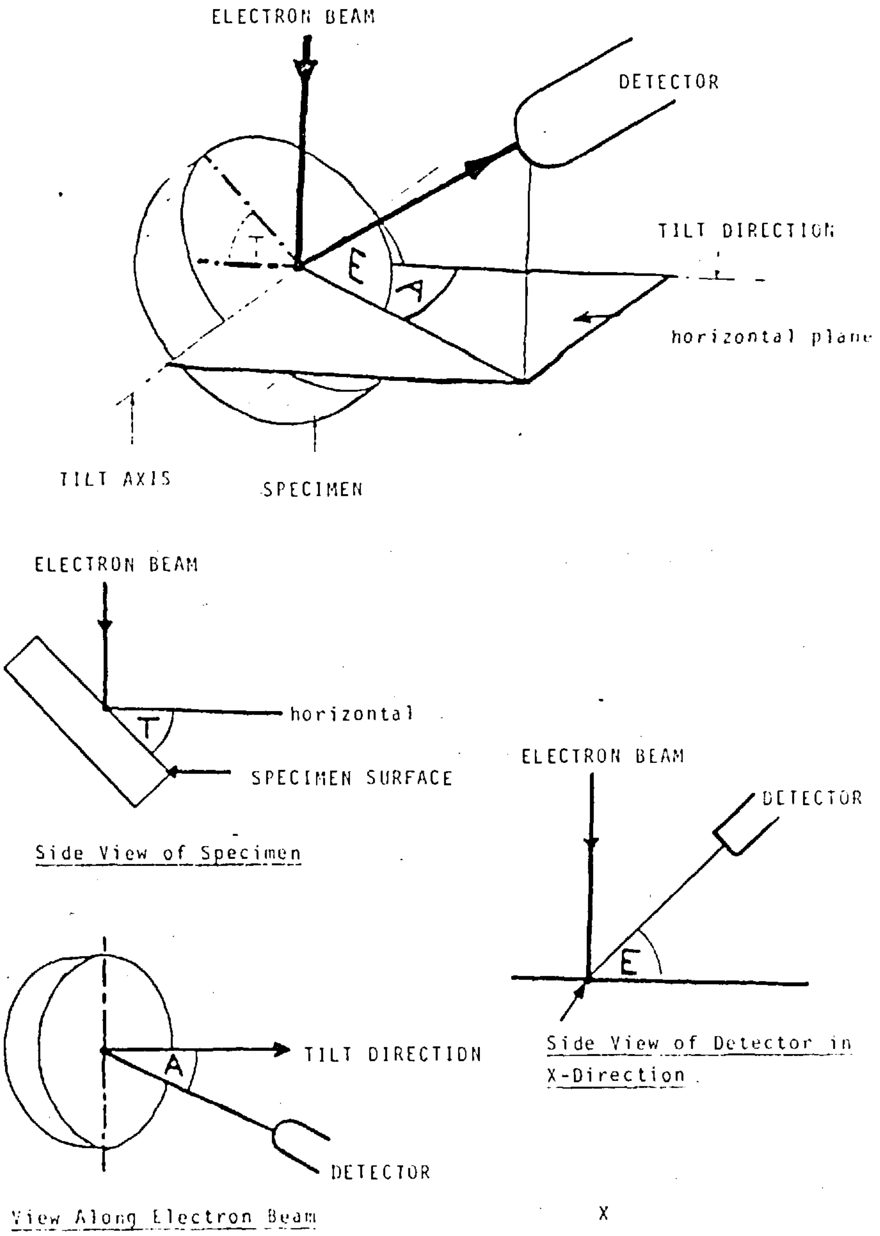

Side View of Specimen

Side View of Detector in X-Direction

View Along Electron Beam

Figure 3.6 Diagram of Beam-Specimen-Detector Geometry (from Link System Manual, ref. 165)

CHAPTER 4

STRUCTURE AND PROPERTIES OF THE HEAT-TREATED AUSTENITIC STAINLESS STEEL

4.1 MICROSTRUCTURE

4.1.1 Solution Annealed Material

A heat treatment of ½ hour at 1120°C resulted in an equiaxed, fully recrystallised structure. Representative electron micrographs are presented in Figure 4.1. The grain size of this material, as determined by the linear intercept method, was approximately 50μm.

4.1.2 Sensitised Material

Two sensitisation variables were examined in this investigation: temperature of sensitisation, and duration of the heat-treatment. As the effects of these variables on the resultant carbide morphologies are closely related, the development of the carbides will be discussed with respect to both parameters. The general observation of the effect of temperature and time of sensitisation was that carbide precipitation is enhanced at higher temperatures, or by long sensitisation treatments, with more profuse precipitation occurring on high-angle grain boundaries.

Precipitation occurs initially on high-angle grain boundaries, with carbides nucleating on incoherent twin boundaries only after longer periods (approximately 48 hrs)

Figure 4.1 Representative Electron Micrographs of Solution Annealed Type 304 Austenitic Stainless Steel

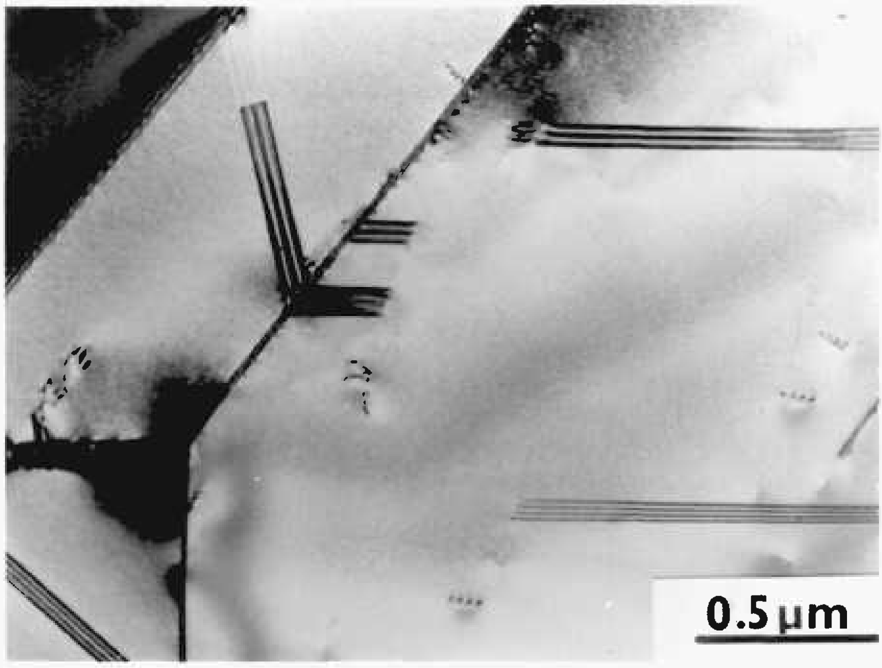
0.5 µm

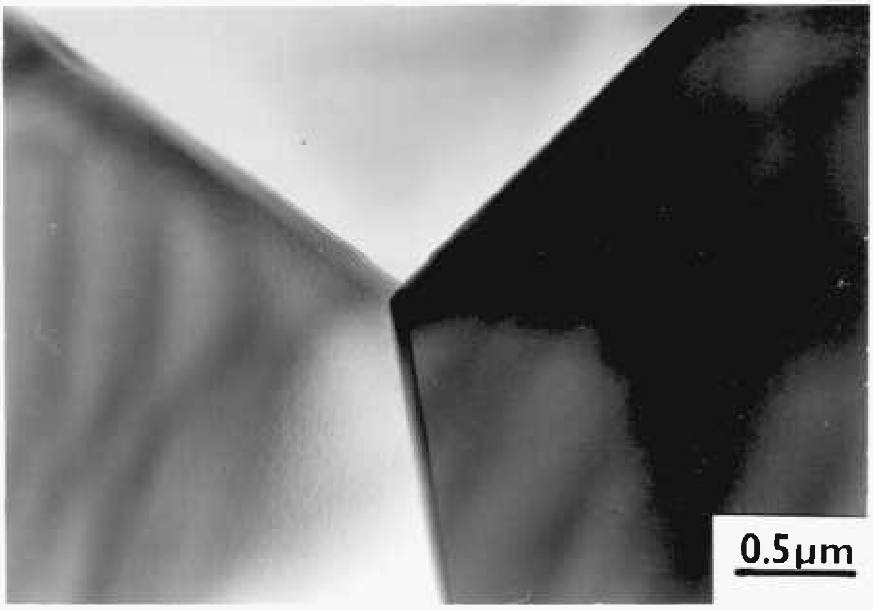
0.5µm

as illustrated in the micrographs in Figures 4.2-4.4. All carbides were observed to be discrete particles, although various morphologies developed as sensitisation time increased. This change in morphology made a quantitative analysis of the effects of temperature and time impossible in this investigation.

Carbides initially appeared as fine precipitates in TEM examination. With a prolonged ageing, they developed morphologies similar to those described by Mahla and Nielsen (9). The dendritic or needle-like shape of the carbide is to be expected on the basis of free energy considerations. The dendritic morphology is favoured as it minimises the strain and interfacial energies of the precipitates.

$M_{23}C_6$ carbides are generally semi-coherent with one grain, but they may exhibit an orientation relationship with both grains depending on the nature of the grain boundary. The observed relationship is $(111)_{M_{23}C_6} || (111)_\gamma$; $<110>_{M_{23}C_6} || <110>_\gamma$ (185, 186). Therefore, by maximising their surface area, the precipitates are maximising the semi-coherent interface and minimising the total free energy.

As the particles grow, the dendrites fragment, and regular geometric arrays of carbides can be observed. A tetrahedral morphology can result, as illustrated in Micrograph B in Figure 4.2. The geometric morphologies are developed due to the preferential orientation of the carbide with the austenite, and the competition between strain and interfacial energy effects (minimise the total free energy).

Figure 4.2 Various Carbide Morphologies in Sensitised Type 304 Stainless Steel.

A) Tetrahedral Array of Carbides

B) Needle-like Carbides

Figure 4.3 Development of Sensitised Microstructure

A) Sensitised for ½ hr. @ 675°C

B) Sensitised for 72 hrs. @ 675°C

C) Sensitised for 72 hrs. @ 675°C; note the precipitation on the incoherent twin boundaries

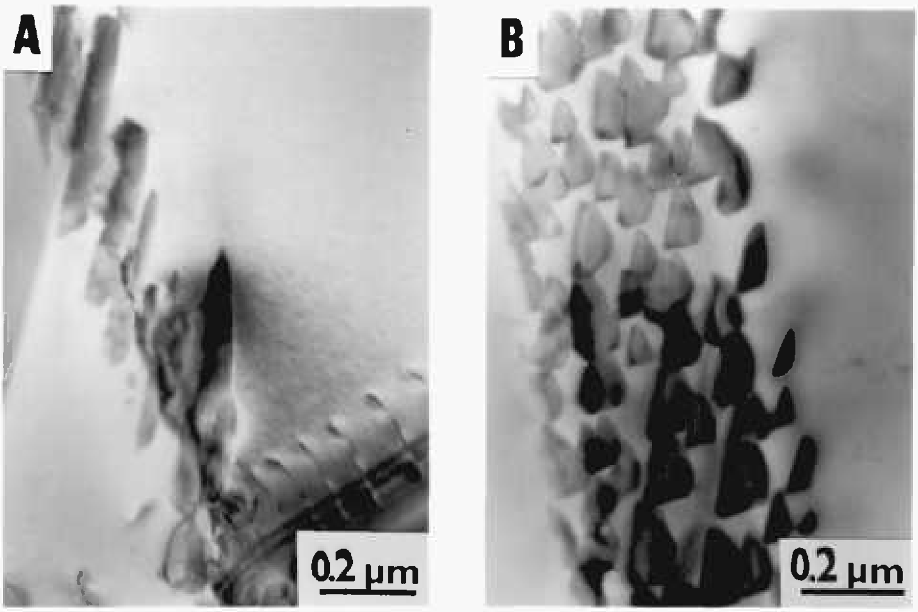
A
0.2 µm
B
0.2 µm

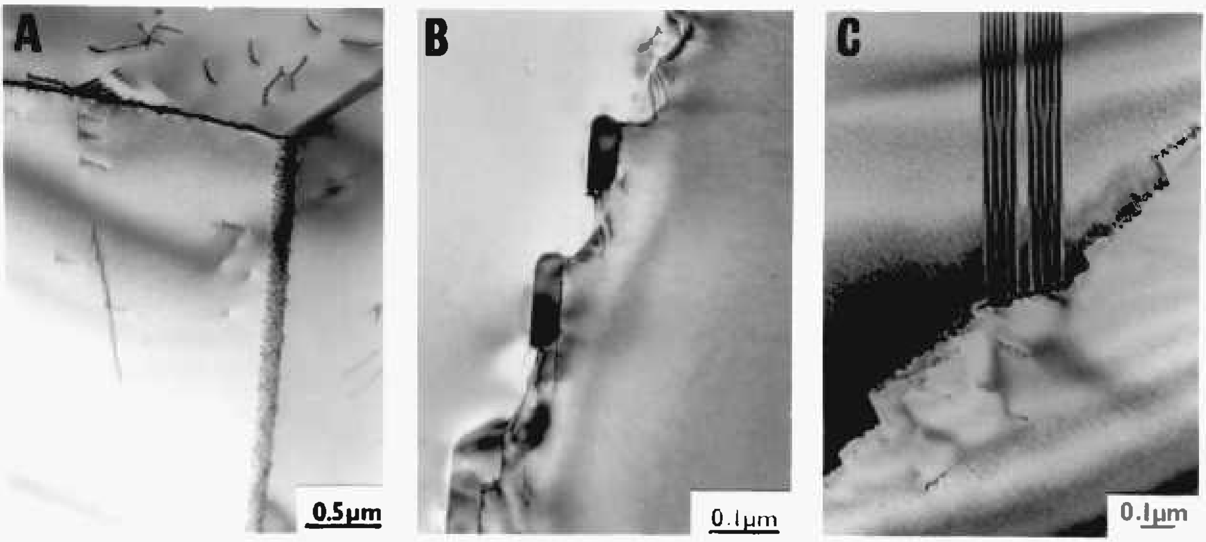
A
0.5µm
B
0.1µm
C
0.1µm

Figure 4.4 Dendritic Carbide Morphologies Observed After Intermediate Sensitisation Treatments (24 hrs. @ 675°C)

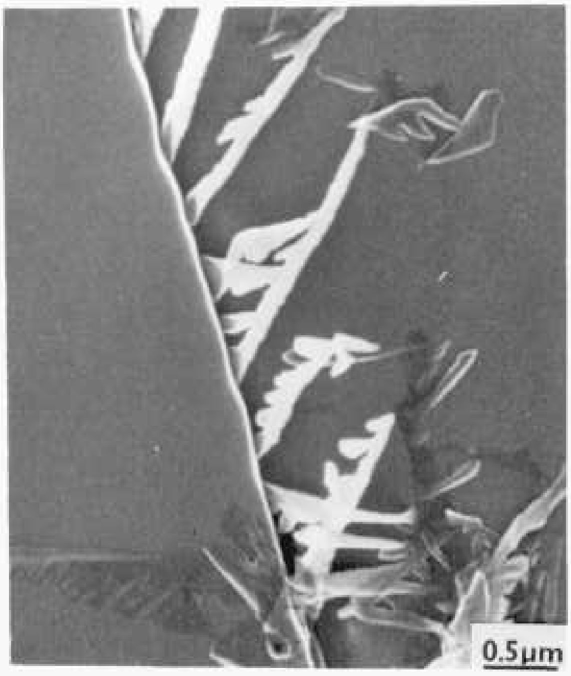
0.5μm

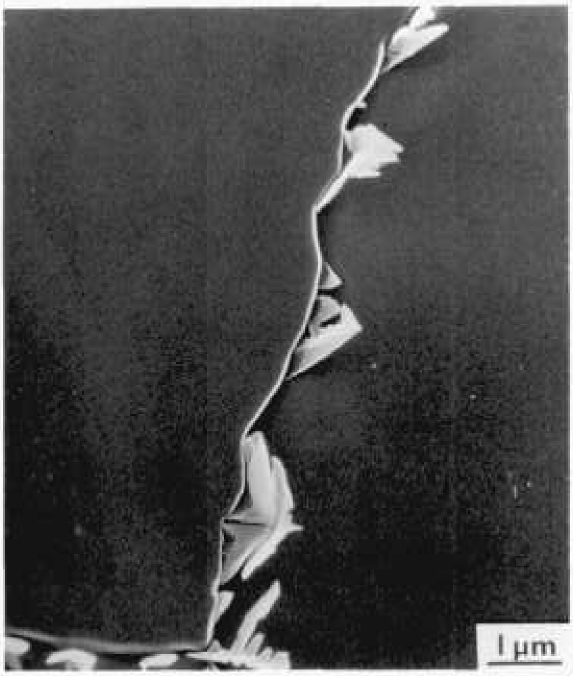
1 μm

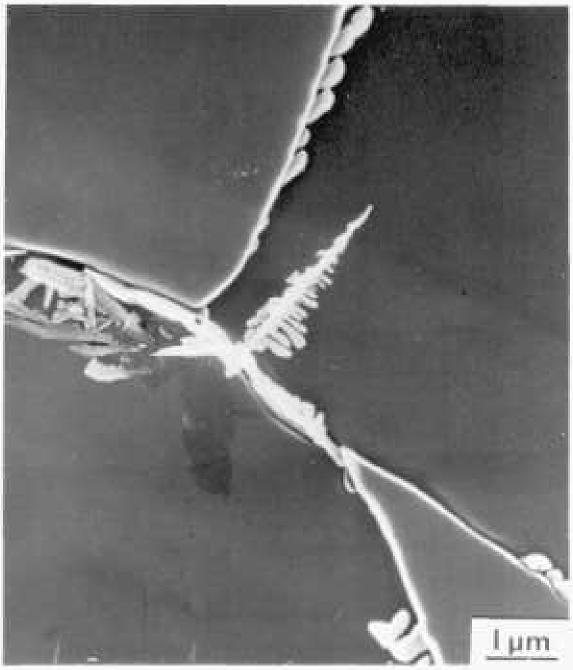
1 μm

4.2 QUANTITATIVE MICROANALYSIS OF HEAT-TREATED STEEL

The existence of the chromium depleted zone in sensitised stainless steels has been indirectly confirmed by numerous techniques which rely on the difference in electrochemical behaviour of the matrix and the regions adjacent to the grain boundaries. Preliminary STEM quantitative microanalyses reported by Pande et al. (187) on two heat-treated austenitic steels (24 hrs @ 600°C and 48 hrs @ 800°C) provided a general indication of the grain boundary chromium depletion, but failed to confirm the hypothesis that the chromium concentration falls below ∿ 12wt.% near the grain boundary. Rao and Lifshin (188) examined one sensitisation treatment in an introductory study, and have claimed to detect 5% Cr at a sensitised grain boundary. All sensitised boundaries were assumed to exhibit identical profiles, although no evidence was presented to support this assumption. These two preliminary studies indicated that STEM quantitative microanalysis could be successfully employed to characterise the sensitisation process.

4.2.1 Experimental Chromium Profiles

4.2.1a Sensitised Steel

It was found that no unique solute profile could adequately characterise a particular sensitisation treatment. Therefore, the results of the quantitative microanalyses representing the most severe depletions for each sensitisation treatment are presented in graphical form in Figures 4.5 - 4.7. Each experimental point is the average Cr content of the analysed volume. The approximate diameter of the analysed cylinder is indicated by the horizontal bar at each experimental value of the Cr concentration, while the vertical error bar represents one standard deviation.

The development of the Cr concentration profile with time was successfully monitored with this quantitative microanalytical technique. It was possible to detect significant depletions in the early stages (15 min @ 675°C) of the precipitation process. As the sensitisation treatment continued, the extent of the chromium-depleted zone increased from approximately 700Å after 15 minutes at 675°C to 2500Å after 100 hrs. This broadening of the depleted zone was accompanied by a decrease in the experimentally measured Cr-concentration near the grain boundary. After 24 hrs. at 675°C, the minimum Cr-content within 200Å of the grain boundary ranged from 10.5 wt.% to 8.5 wt.%. These experimental results confirm the existence of a zone in which the Cr-concentration is less than 12 wt.% as initially proposed by Bain et al. (64) in 1933.

Material which had been sensitised at 600°C was also examined in order to study the effect of temperature on the resultant Cr-profiles. The widths of the depleted zones were found to be substantially less than those observed after the 675°C heat treatments for the same periods, and the profiles were observed to be steeper than the 675°C profiles. This explains why the experimental values of the

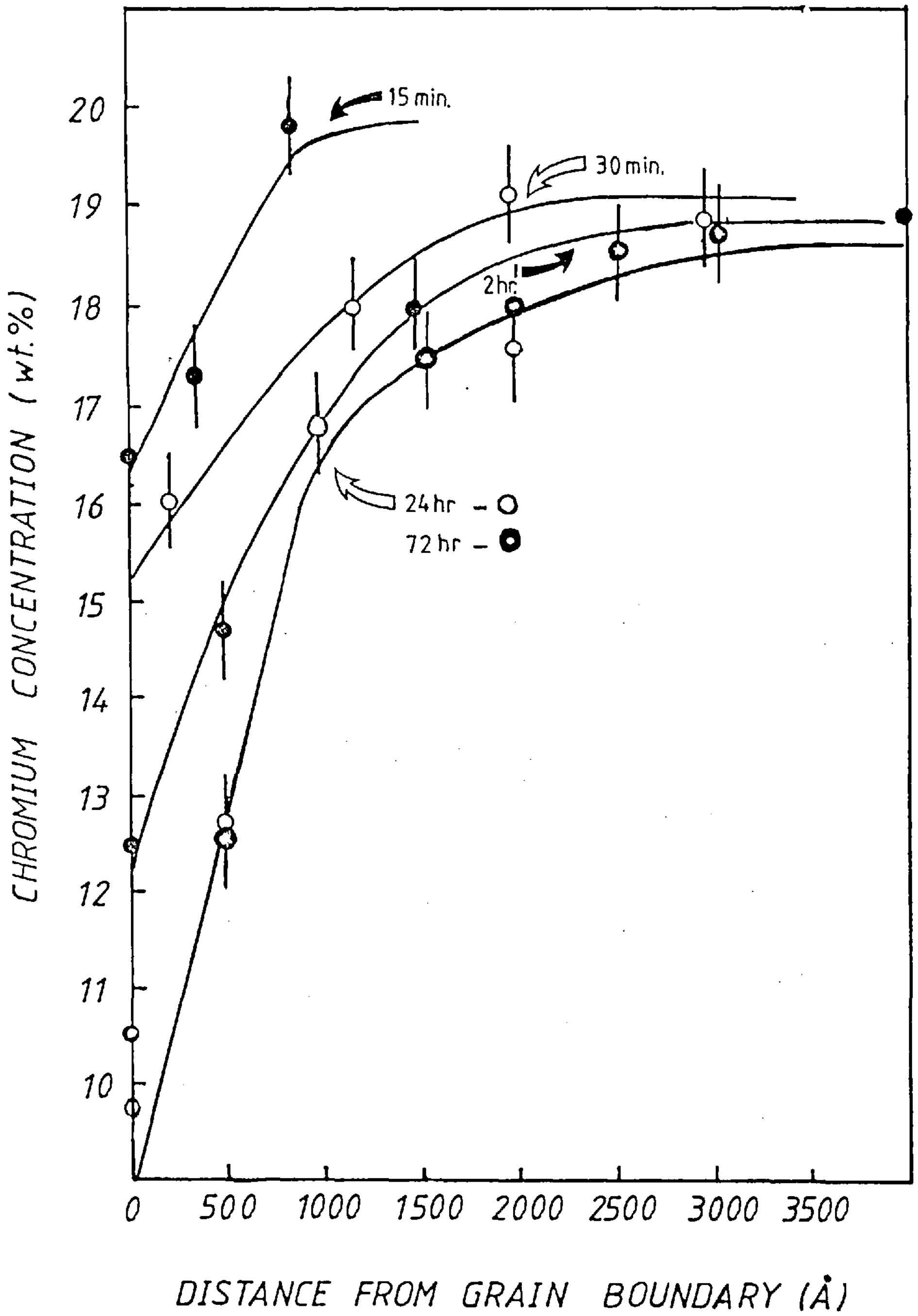

Figure 4.5 Chromium Concentration Profiles Developed During Sensitisation at 675 °C.

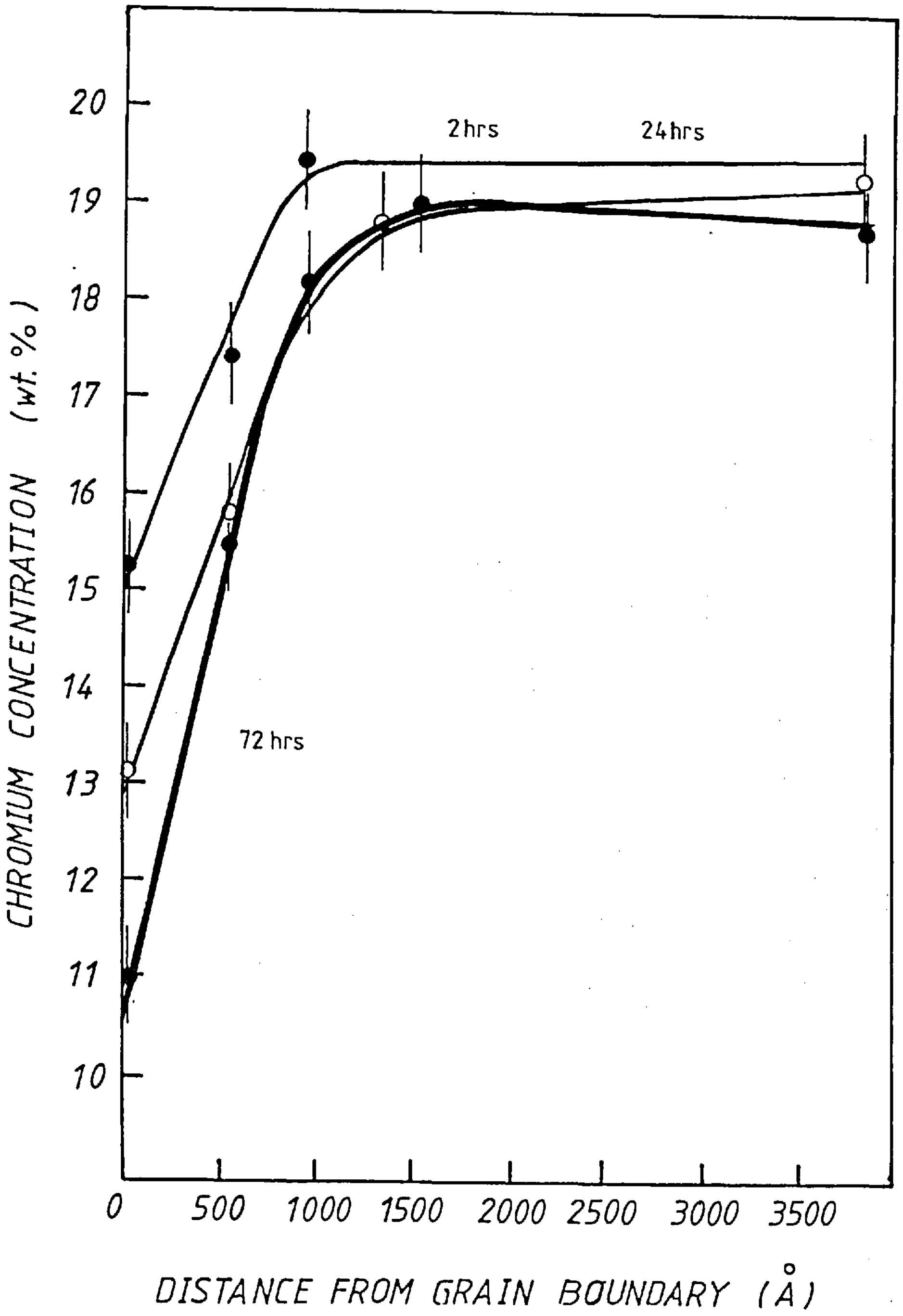

Figure 4.6 Chromium Concentration Profiles Developed During Sensitisation at 600 °C.

Cr contents next to the grain boundary are higher for the 600°C material than for the 675°C specimens. Since the region of analysed material is approximately 500Å in diameter, the experimental values for the 600°C specimens will be the average over a wider range of Cr compositions than those values obtained for the 675°C material. By reducing the temperature of sensitisation, the chromium content in equilibrium with $(Cr, Fe)_{23} C_6$ will decrease, as shown in the thermodynamic analysis of Tedmon et al. (66). Experimental evidence in support of the reduction in the equilibrium Cr content will be presented in Section 4.4.

The lack of a characteristic solute profile to describe a particular sensitisation treatment was attributed to the fact that the nature of the profile is dependent upon the type of grain boundary (and grain boundary plane) and the extent of precipitation rather than the specification of particular sensitisation conditions (time and temperature).

Solute profiles illustrated in Figure 4.7 were typical of those obtained at coherent and incoherent twin boundaries after 72 hrs. at 675°C. No depletion was detected at coherent twin boundaries, while a narrow depleted zone was observed at incoherent twin boundaries.

4.2.1b 'Stabilised' Steel

The susceptibility of austenitic stainless steels to intergranular stress corrosion is eliminated after heat-treating in the vicinity of 900°C. The "stabilised" microstructure is characterised by the precipitation of large

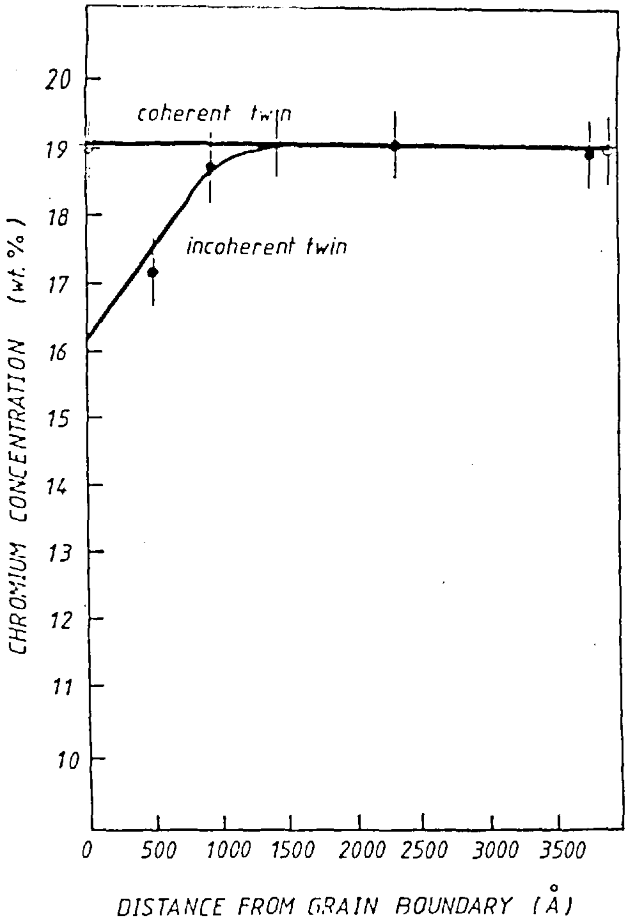

Figure 4.7 Chromium Concentration Profiles From Incoherent and Coherent Twin Boundaries (72 hrs. @ 675°C)

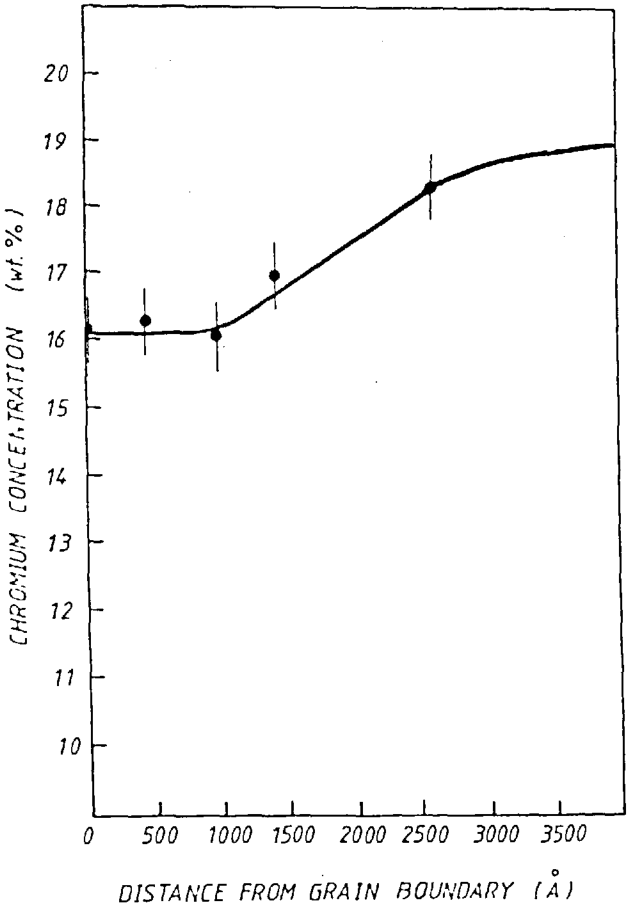

Figure 4.8 Chromium Concentration Profile After 2 hrs. @ 900°C.

$(Cr,Fe)_{24} C_6$ carbides along grain boundaries. It has been proposed that the reason for the immunity to intergranular attack is the nature of the chromium profile at the grain boundaries (susceptibility to IG attack being determined by the zone in which the Cr content is less than ∿ 12 wt.% so that passive film formation is eliminated).

To confirm this hypothesis regarding "stabilised" austenitic stainless steel, specimens which had been annealed for 1 hr. at 900°C (after solution annealing) were prepared for TEM examination and STEM quantitative microanalyses. Microanalysis of the grain boundary regions confirmed the minimum detectable chromium content was ∿ 16 wt.%. This profile is presented in Figure 4.8 .

At the elevated annealing temperature (900°C), the equilibrium chromium concentration of the austenite with the carbide is approximately 16 wt.%. In addition, D^{γ}_{Cr} is raised significantly ($D^{\gamma}_{Cr} = 10^{-12} cm^2/sec$ at 900°C), so that a wide depleted zone cannot develop.

4.2.1c Solution Annealed Steel

No segregation was detected in the solution annealed specimens.

4.2.2 Comparison With Theoretical Predictions

The development of the chromium depleted zone during sensitisation has been analysed by Strawström and Hillert (65), and Tedmon et al. (66). In Stawstrom and Hillert's model, it is assumed that the chromium content adjacent to a carbide is thermodynamically determined by the alloy- $M_{23}C_6$-C equilibrium. A similar assumption is made by Tedmon et al., but, in their analysis, the Cr content along the grain boundary is not assumed to be constant. Another difference between the two models is the importance of grain boundary diffusion. The volume diffusivity of Cr in γ is employed in the calculations of Stawström & Hillert, whereas both volume and grain boundary diffusivities are considered by Tedmon et al. in their determination of the extent of the Cr- depleted zone.

It is possible to approximate the width of the chromium - depleted zone by a simple diffusion analysis:

$$\ell = 2\sqrt{Dt}$$

where ℓ = width of depleted zone
D = diffusivity of Cr in
t = time (sec)

The extent of the region where the Cr content is less than 12 wt.% (required for passive film formation) can be determined by the following equation (65):

$$m = 2\sqrt{Dt}\,\frac{0.13 - X^{i}_{Cr}}{X^{o}_{Cr} - X^{i}_{Cr}}$$

where X^{i}_{Cr} = Cr content at carbide/γ interface
X^{o}_{Cr} = bulk Cr content
(mole fraction)

Using reported diffusion data from Stawström and Hillert, the widths of the depleted zones have been calculated for temperatures of 600°C and 675°C, and these results are presented in Table V with the experimental data of Section 4.2.1.

TABLE V.

A Comparison of the Theoretical and Experimental Data on the Extent of the Chromium Depleted Zone

	t (hr)	$L=2\sqrt{Dt}$ (Å)	L_{exp} (Å)	$m=L\dfrac{.13-X^{i}_{Cr}}{X^{o}_{Cr}-X^{i}_{Cr}}$ (Å)	m_{exp} (Å)
$T = 675^{\circ}C$ $D = 3 \times 10^{-15} cm^2/sec$ $X^{i}_{Cr} = \sim 0.09$	0.5	465	∿ 1500	160	——
	2	930	∿ 1750	330	∿ 100
	24	3220	∿ 2500	1140	∿ 500
	72	5580	∿ 2500	1970	∿ 750
	100	6570	∿ 2000	2330	∿ 750
$T = 600^{\circ}C$ $D = 3 \times 10^{-16} cm^2/sec$ $X^{i}_{Cr} = \sim 0.08$	2	294	∿ 800	120	——
	24	1018	∿ 800	410	∿ 100
	72	1760	∿ 1500	720	∿ 400

TABLE VI.

Experimental Diffusion Parameters for Chromium in Austenite

$$D_{exp} = D_o \exp\left(-\frac{Q}{RT}\right)$$

$$D_o = 0.08\ cm^2/sec$$

$$Q_{theor.} = -58.5\ kcal/mole$$

	t (hrs.)	D_{exp} (cm^2/sec)	Q_{exp} (kcal/mole)	% difference
$T = 675^{\circ}C$	0.5	3×10^{-14}	-54.00	7.7%
	2	1.06×10^{-14}	-55.90	4.4%
	24	1.96×10^{-15}	-59.13	1.0%
	72	4.67×10^{-16}	-61.83	5.6%
$T = 600^{\circ}C$	2	2.2×10^{-15}	-54.23	7.3%
	24	1.6×10^{-16}	-58.77	0.4%
	72	9.6×10^{-17}	-59.68	2.0%

The apparent diffusivities of Cr in γ, as estimated from results of quantitative microanalysis, are in fair agreement with previously published diffusivities (65). Experimental activation energies (Q) for diffusion of Cr in γ have been calculated for each experimental D^{γ}_{Cr} and are presented in Table VI. All values of Q were within 10% of the published value of Stawström and Hillert, with the best agreement involving those values obtained from the 24 hr sensitisation treatments.

As the temperature of sensitisation decreases, the diffusivity of Cr in γ, and therefore the width of the depleted zone, is reduced. The extent of the zone increases with time, but not as dramatically as predicted by $\sqrt{Dt}$ calculations. This implies that the rate controlling process in governing the supply of solute to the carbides is grain boundary diffusion.

4.2.3 Asymmetry

Certain solute profiles across sensitised grain boundaries were found to be asymmetric. An example of such a profile is presented in Figure 4.9. This asymmetry was pronounced within ∿ 1000Å of the grain boundary, with a wider Cr-depleted zone (shallower profile) observed on the incoherent side of the carbide. To detect this asymmetry, it was necessary to examine the grain boundary regions between precipitates which were semi-coherent with the same austenite grain. Such a microstructue is illustrated in Figure 4.9 .

Figure 4.9 Asymmetric Solute Profile Developed During Sensitisation at 675 °C, and a Representative Grain Boundary at Which Such a Profile Occurred.

72 hours at 675°C

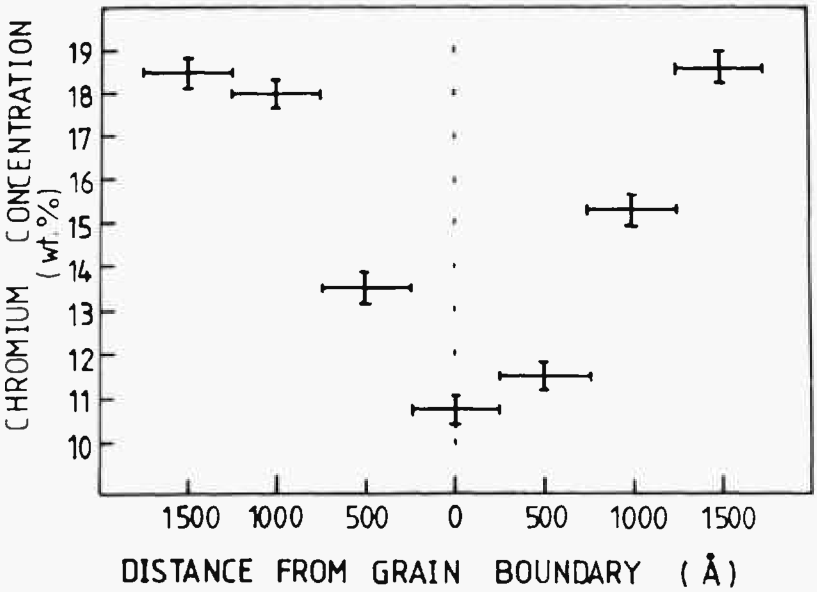

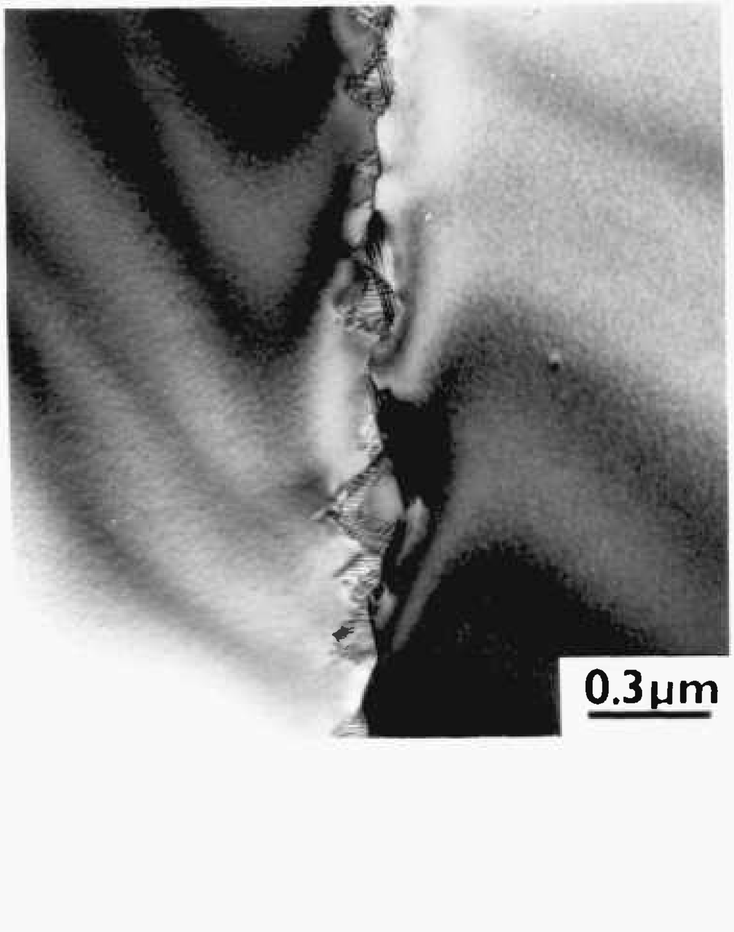

It is generally assumed that solute is transported to the carbide via volume diffusion to the grain boundary, and grain boundary diffusion to the growing carbide. The experimentally determined solute profiles indicate that this does occur in the grain on the incoherent side of the carbide, but that volume diffusion is not the controlling process in the grain which is semi-coherent with the precipitate. It is likely that growth of the semi-coherent side of the carbide may be interface-controlled, and that a ledge mechanism may be operating (189).

The observation of grain boundary migration during the sensitisation of austenitic stainless steels has been made by numerious workers (186, 190, 191). It has been proposed that carbide precipitation during sensitisation is an example of discontinuous precipitation (the simulataneous precipitation of a new phase and the migration of the matrix grain boundary). Younger et al. (12) reported that $M_{23}C_6$ precipitates grew only into the grain with which they had no unique orientation relationship. This is consistent with a discontinuous mode of precipitation: precipitation occurs behind an advancing incoherent (high energy) interface. Examples of grain boundary migration associated with discontinuous precipitation are presented in Figure 4.10. The direction of migration is dependent upon the orientation of the carbides and the austenite. There are two opposing directions of GB migration operating in Figure 4.10A. The boundary is drawn towards the grain which is incoherent

Figure 4.10 Examples of Grain Boundary Migration Which Has Occurred During Sensitisation at 675 °C.

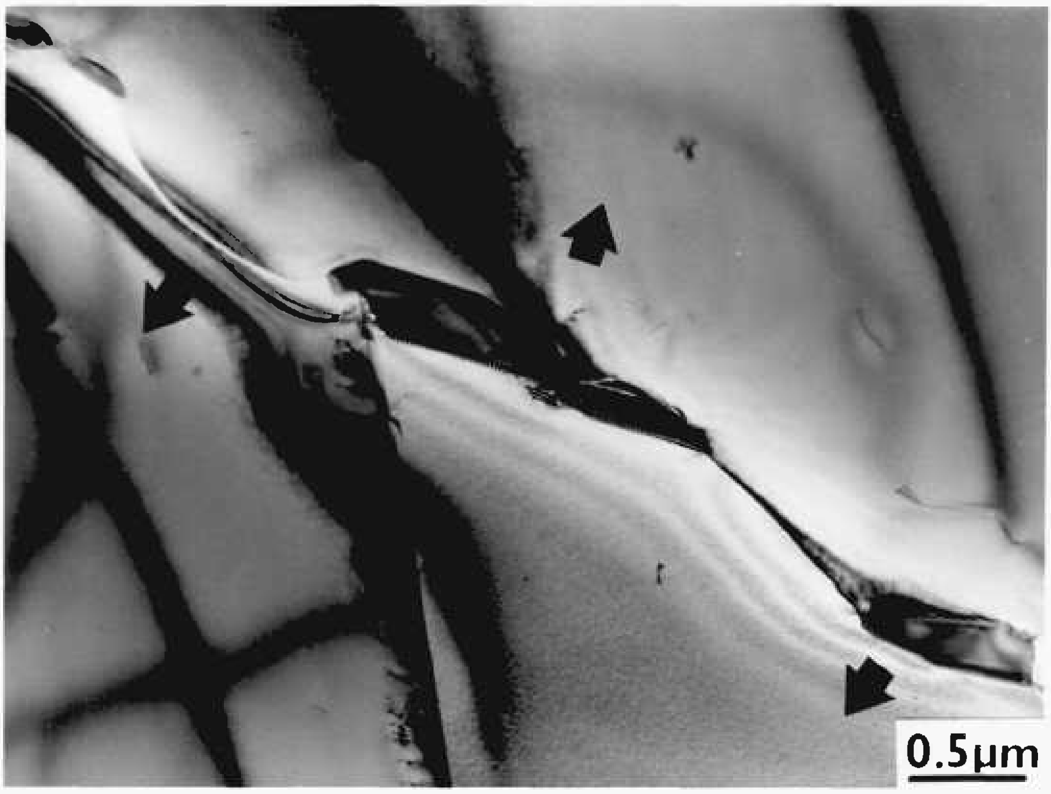
0.5μm


0.2μm

with the carbide, in agreement with the observations of Younger et al.(12). Carbides which possess the same relationship with the austenite may promote a bowing of the grain boundary between the carbides. This can be seen on the left in Micrograph A, and in Micrograph B. Whether the asymmetric nature of the solute profile is result or cause of grain boundary migration is not yet known. It is possible that there is a chemical driving force for migration of the grain boundary (191,192), particularly when an asymmetric concentration profile exists. Hillert and Lagneborg (191) also considered the role of surface energy in GB migration, especially when the grain boundary precipitate has an orientation relationship with one of the grains as the surface energies may favour the growth of the related grain. From the micrographs in Figure 4.10, it appears that the bowing of the boundary is a result of the discontinuous precipitation process. The bowing may simply be caused by the growing carbides dragging the boundary. Once the asymmetric chromium profile develops, the boundary can easily bulge out (191). The diagram in Figure 4.11 illustrate the development of grain boundary migration during precipitation.

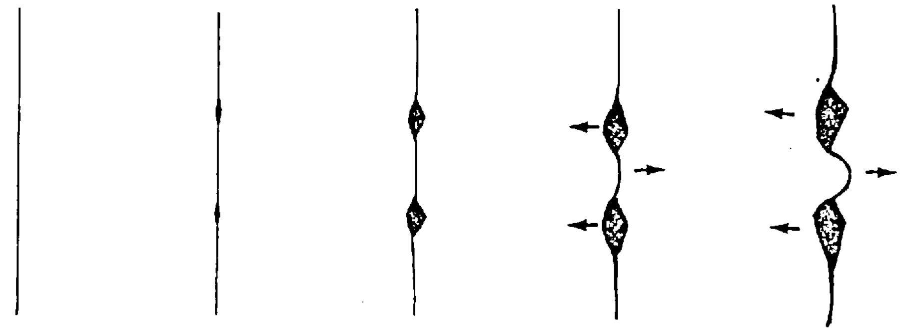

Figure 4.11 Schematic Illustration of Grain Boundary Migration and Bowing During Precipitation.

4.3 MECHANICAL PROPERTIES

Results of the conventional tension tests are presented in Table VII. The degree of carbide precipitation had no apparent effect on the mechanical properties. All failures were ductile, as illustrated in Figure 4.12. Although no variation in mechanical behaviour was observed between the heavily (72 hrs.) and lightly (2 hrs.) sensitised specimens, a minor difference was detected in the fractography of the failed specimens. The fracture surfaces of the lightly sensitised specimens were characterised by ductile dimpling, while regions of ductile intergranular tearing and ductile dimpling were observed in the heavily sensitised specimens.

4.4 PREFERENTIAL FORMATION OF MARTENSITE NEAR GRAIN BOUNDARIES

The austenitic stainless steel studied in this investigation (Type 304) is metastable with an M_s temperature of approximately -200°C. Examination of heavily sensitised specimens in the transmission electron microscope revealed the existence of martensite adjacent to certain grain boundaries. This martensite was in the form of narrow bands along various sensitised boundaries in the as-sensitised condition, and is depicted in Figure 4.13. The structure, positively identified by electron diffraction, exhibited a Nishiyama - Wasserman relationship with the austenite:

TABLE VII.

Mechanical Properties of the Sensitised Steel

heat treatment	σ_{yield} (MN/m^2)	UTS (MN/m^2)	ε_f	elongation
2 hrs. @ 675°C	181	651	0.56	75%
24 hrs. @ 675°C	180	666	0.55	73%
72 hrs. @ 675°C	185	660	0.56	75%
2 hrs. @ 600°C	210	651	0.56	75%
24 hrs. @ 600°C	192	655	0.57	75%
72 hrs. @ 600°C	191	650	0.56	75%

Figure 4.12 Representative Fractographs of Sensitised Specimens Fractured in Air (conventional tensile test).

A) Sensitised for 2 hrs. @ 675 °C

B) Sensitised for 24 hrs. @ 675 °C

C) Sensitised for 72 hrs. @ 675 °C

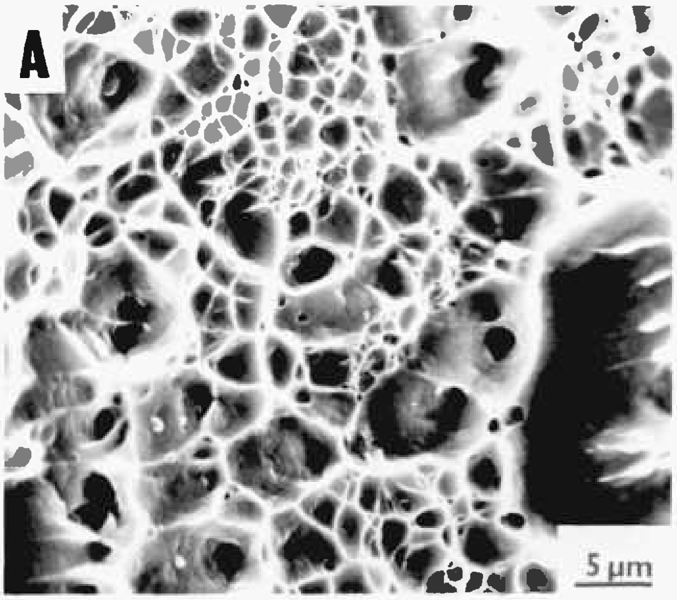
A
5 µm

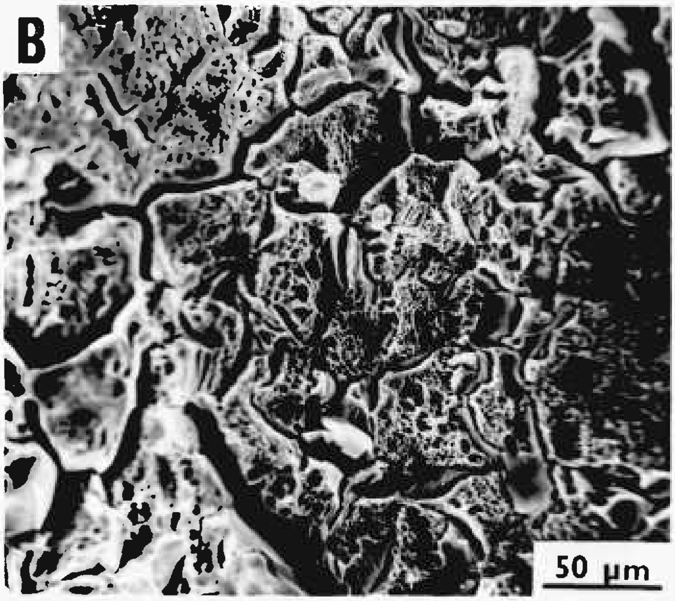
B
50 µm

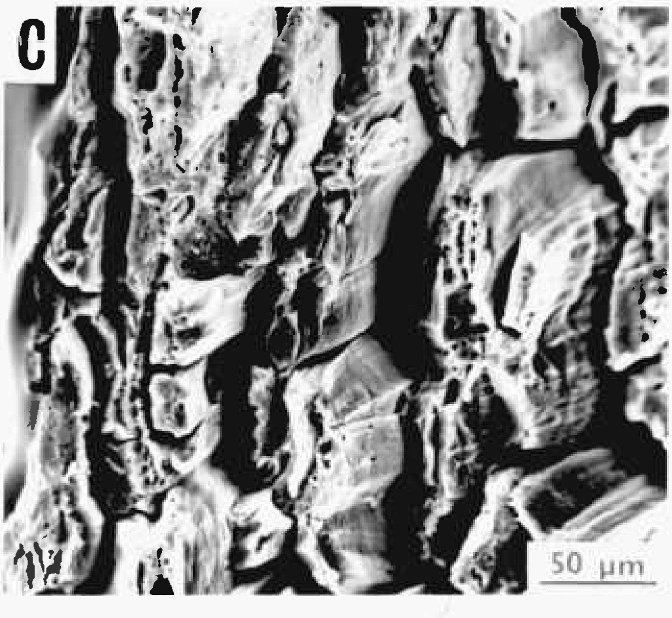
C
50 µm

$(011)_{bcc} \,||\, (111)_{fcc}$ and $[100]_{bcc} \,||\, [\bar{1}10]_{fcc}$ (Figure 4.14). This particular form of martensite - highly dislocated with no apparent midrib, and a wavy α'/γ interface - has been termed "massive" martensite, but is generally considered to be a special form of the lath variety of martensite (1,3).

Quantitative microanalysis of this grain boundary martensite revealed that a compositional gradient existed within the martensite. An example of such a profile is presented in Figure 4.15. The martensite was found to form where the Cr content was less than ∿ 16 wt.%. The depletion of chromium effectively raises the M_s in the grain boundary region so that the material can transform on cooling (193). An approximate value of the M_s can be calculated from the expression derived by Eichelman and Hull (194):

$$M_s(^{o}C) = 1302-42(\%Cr)-61(\%Ni)-33(\%Mn)-28(\%Si)-1667(\%(C+N))$$

For the material in the vicinity of the sensitised grain boundaries, this results in an M_s of ∿ $100^{o}C$ if the C depletion is neglected. Since the precipitation of $(Cr, Fe)_{23}C_6$ also results in the removal of C from the austenite, the material will be even less stable. The $\gamma \to \alpha'$ transformation would definitely be expected on the basis of the chromium concentration profiles reported in Section 4.2. Each wt.% decrease in Cr content results in an increase of approximately 30 C^{o} in the M_s temperature (1).

Figure 4.13 Preferential Formation of Martensite in the Chromium Depleted Zone of a Specimen Sensitised for 72 hrs. @ 675 °C. bright field image; HRDF image using (200) reflection; corresponding electron diffraction pattern.


1 µm

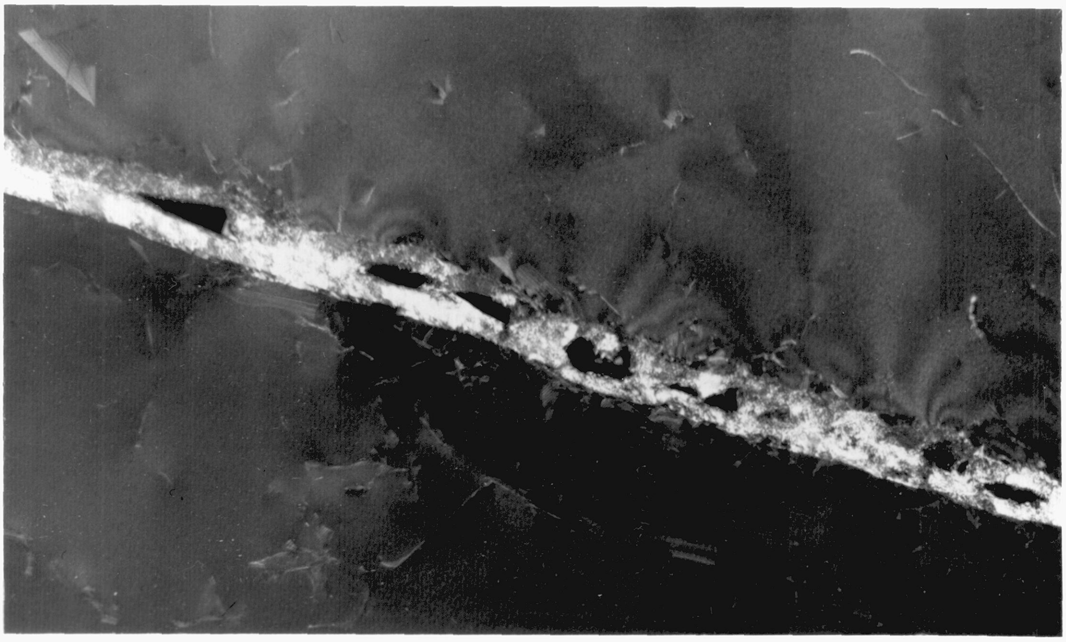

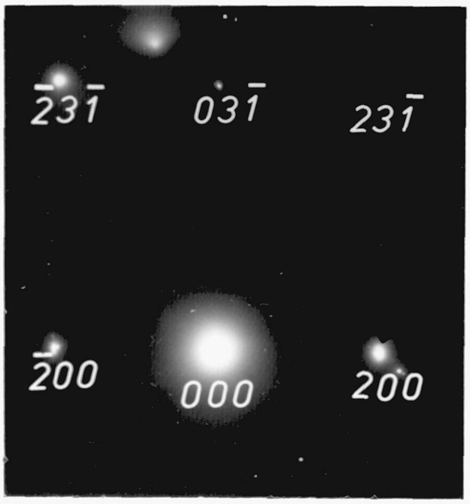
$\bar{2}3\bar{1}$
$03\bar{1}$
$23\bar{1}$
$\bar{2}00$
000
200

Figure 4.14 Region of α' Martensite in Sensitised 304 Which Exhibits a Nishiyama-Wasserman Orientation Relationship with the Austenite.

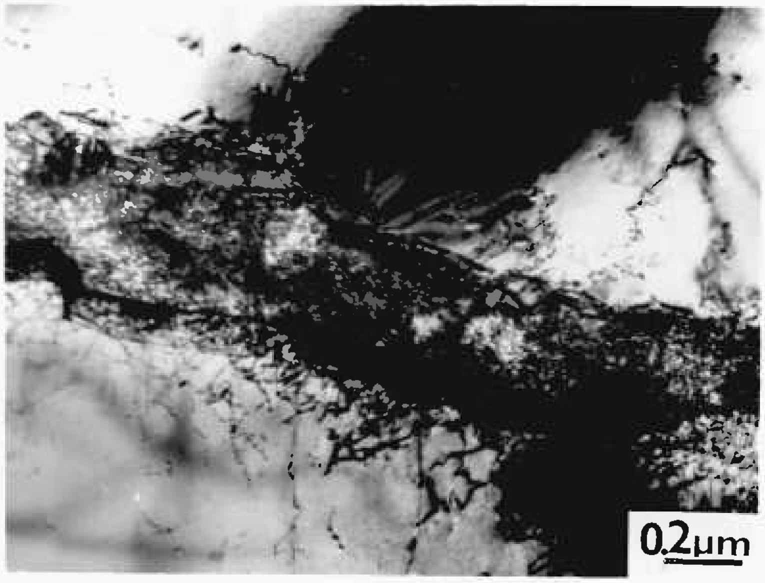

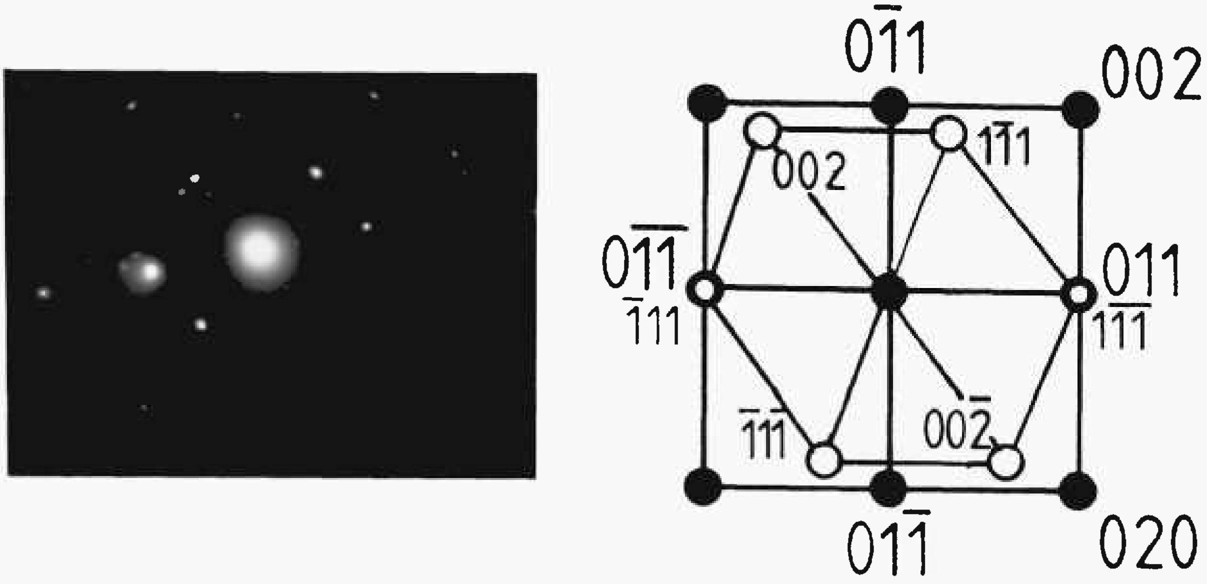

$(011)_{bcc} // (111)_{fcc}$

$[100]_{bcc} // [1\bar{1}0]_{fcc}$

Figure 4.15 Representative Micrograph and Chromium Concentration Profile of Grain Boundary Martensite

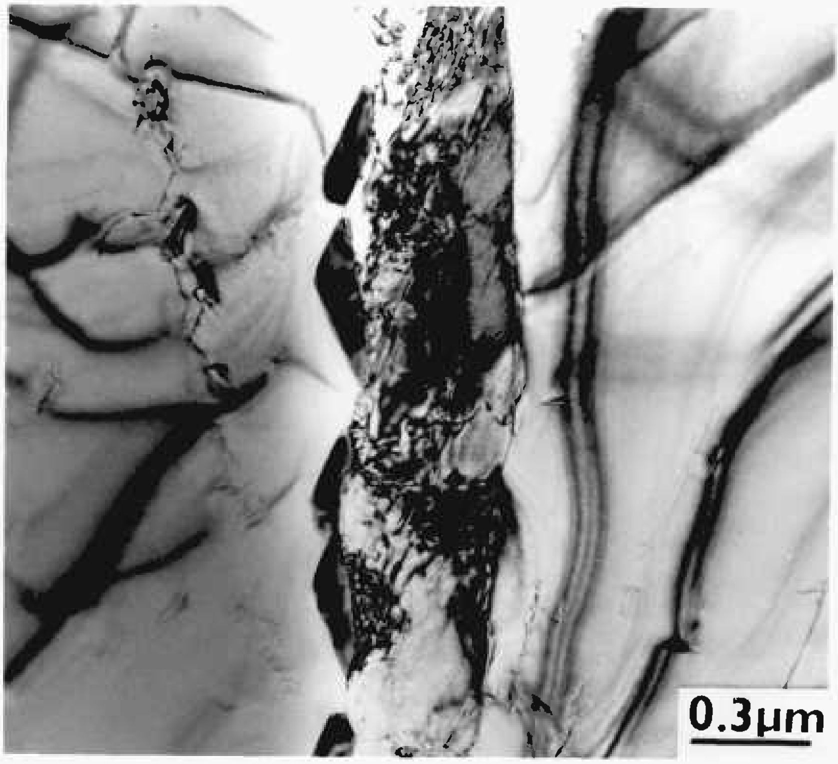
0.3μm

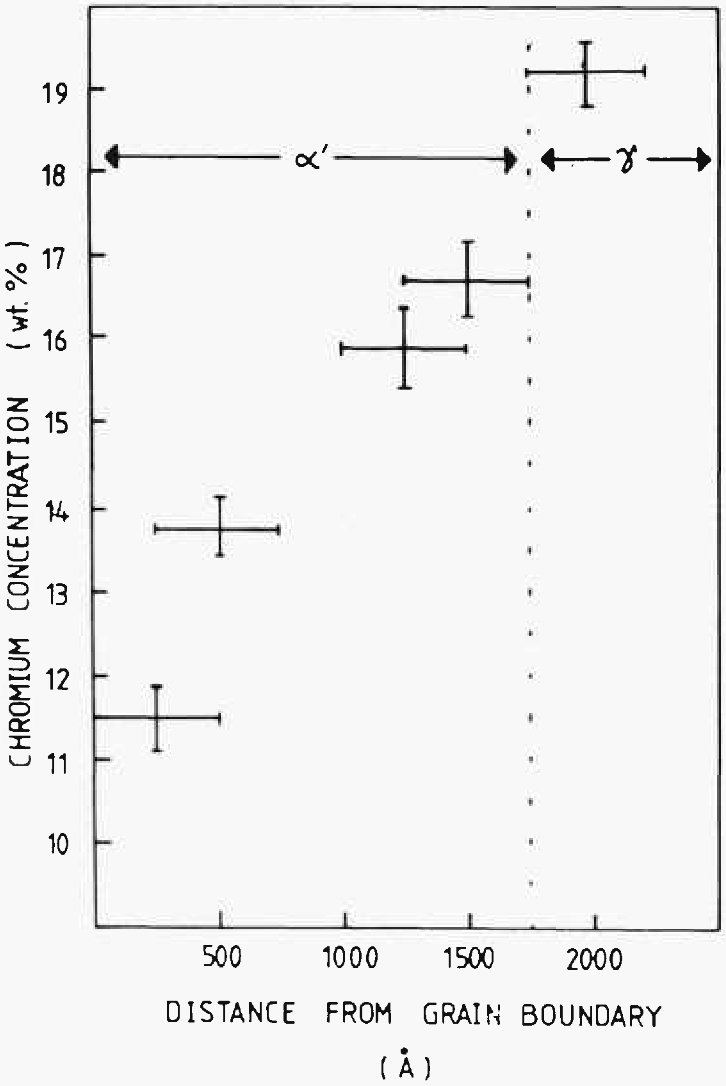
CHROMIUM CONCENTRATION (wt. %)
10
11
12
13
14
15
16
17
18
19
α'
γ
500
1000
1500
2000
DISTANCE FROM GRAIN BOUNDARY
(Å)

Martensite is stable within the composition range detected in the quantitative microanalyses of sensitised grain boundaries, but the existence of such depleted zones is not in itself sufficient to cause the spontaneous martensitic transformation. This is readily demonstrated by the observation that only a small fraction of the boundaries had transformed. Clearly, other factors are important in the transformation behaviour of this material.

Effect of Deformation

The effect of deformation on the martensitic transformation in metastable austenitic stainless steels has been well-documented (194, 195, 196). Plastic deformation enhances the $\gamma \rightarrow \alpha'$ transformation by inducing local peak stresses which can initiate the transformation, and by supplying strain-energy required to transform the fcc structure to bcc.

To determine the role of deformation in the transformation of the chromium depleted austenite to martensite, a series of specimens were strained (elastically or 5% ε) and examined for evidence of martensite. A magnetic balance was used in order to obtain a quantitative measurement of the amount of martensite present. Specimens were in the form of spark-cut discs (3.0mm in diameter). The amounts of martensite present in the strained specimens were minute. The highest reading obtained was $\sim$ 1.4 vol % for the 72 hr. @ 675°C steel strained 5%.

TEM examination revealed regions of strain induced martensite in the vicinity of various sensitised boundaries (Figure 4.16). A difference in morphology was observed between the strain-induced and as-quenched martensites. The strain-induced martensite formed in irregular packets in the grain boundary region while the as-quenched structure appeared as straight bands. Also, the "packet" martensite was not within the well-defined compositional limit ($< \sim 16$ wt.% Cr). Some martensite packets extended beyond the chromium depleted zone into the austenite.

The importance of the martensite transformation cannot be neglected. Although more martensite was observed in the specimens after deformation, the volume fraction which existed was very small. The existence of a narrow band of martensite along grain boundaries, however, may markedly affect the behaviour of the material, particularly in stress corrosive environments.

Figure 4.16 Typical Morphology of Strain-Induced Martensite Formed in the Chromium Depleted Zone of a Specimen Sensitised for 72 hrs. @ 675 °C (5 % ε).
bright field image, HRDF image using (200) reflection, corresponding electron diffraction pattern

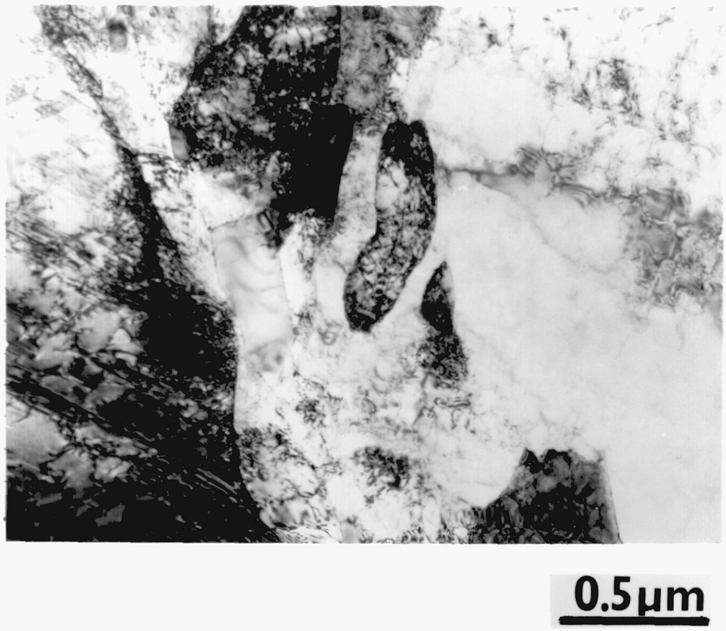
0.5µm

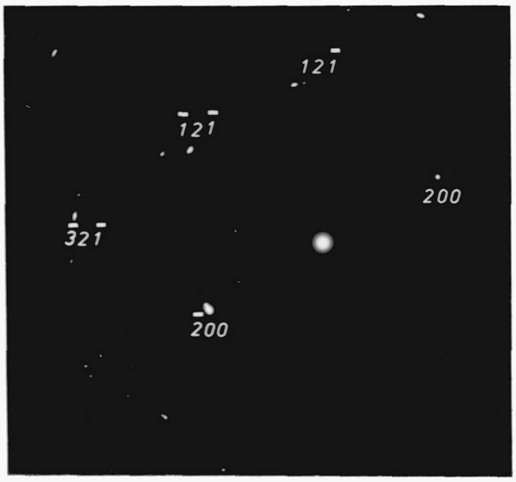
$12\bar{1}$
$\bar{1}2\bar{1}$
200
$\bar{3}2\bar{1}$
$\bar{2}00$

CHAPTER 5

INTERGRANULAR STRESS CORROSION CRACKING

5.1 POLARISATION BEHAVIOUR OF THE EXPERIMENTAL Fe-Ni-Cr ALLOYS

The effect of sensitisation on the chromium content of the austenite (or martensite) adjacent to high angle grain boundaries has been previously discussed (Section 4.2). In order to examine the behaviour of the low chromium material, a series of experimental Fe-Ni-Cr alloys (with varying chromium contents) were prepared as described in Section 2.6. The polarisation tests were conducted at a sweep rate of 100 mV/min in 0.1M H_2SO_4 + 0.02M NaCl (pH=1) and 0.01M H_2SO_4 + 0.002M NaCl (pH=2) from -600 mV SCE to + 300 mV SCE. The direction was then reversed (+ 300 mV SCE to - 600 mV SCE). In this way, it was possible to evaluate the polarisation behaviour of unfilmed and filmed metal. The results are presented in the form of polarisation curves in Figures 5.1 and 5.2.

These potentiostatically determined polarisation curves clearly demonstrate the effect of chromium content and pH on the anodic and cathodic behaviour of the Fe-Ni-Cr alloys. The corrosion potential was found to shift to more positive values as the chromium content was increased. The values of E_{corr} ranged from -440 mV (SCE) for the 10 Cr alloy to -380 mV (SCE) for the 18 Cr specimen in the

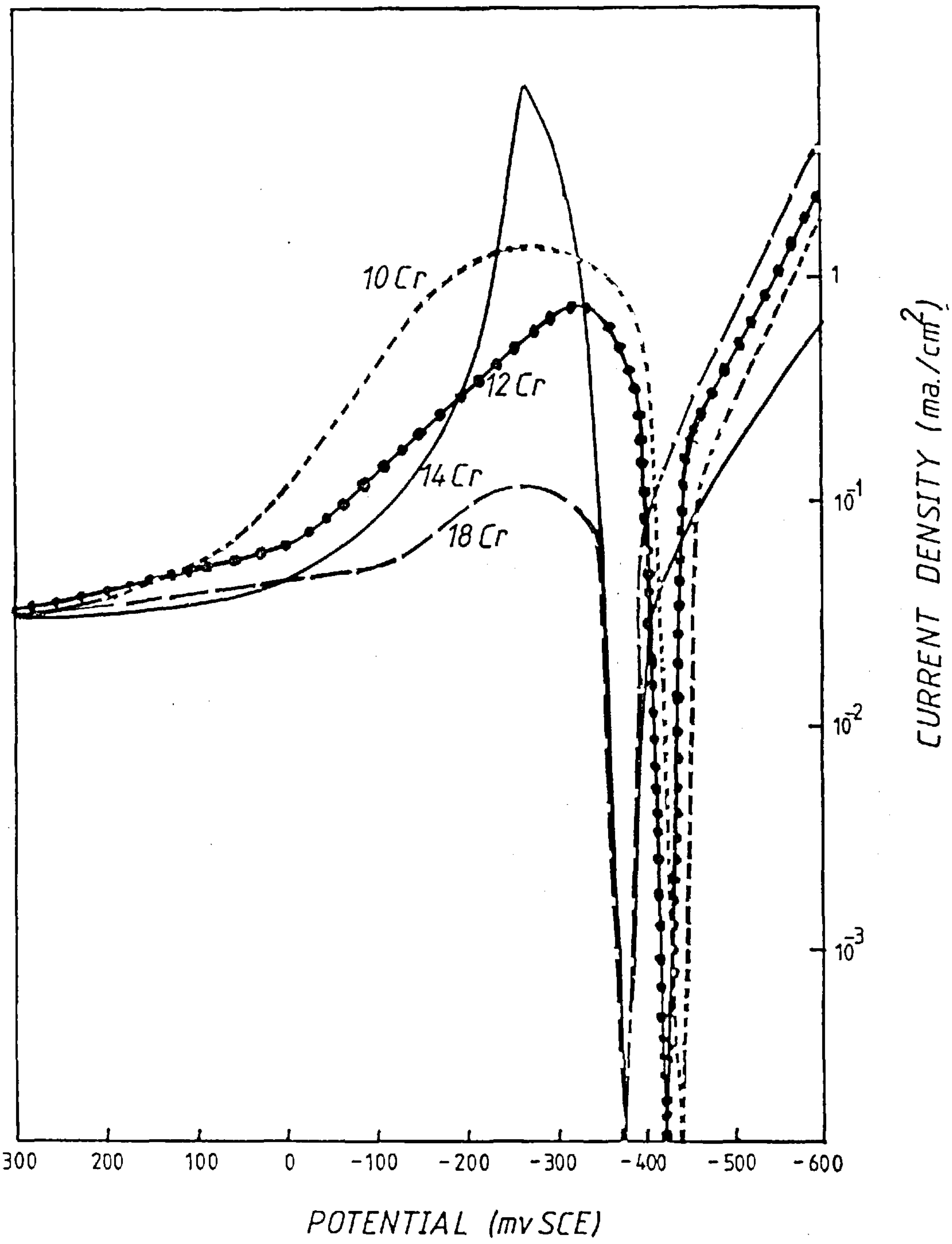

Figure 5.1 Polarisation Curves for Experimental Fe-Ni-Cr Alloys in pH=1 0.1M H_2SO_4+ 0.02M NaCl Solution. (sweep rate ∿ 100 mv/min; -600 to +300 mv)

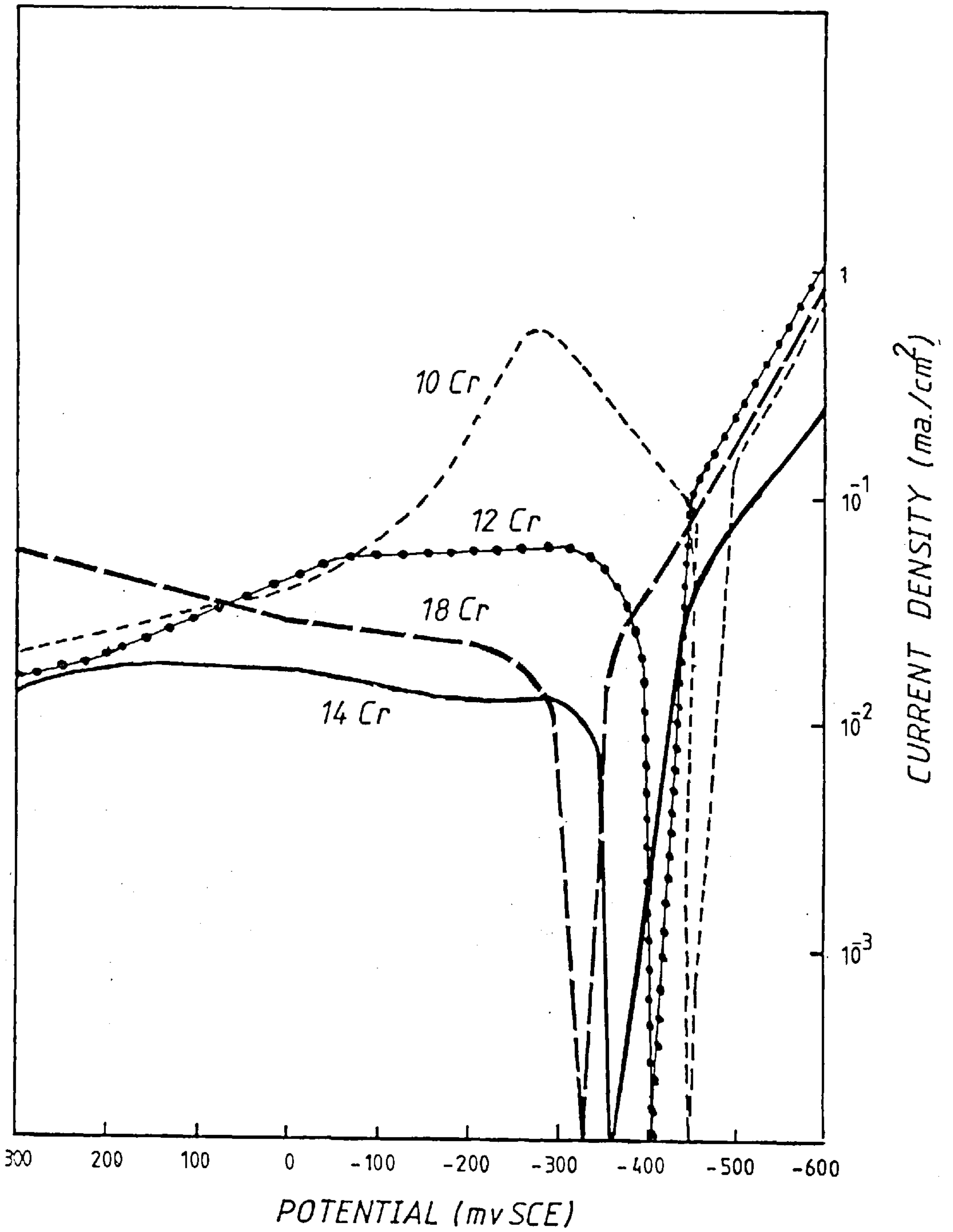

Figure 5.2 Polarisation Curves for Experimental Fe-Ni-Cr Alloys in pH=2 0.01M H_2SO_4+ 0.002M NaCl Solution. (sweep rate∿ 100 mv/min; -600 to +300mv)

0.1M H_2SO_4 + 0.02M NaCl electrolyte. The results obtained from the polarisation curves in 0.01 M H_2SO_4 + 0.002 M NaCl were consistent with the reported effect of Cr and (Cl^-) on the polarisation behaviour of the alloys (196,197). The corrosion potentials were more positive in the diluted (pH=2) electrolyte.

From these results, it was noted that two steady-state mixed potentials exist. It has been suggested (198) that E_{corr} measured in the +300mV to -600mV (SCE) scan was the result of the filmed surface coming to steady state. The value of E_{corr} obtained during the -600mV to +300mV (SCE) scan was the corrosion potential of the film free surface. These polarisation curves provided a useful guide for selection of potentials for the controlled potential SCC tests described in Section 5.3.

5.2 SCC SLOW STRAIN RATE RESULTS

The stress corrosion behaviour of the sensitised steel was evaluated through slow strain rate tests. In this type of experiment, the effect of the environment on the mechanical properties may be readily monitored. The ductility parameter selected for comparison in this study was the true strain to fracture.

The results of the stress corrosion tests are presented in Figures 5.3 and 5.4. These results will be discussed with respect to three major variables:

1) the concentration of the solution (pH);

2) period of sensitisation; and 3) temperature of sensitisation.

TABLE VIII.

Results of the Slow Strain Rate SCC Tests

Specimen	*pH*	*Elongation*	*Fracture Stress* (MN/m^2)	ε_f
2 hr/675°C	1	30%	463	0.26
	2	55%	561	0.44
24hr/675°C	1	20%	460	0.18
	2	62%	628	0.49
72hr/675°C	1	20%	456	0.18
	2	35%	497	0.30
	3	30%	561	0.27
	4	55%	613	0.44
	5	70%	640	0.53
2 hr/600°C	1	65%	626	0.50
24hr/600°C	1	22%	435	0.20
	2	14%	445	0.13
	3	16%	445	0.15
72hr/600°C	1	18%	409	0.16
	2	25%	458	0.22
	3	20%	509	0.18
	4	55%	652	0.44

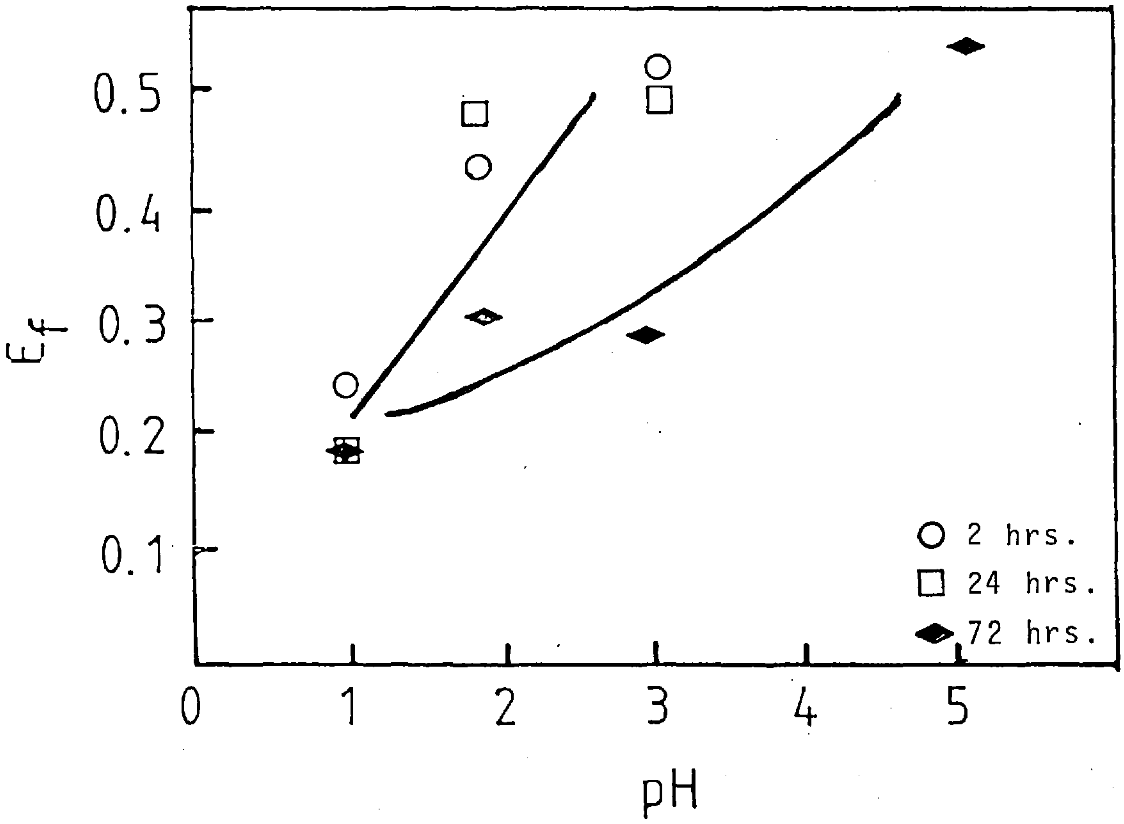

Figure 5.3 True Strain to Failure (ε_f) vs. pH of Solution For Specimens Sensitised at 675°C

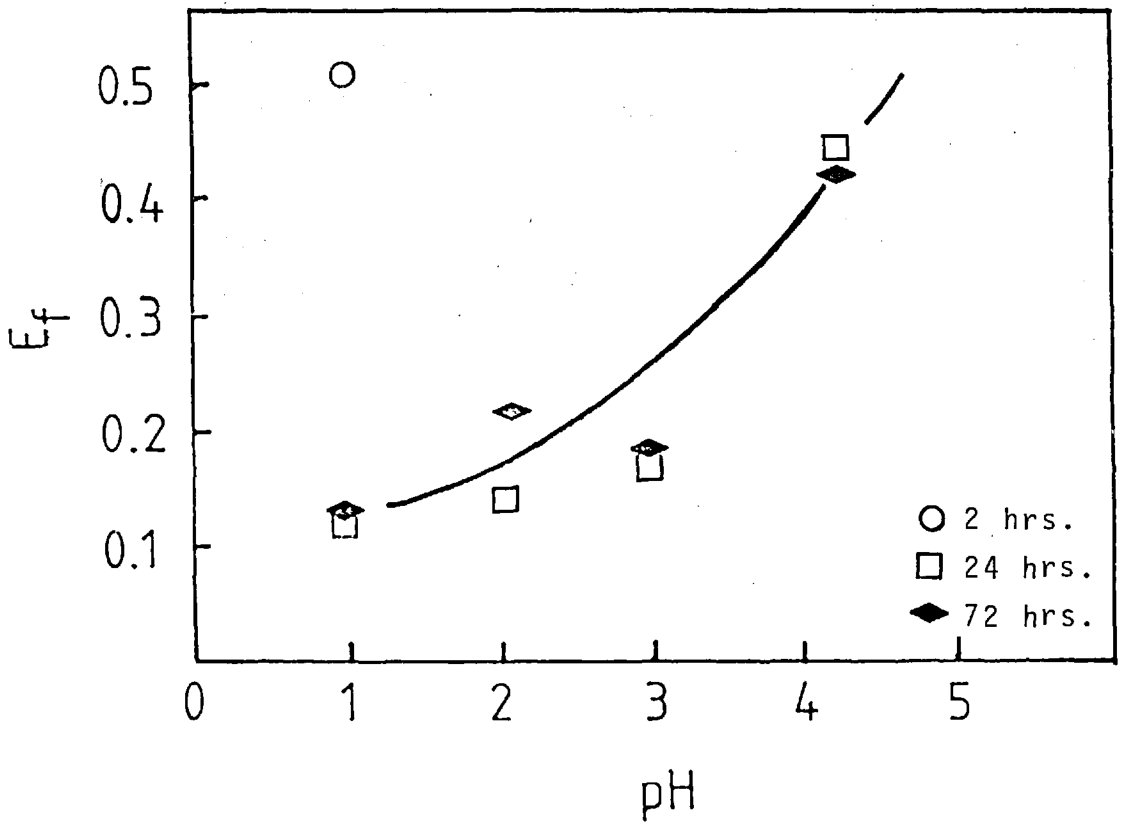

Figure 5.4 True Strain to Failure (ε_f) vs. pH of Solution For Specimens Sensitised at 600°C

5.2.1 Concentration of Solution

The effect of pH (concentration of SC solution) is illustrated in Figures 5.3 and 5.4. As the pH increases, the strain to failure increases, and approaches the value for specimens tested in an inert environment. The 72 hour specimens exhibited the greatest susceptibility to SCC with respect to pH. Figure 5.5 illustrates the type of fractography observed after stress corrosion of a 72 hr @ 675°C specimen in a pH=1 solution. There were indications of plastic deformation (slip lines), and the fracture surface was predominantly intergranular (Micrographs A, and B). However, areas of a "feathery" type of fracture sometimes termed "quasi-cleavage" were also observed (Micrograph C). Slip line attack was not extensive, although occasional examples could be detected, particularly in regions where fracture first occurred (Micrograph D). Fractographic examination of the corresponding specimens sensitised at 600°C revealed similar features, as shown in Figure 5.6. In addition to the intergranular fracture and signs of significant plastic deformation (Micrographs A and C), regions of "quasi-cleavage" were prominent (Micrograph B). The fracture surfaces had not been severely attacked by the environment, and so the cleavage-like fracture is well-preserved. Micrograph C in Figure 5.6 depicts the initial stages of slip line attack in the "quasi-cleavage" region.

Similar fracture morphologies were observed during the examination of the specimens (72 hrs @ 675°C, 72 hrs @

Figure 5.5 Representative Fractographs of Sensitised (72 hrs. @ 675 °C) Specimens Stress Corroded in pH=1 0.1M H_2SO_4 + 0.02M NaCl Solution.

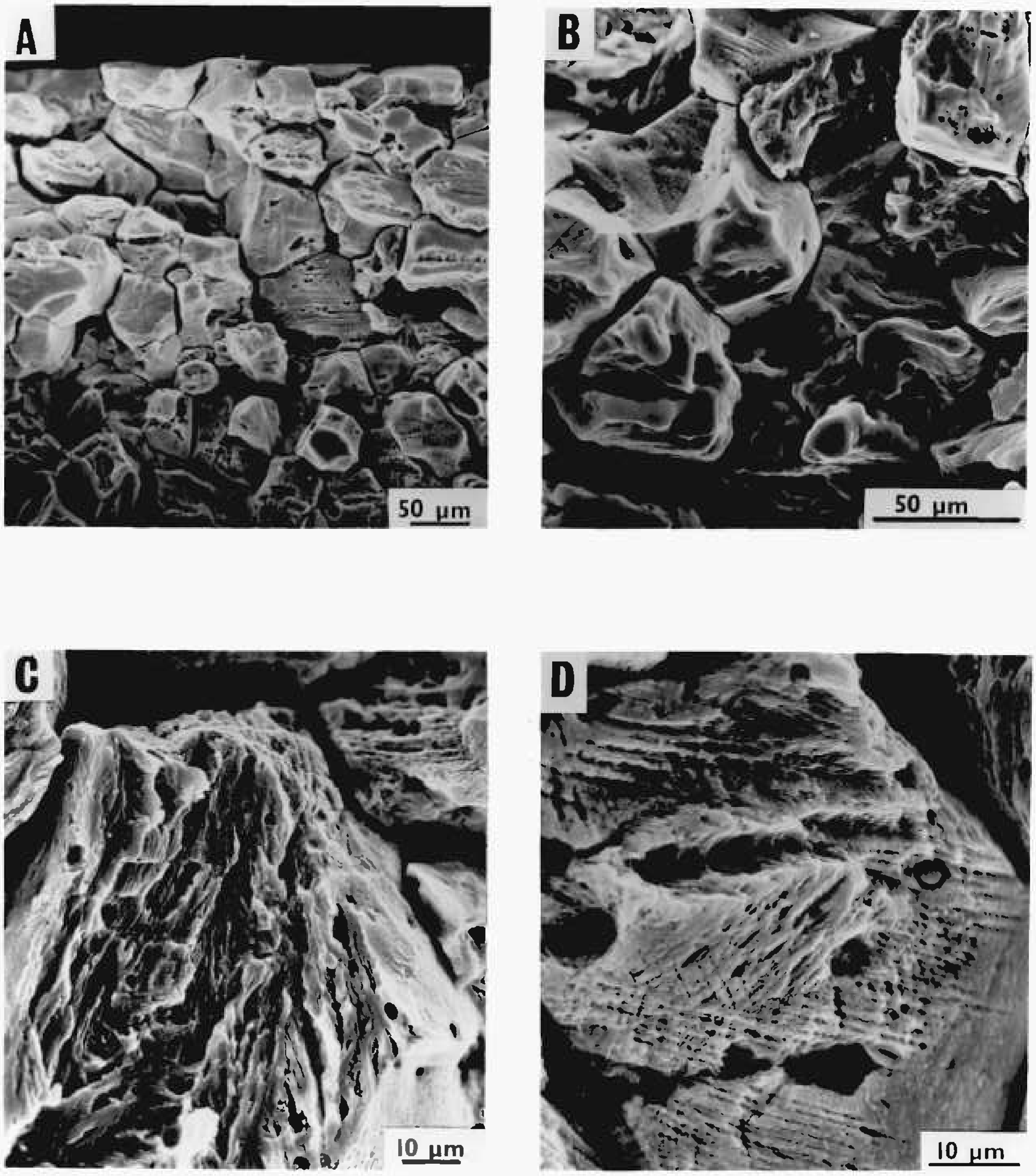
A
50 µm
B
50 µm
C
10 µm
D
10 µm

Figure 5.6 Representative Fractographs of Specimens Sensitised for 72 hrs. @ 600 °C after Stress Corrosion in pH=1 0.1M H_2SO_4 + 0.02M NaCl Solution.

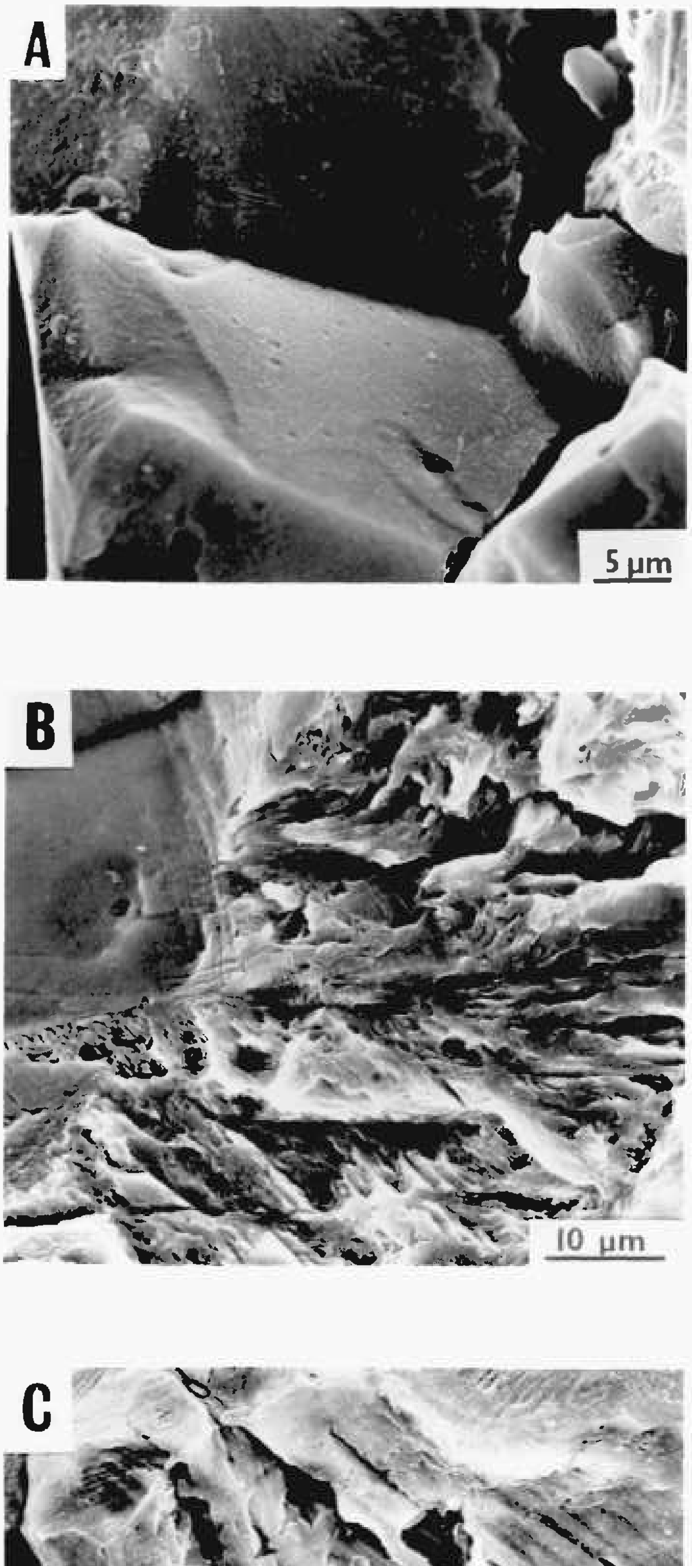
A
5 µm
B
10 µm
C
5 µm

600°C) tested in the pH=2 solutions. Representative micrographs are presented in Figure 5.7. The primary difference in fractography between specimens tested in the 0.1 M H_2SO_4 + 0.02 M NaCl and 0.01 M H_2SO_4 + 0.002 M NaCl solutions was the degree of plastic deformation, the greater strain to failure being associated with the more dilute solution. However, regions of cleavage-like fracture were still readily discernable. Micrographs A-C in Figure 5.7 depict intergranular and transgranular features. Individual carbides and the absence of slip line attack are evident from Micrograph B. The extent of general corrosive attack is illustrated in Micrograph D, which represents the surface of the stress corroded specimen. This particular specimen had been exposed to the solution for 24 hours. Etch pits can be detected, in addition to slip line attack. Another prominent feature is the preferential attack of the well-defined grain boundary regions.

Intermediate sensitisation treatments (24 hrs @ 675°C or 600°C) exhibited behaviour similar to the previously described specimens. Figure 5.8 contains representative micrographs of specimens tested in pH=1 (A and B), pH=2 (C and D) and pH=3 (E and F) solutions. These specimens were characterised by higher strain to failure values than the corresponding 72 hr. specimens. Cleavage-like regions were detected in all three environments, with the greatest amount present in the specimens tested in the 0.1 M H_2SO_4 + 0.02 M NaCl (pH=1) solution. Micrograph D illustrates the most severe pitting and slipline attack observed in the strong acid solutions. This type of attack had occurred

Figure 5.7 Typical Fracture Morphologies Observed after Stress Corrosion of Heavily Sensitised Specimens (72 hrs. @ 600 °C or 675 °C) in pH=2 0.01M H_2SO_4 + 0.002M NaCl Solution.

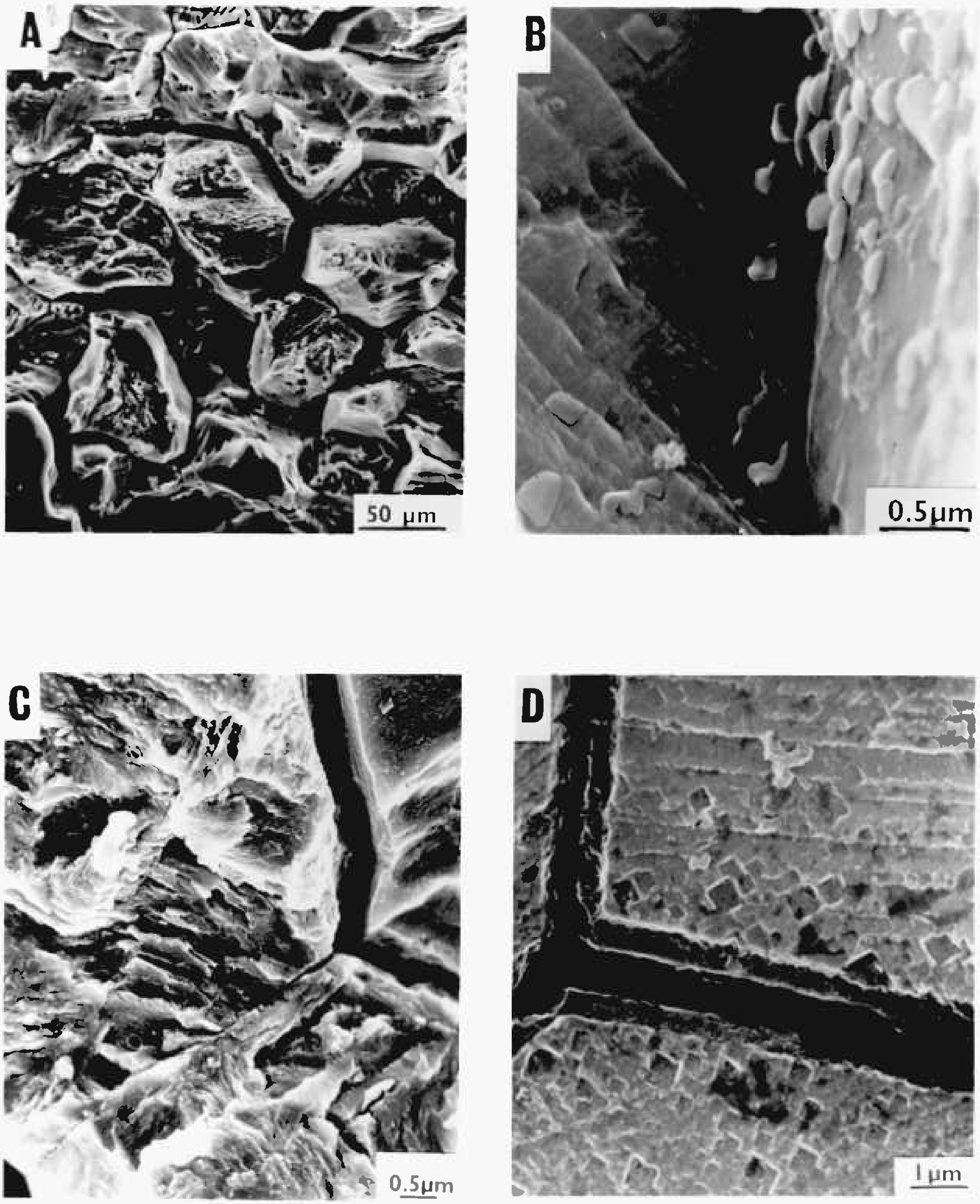
A
50 µm
B
0.5µm
C
0.5µm
D
1 µm

Figure 5.8 A Comparison of Various Fracture Morphologies Observed after Stress Corrosion of Sensitised Specimens (24 hrs. @ 600 °C and 675 °C) in H_2SO_4 + NaCl Solutions.

A,B) SCC in pH=1 0.1M H_2SO_4 + 0.02M NaCl

C,D) SCC in pH=2 0.01M H_2SO_4 + 0.002M NaCl

E,F) SCC in pH=3 0.001M H_2SO_4 + 0.0002M NaCl

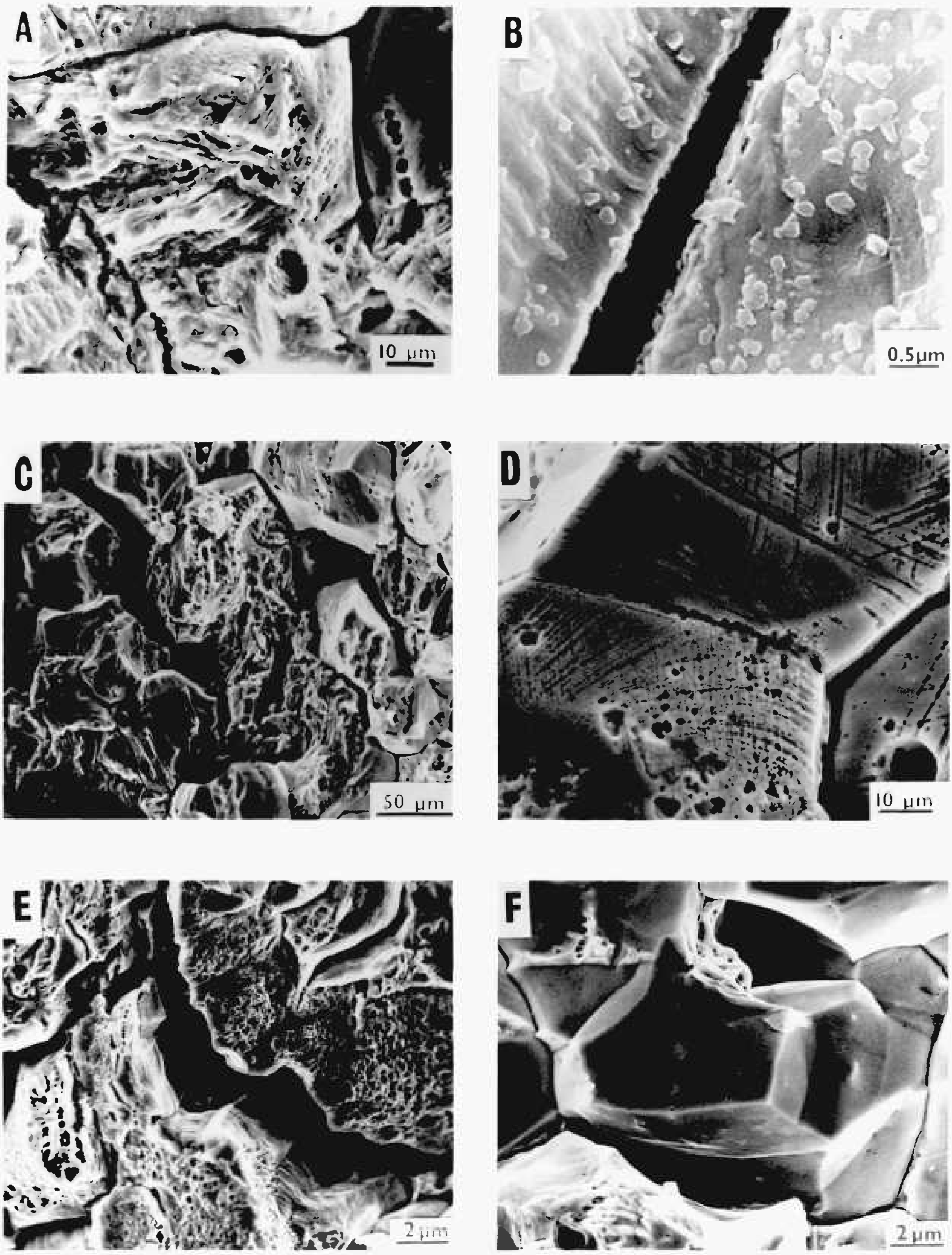
A
10 μm
B
0.5μm
C
50 μm
D
10 μm
E
2 μm
F
2 μm

in a region which had failed in the early stages of SCC propagation. Micrographs E and F represents the variety of fractography observed in the pH=3 solutions. The fracture surfaces were characterised by a region of intergranular (and cleavage-like fracture), and an area of ductile (dimpling and intergranular tearing). This type of fracture morphology is similar to that observed for the pH=2 solutions.

5.2.2 Period of Sensitisation

The observed susceptibility to IGSCC was affected by the duration of the sensitisation treatment, as illustrated in Figures 5.3 and 5.4. As the period of sensitisation increased, the material became more susceptible to stress corrosion failure. Specimens sensitised for 2 hours at 675°C only exhibited stress corrosion cracking in the strongest solution, as compared with the 72 hour specimens which failed prematurely due to SCC even in pH=3.5 solutions.

5.2.3 Temperature of Sensitisation

Similar SCC results were obtained from tests conducted on specimens sensitised at 600°C and 675°C, with other conditions being equal (duration of sensitisation, environment). This is illustrated in Figure 5.9 where E_f vs. pH is plotted for specimens sensitised at 675°C and 600°C for 72 hours. A similar trend was observed for specimens sensitised for 24 hours. The pattern was not followed by the 2 hour specimens, which were not greatly susceptible to IGSCC.

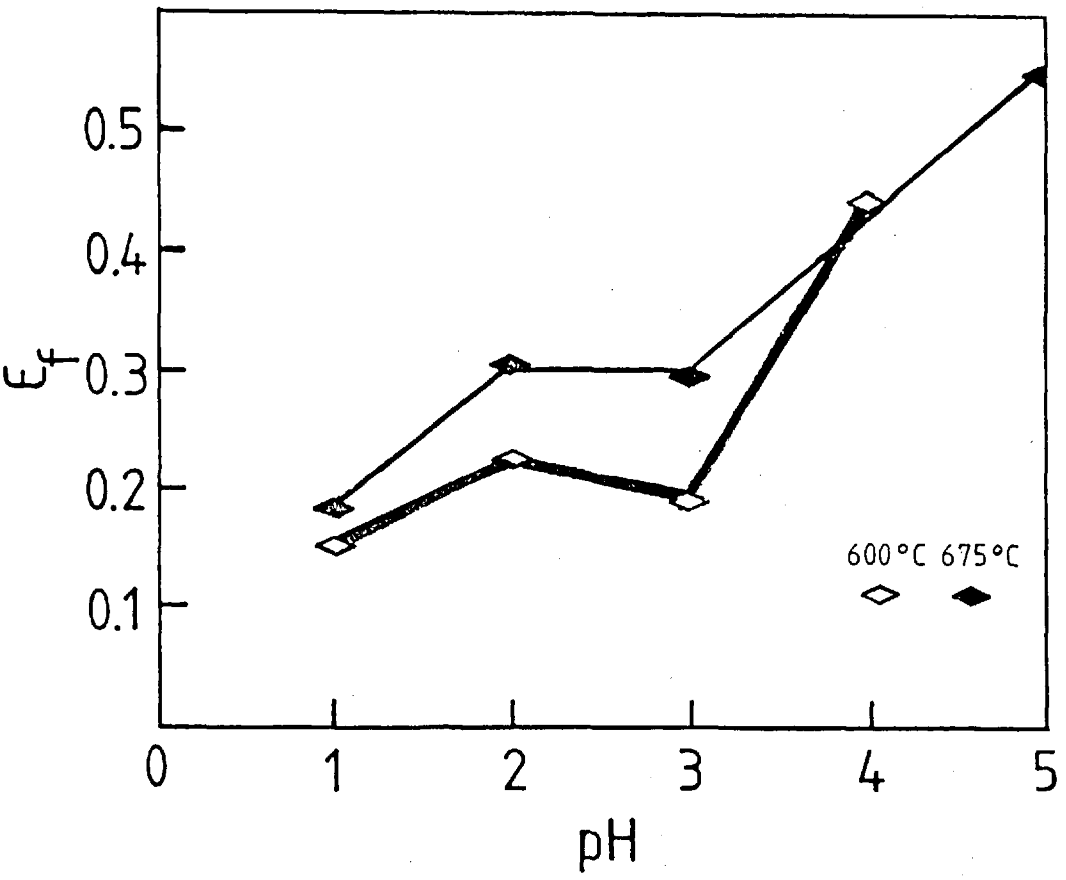

Figure 5.9 True Strain to Failure (ε_f) vs. pH of Solution For Specimens Sensitised at 675°C and 600°C For 72 Hours.

Tests conducted on material sensitised for 2 hours at 600°C failed to indicate SCC even in the most acidic environments.

5.3 STRESS CORROSION - RESULTS OF SLOW STRAIN RATE TESTS CONDUCTED UNDER CONTROLLED POTENTIAL

The effect of an applied anodic or cathodic potential on the SCC behaviour of metals has been the major factor in distinguishing between active path or hydrogen embrittlement mechanisms to describe the phenomenon of SCC. Essential to active path mechanisms is the role of dissolution in crack advance. Application of an anodic potential should promote dissolution, and therefore enhance cracking. For hydrogen embrittlement models of SCC, crack propagation should be enhanced when hydrogen entry is enhanced, i.e. under cathodic potentials. Therefore, to elucidate the primary mechanism of stress corrosion cracking (propagation), stress corrosion tests were conducted under potential control.

A series of sensitisation treatments were examined (2, 24 and 72 hours at 675°C) in two solutions (0.1 M H_2SO_4 + 0.02 M NaCl (pH=1), and 0.01 M H_2SO_4 + 0.002 M NaCl (pH=2) under anodic and cathodic potentials. The potentials selected were -140mV (SCE) and -650mV (SCE). The anodic potential of - 140 mV lies in the active peak (negative slope) of the polarisation curve, while -650mV is in the cathodic region. Both potentials are approximately 200 mV from the corrosion potential of the low chromium material at the sensitised grain boundaries.

The results of these experiments are presented in Figure 5.10. The strain to failure is plotted with respect to applied potential for each sensitisation treatment.

5.3.1 Cathodic Control

All sensitised specimens failed prematurely when tested in either solution under cathodic polarisation (- 650mV SCE). Examination of the fracture surfaces revealed regions of intergranular and cleavage-like fracture, representative fractographs of which are presented in Figures 5.11 - 5.13.

The primary fracture mode in the 72 hour specimens was intergranular, with cleavage-like regions becoming more prominant as the sensitisation time decreased. Micrograph A in Figure 5.11 is typical of the 72 hour specimens. Indications of hydrogen cracking are evident in Micrograph B, where fine transgranular cracks can be detected on a carbide-covered intergranular face. The absence of dissolution attack is demonstrated in Micrograph C which contains a high magnification micrograph of an intergranular crack. Depressions can be seen on the grain where once carbides had been present.

Specimens sensitised for 24 hours exhibited similar behaviour when tested under cathodic potential. Two fracture modes - intergranular and cleavage-like- characterised these failures. Strains to failure were slightly greater than those for the 72 hour specimens. Slip lines are visible in the intergranular region portrayed in Micrograph A in Figure 5.12. Individual carbides were still easily

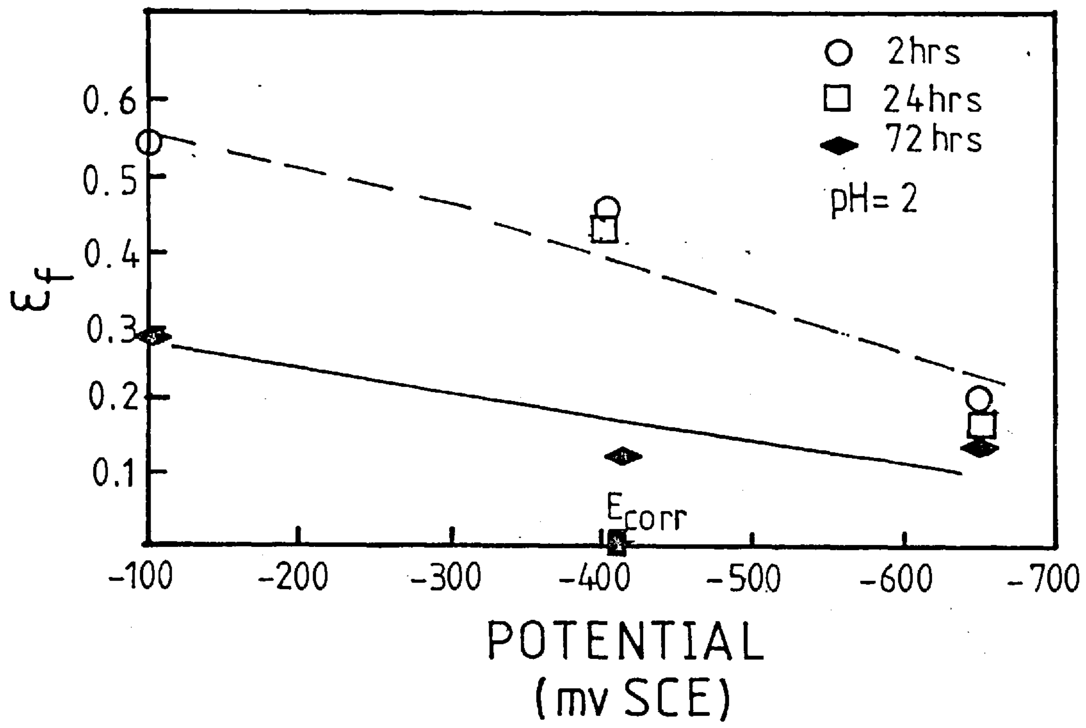

Figure 5.10 True Strain to Failure (ε_f) vs. Applied Potential For Controlled Potential SSR Tests.

Figure 5.11 Representative Fractographs of Sensitised Specimens (72 hrs. @ 675 °C) Tested in pH=2 0.01M H_2SO_4 + 0.002M NaCl Solution Under Cathodic Control (-650 mV SCE)

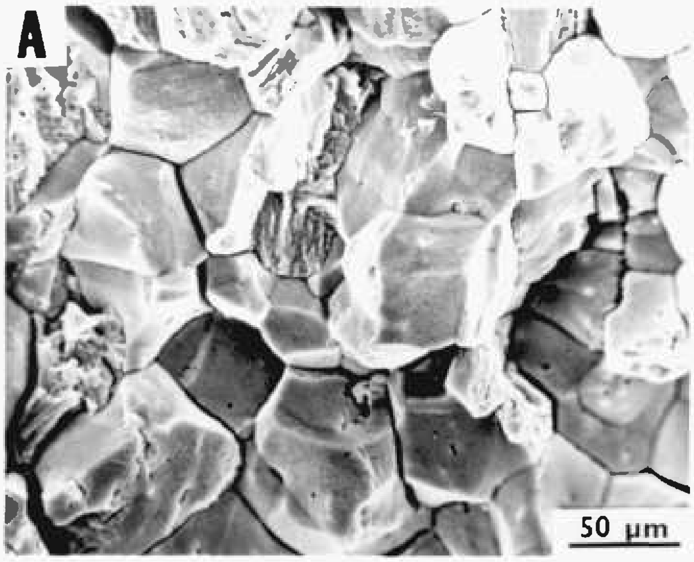
A
50 μm

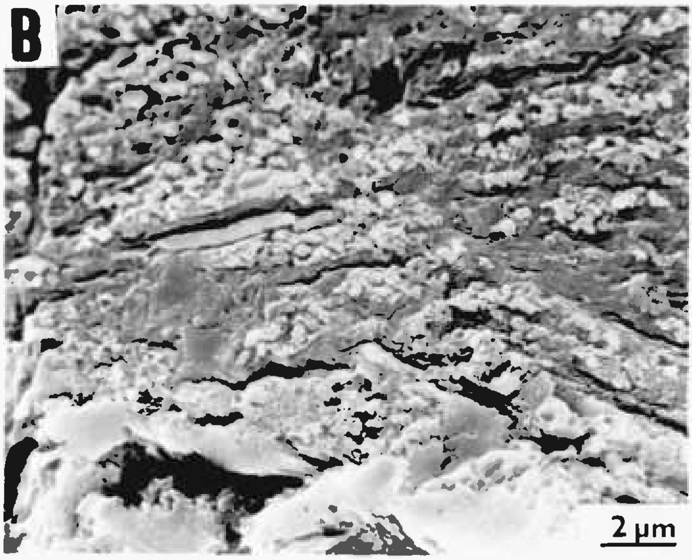
B
2 μm

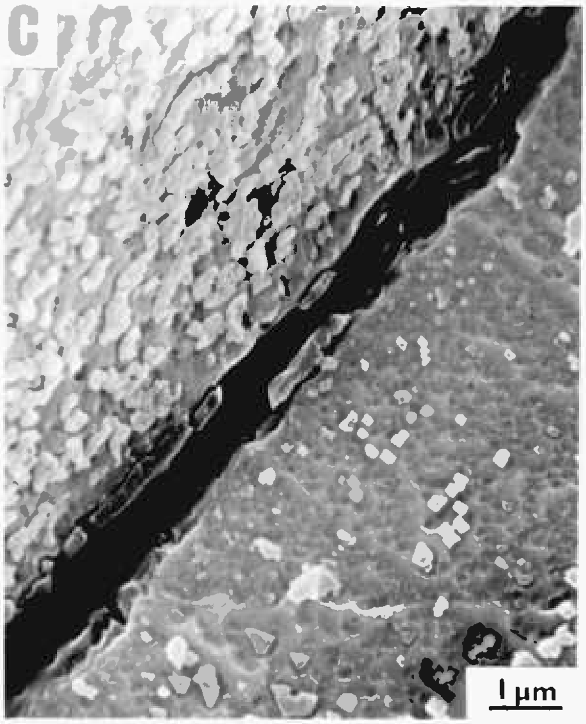
C
1 μm

Figure 5.12 Representative Fractographs of Specimens Sensitised for 24 hrs. @ 675 °C Tested Under Cathodic Control in:

A,B,D) pH=2 0.01M H_2SO_4 + 0.002M NaCl

C) pH=1 0.1M H_2SO_4 + 0.02M NaCl

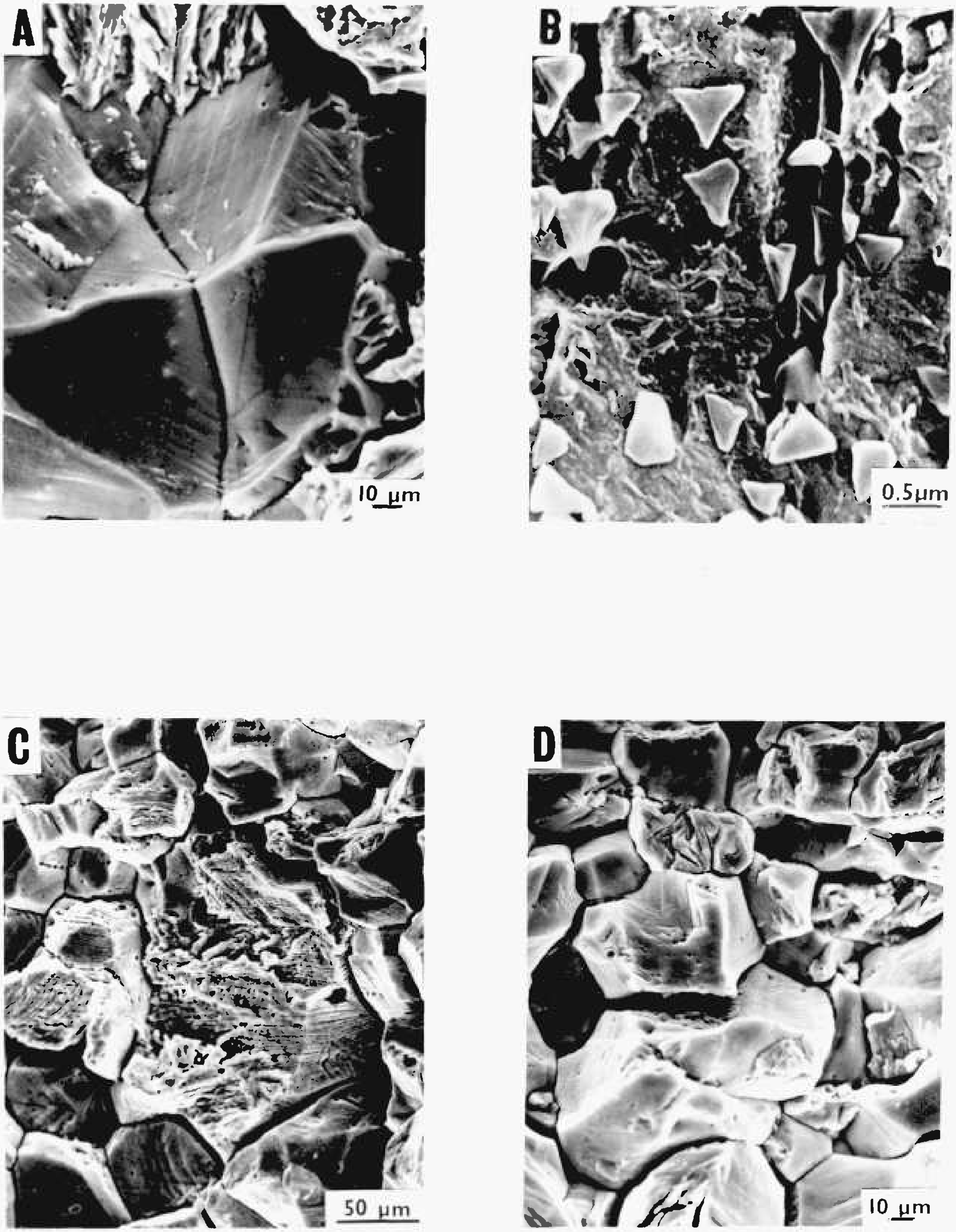
A
10 µm
B
0.5µm
C
50 µm
D
10 µm

Figure 5.13 Representative Fractographs of Specimens Sensitised for 2 hrs. @ 675 °C and Tested Under Cathodic Control (-650 mV SCE)

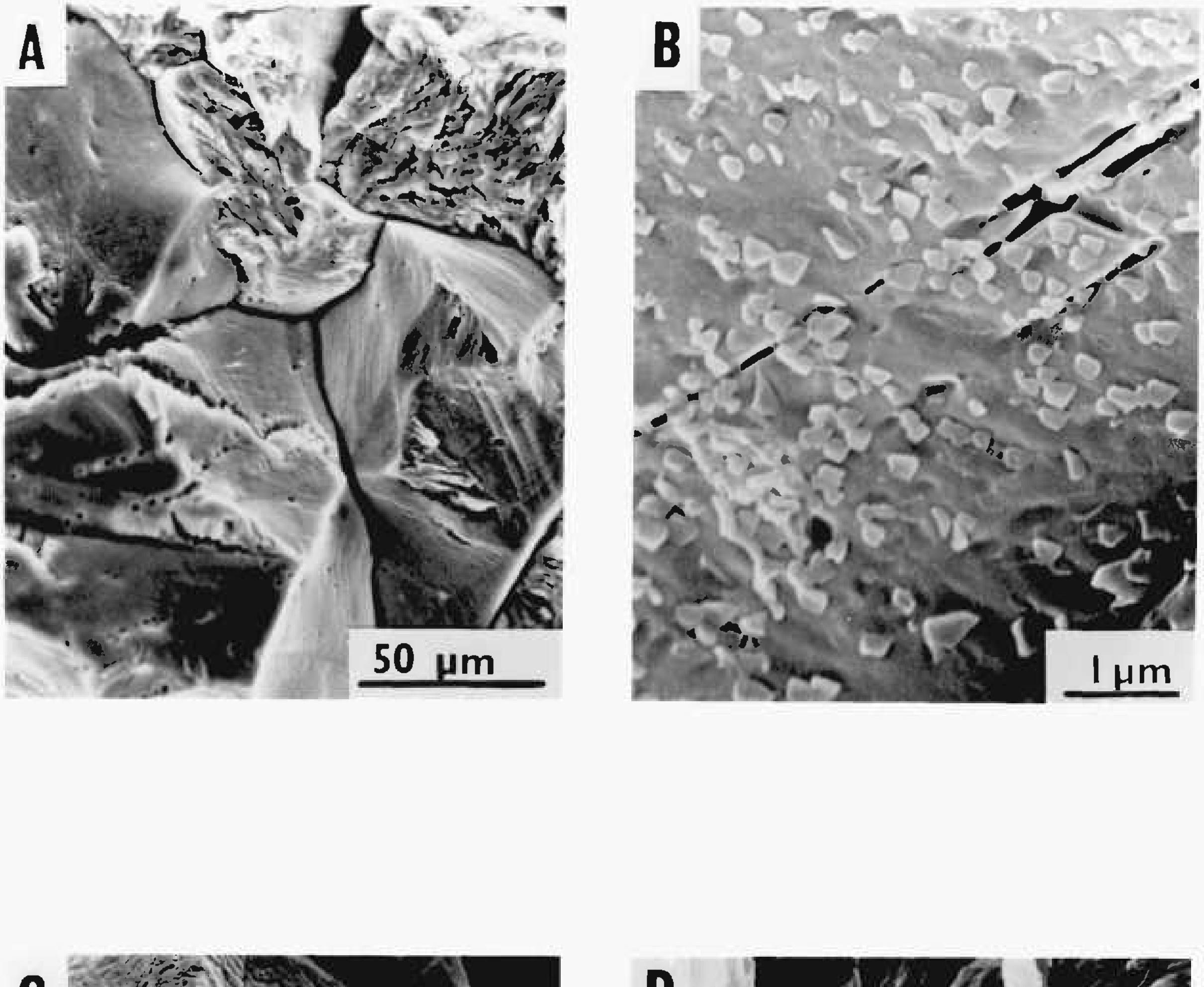
A
50 µm
B
1 µm
C
10µm
D
1 µm

resolved (Micrograph B). Representative micrographs of fracture surfaces examined after testing in the pH=1 and pH=2 solutions are presented in Micrographs C and D, respectively. Some slip line attack can be observed in Micrograph C. No difference in strain to failure was detected for these specimens.

The greatest failure strains were associated with the specimens sensitised for 2 hours. Once again, the fracture surface was characterised by regions of intergranular and cleavage-like failure, as illustrated in Figure 5.13 (Micrograph A). Secondary cracking on an intergranular face is shown in Micrograph B. The cracking is crystallographic, as would be expected for the case of hydrogen cracking. Micrographs C and D contain additional examples of transgranular fracture. It appears to be crystallographic, and fine in structure.

Fracture matching was undertaken in order to confirm that the cleavage-like fracture was not related to slip but rather due to embrittlement. Micrographs of matched fracture surfaces are presented in Figures 5.14 and 5.15. Also included in Figure 5.14 are two matching micrographs of the cleavage-like fracture; one micrograph is reverse-printed so that a detailed comparison of the features may be made. The second set of matched micrographs (Figure 5.15) depicts the effect of the acid environment on the fine cleavage-like structure. The left fracture surface was kept under cathodic control. The opposite face, however, was

Figure 5.14 Matching Fracture Surfaces From Sensitised Specimens (24 hrs. @ 675°C) Tested in pH=2 0.01M H_2SO_4 + 0.002M NaCl Solution Under Cathodic Control (-650 mV SCE).

The lower right-hand micrograph is reverse printed to enable a comparison of the features to be made.

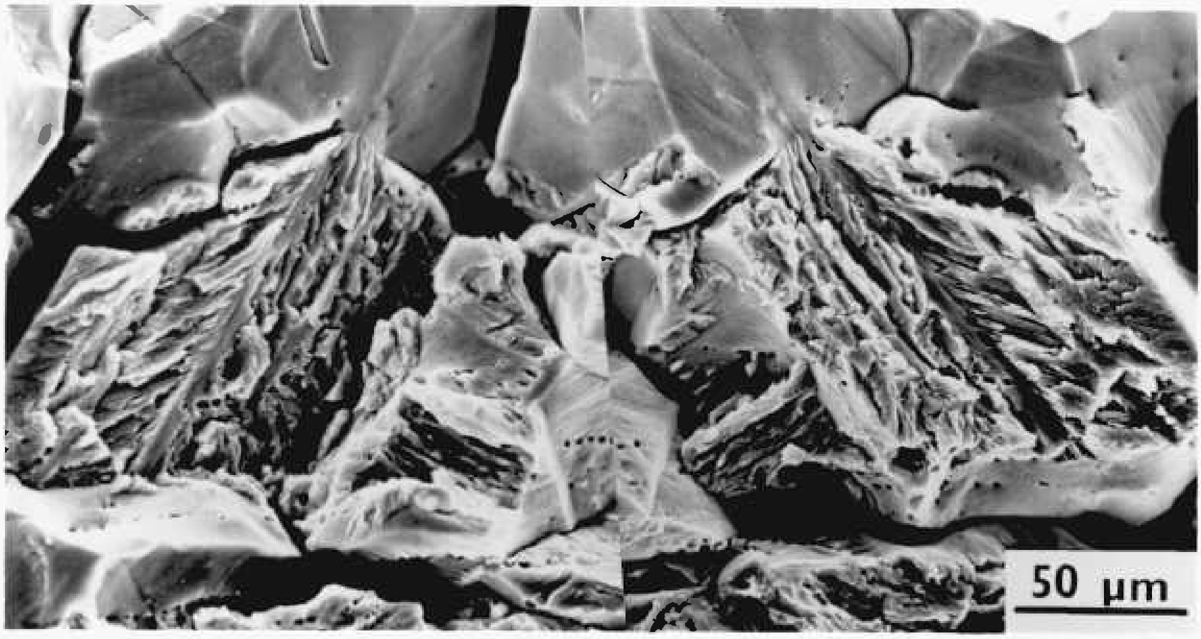
50 µm

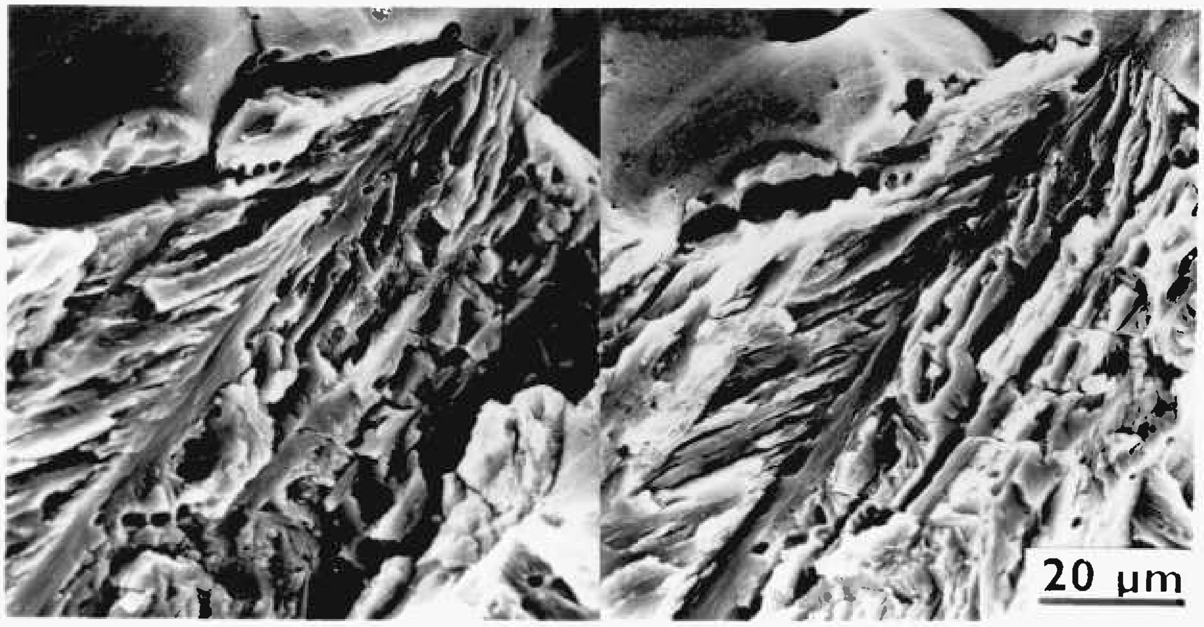
20 µm

Figure 5.15 Matching Fracture Surfaces From Sensitised Specimens (24 hrs. @ 675°C) Tested in pH=2 0.01M H_2SO_4 + 0.002M NaCl Solution Under Cathodic Control (-650 mV SCE).
The effect of post-fracture dissolution can be observed in the lower micrographs. The surface on the left was exposed to the solution while under cathodic protection, while that on the right was permitted to corrode freely.

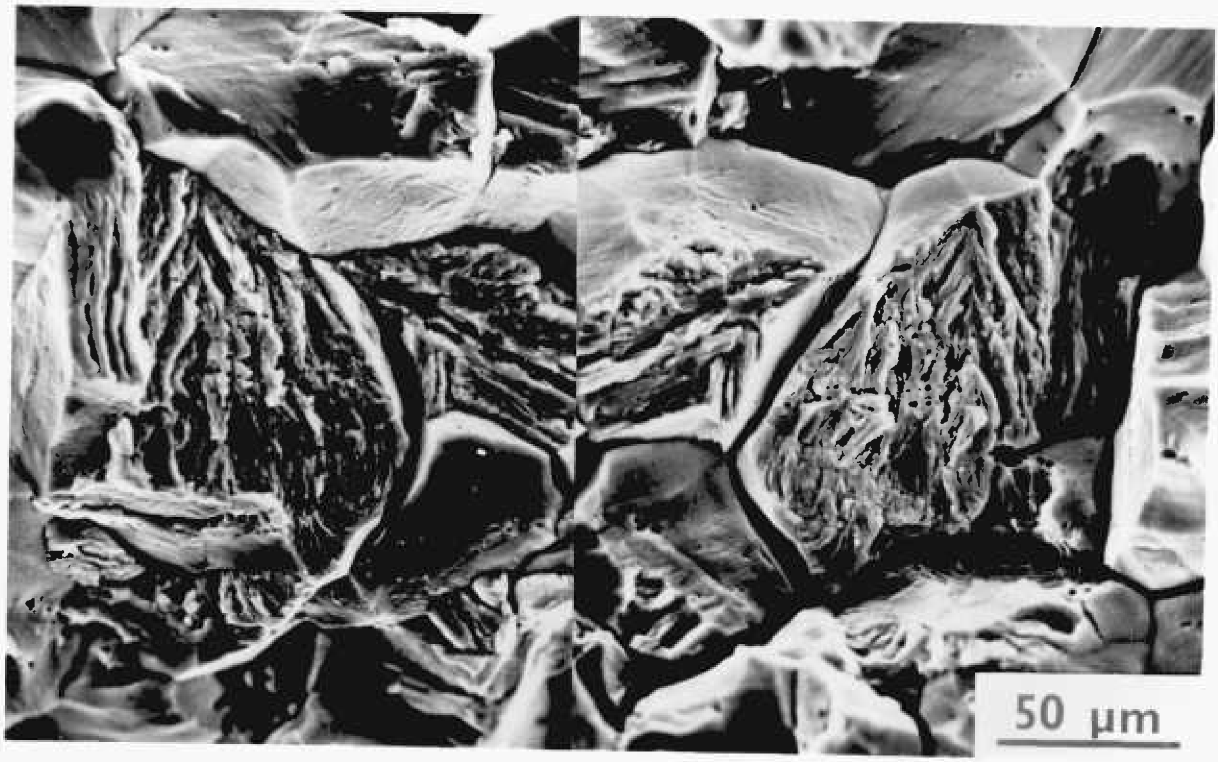
50 μm

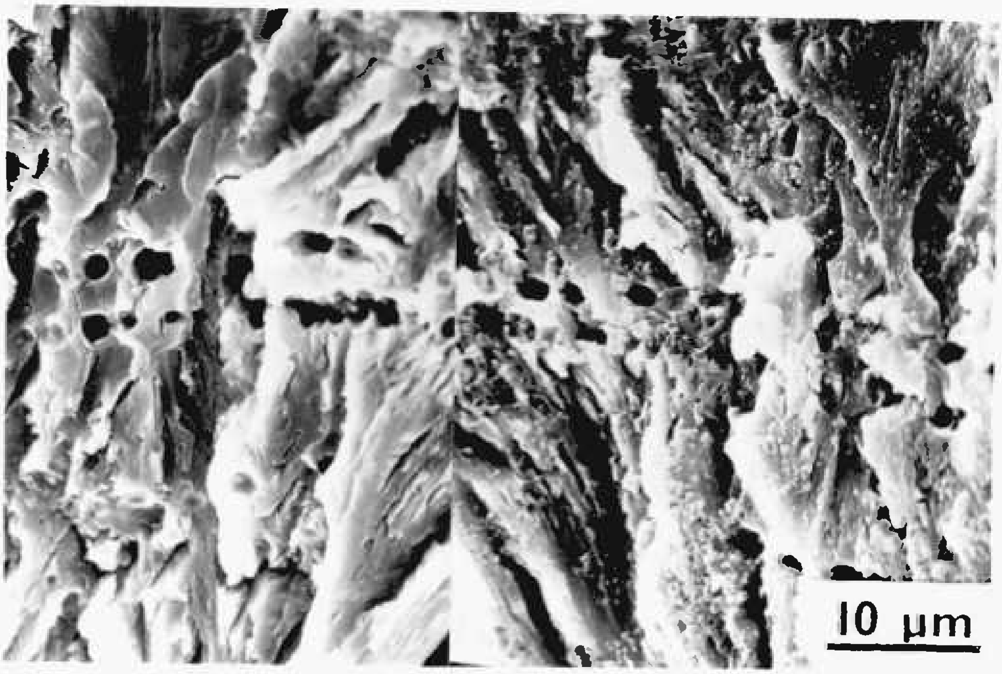
10 μm

not cathodically protected after fracture, and was permitted to corrode freely for approximately 3 hours. A small amount of attack occurred, and corrosion product can be readily detected in the right micrograph.

All slow strain rate tests conducted under cathodic potential displayed similar fracture morphologies. The strains to failure for each sensitisation treatment paralleled those results obtained under free corrosion conditions in that the 72 hour specimens fractured at the lowest strain, while the 2 hour specimens failed at the highest value ($\varepsilon_f = 0.22$).

5.3.2 Anodic Control

Unlike the SCC experiments conducted under cathodic polarisation, the results of the anodically controlled tests depended strongly on the solution. All specimens tested in the pH=1 H_2SO_4 + NaCl solution failed intergranularly, with little or no strain.

Examples of intergranular fracture presented in Figure 5.16 were typical of the heavily sensitised specimens. There was no evidence of slip-line attack (Micrograph A). The specimens underwent little plastic deformation as failure occurred shortly after yielding. Application of stress was not required for intergranular failure under these conditions (pH=1, -140mV SCE). Micrographs B-D depict the intergranular carbides and grain faces after failure.

Figure 5.16 Intergranular Failure of Heavily Sensitised Specimens (72 hrs. @ 675°C) Tested in pH=1 0.1M H_2SO_4 + 0.02M NaCl Solution Under Anodic Control (-140 mV SCE).

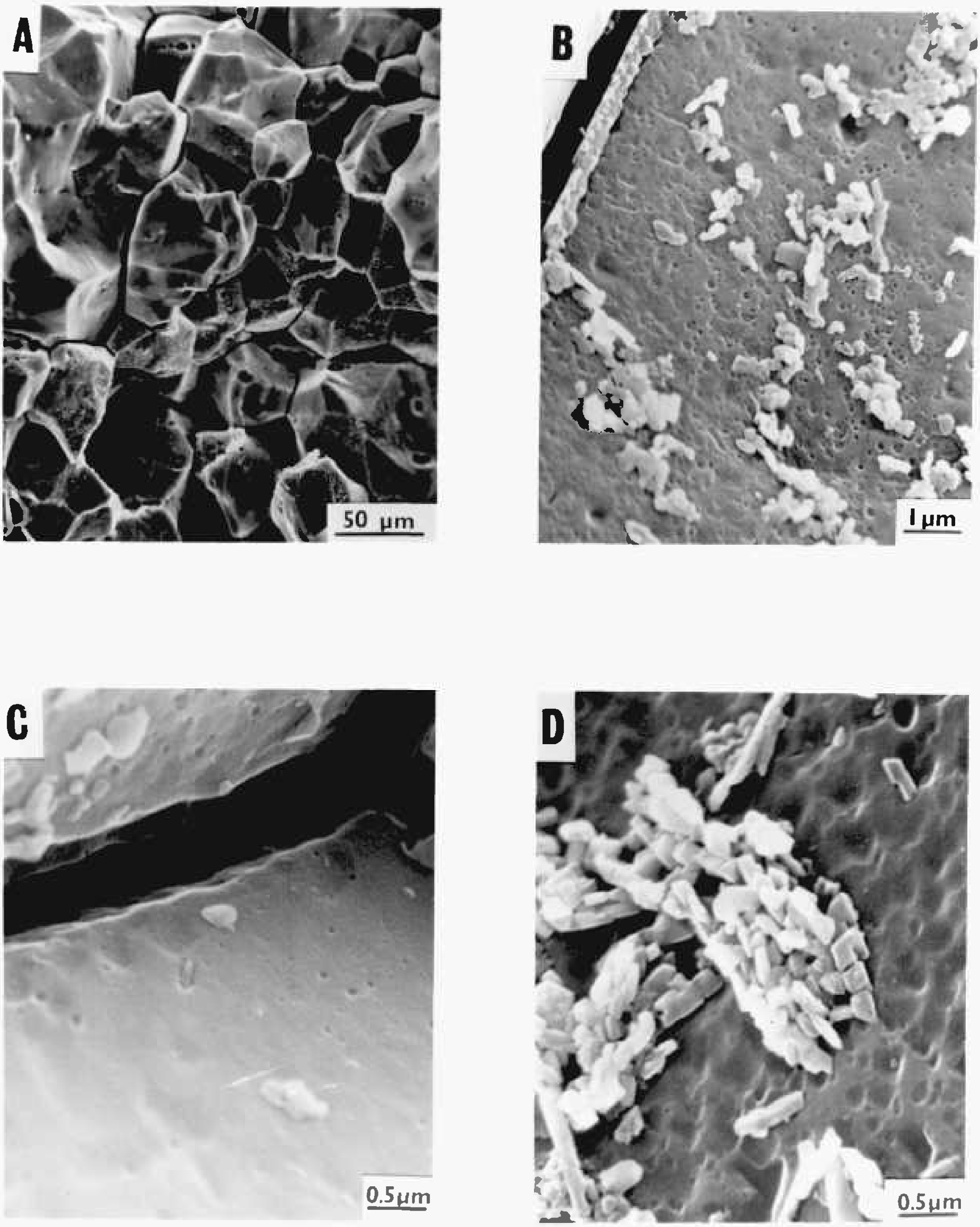
A
50 µm
B
1 µm
C
0.5µm
D
0.5µm

Specimens sensitised for 2 hours and 24 hours at 675°C displayed similar behaviour to the 72 hour specimens during anodic testing. Strains to fracture were slightly greater than those observed for the heavily sensitised material. Representative micrographs in Figure 5.17 contain examples of slip-line attack and extensive dissolution and pitting.

Slow strain rate tests conducted under anodic potential in the pH=2 0.01M H_2SO_4 + 0.002 M NaCl solution yielded unexpected results. The 2 and 24 hour specimens exhibited no signs of dissolution attack. As illustrated in Micrographs A and B in Figure 5.18, failure was ductile. Intergranular tearing was predominant in the 24 hour specimens. The mechanical behaviour of these specimens was very similar to that of the control specimens (air-tested). Only the 72 hour treatment was susceptible to intergranular fracture under these conditions. However, the strain to failure was substantially greater than that in the pH=1 solution. Indications of plastic deformation (slip lines) are visible in Micrograph C.

The response of the 2 and 24 hour specimens to these controlled potential tests in the pH=2 environment prompted additional experiments on solution annealed material. Under cathodic potential, a brittle fracture resulted. Fractographic examination revealed 100% cleavage-like fracture with secondary intergranular separation, as shown in Micrographs A and B in Figure 5.19. The behaviour of the solution

Figure 5.17 Representative Fractographs of Sensitised Specimens Tested in pH=1 0.1M H_2SO_4 + 0.02M NaCl Solution Under Anodic Control (-140 mV SCE).

A) Sensitised for 2 hrs. @ 675°C

B) Sensitised for 24 hrs. @ 675°C

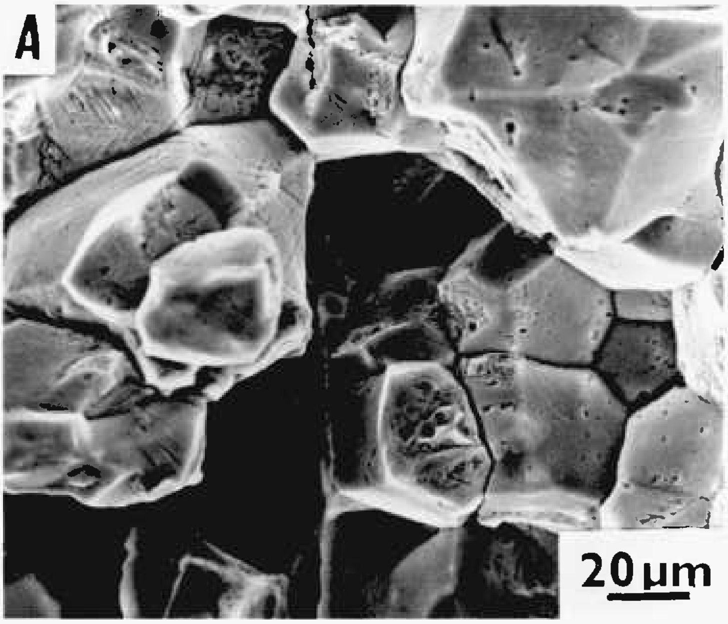
A
20 µm

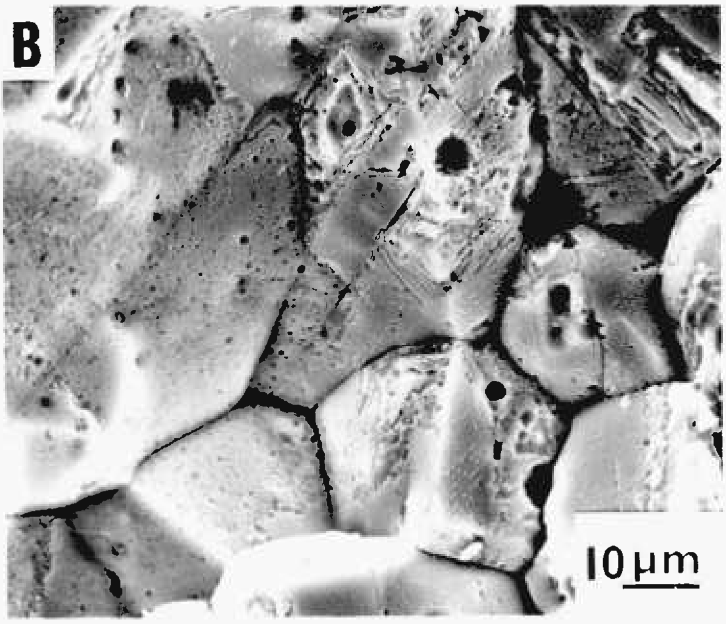
B
10 µm

Figure 5.18 Representative Fractographs of Sensitised Specimens Tested in pH=2 0.01M H_2SO_4 + 0.002M NaCl Solution Under Anodic Control (-140 mV SCE).

A) Sensitised for 2 hrs. @ 675°C

B) Sensitised for 24 hrs. @ 675°C

C) Sensitised for 72 hrs. @ 675°C

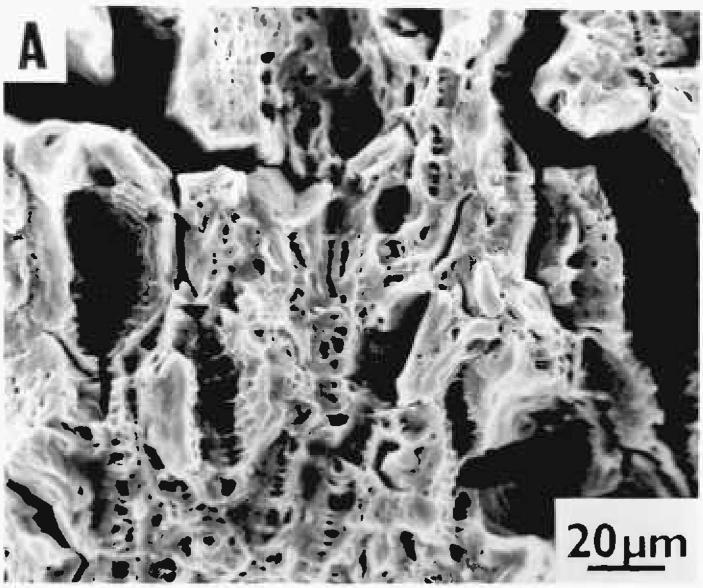
A
20μm

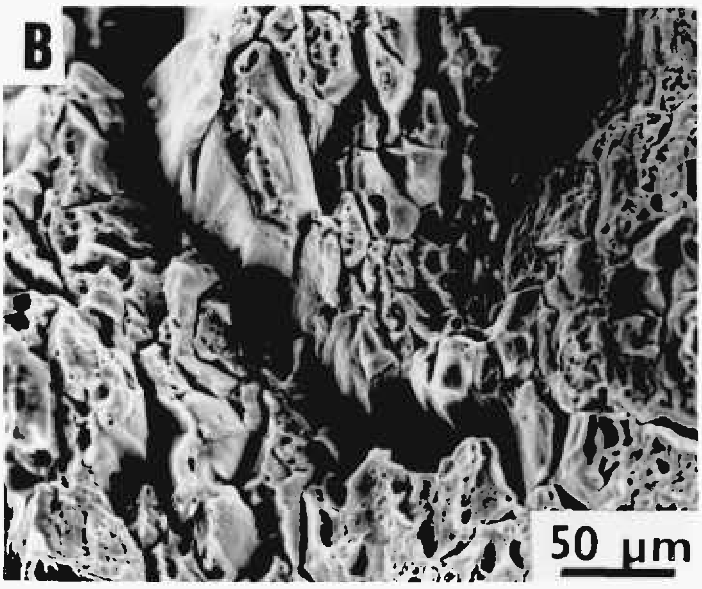
B
50 μm

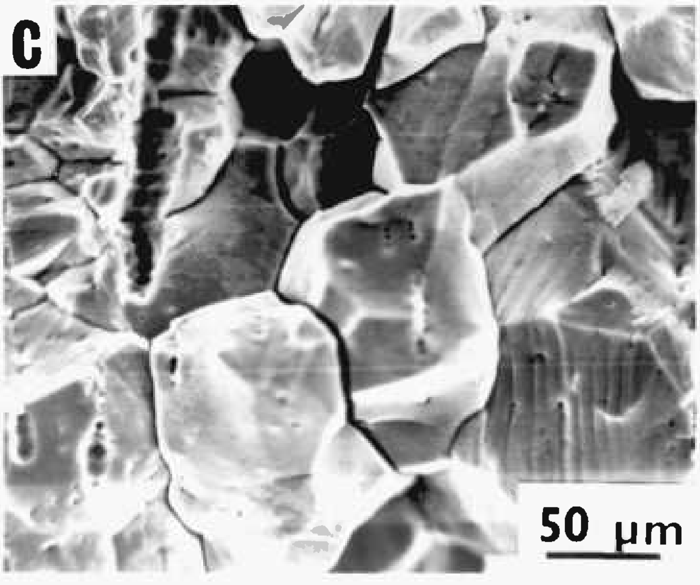
C
50 μm

Figure 5.19 Representative Fractographs of Solution Annealed Material Tested in pH=2 0.01M H_2SO_4 + 0.002M NaCl Solution Under Controlled Potential Conditions.
A,B) -650 mV SCE
C) -140 mV SCE

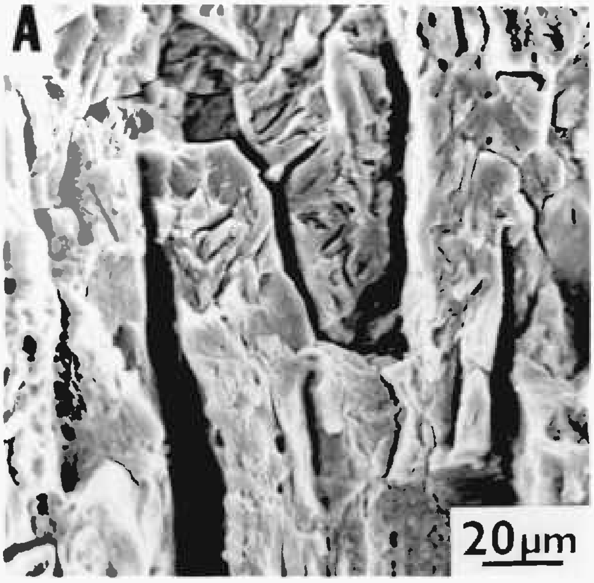
A
20µm

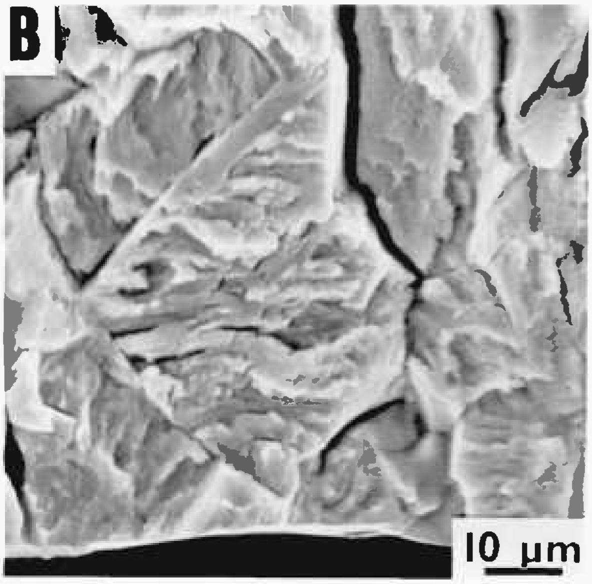
B
10 µm

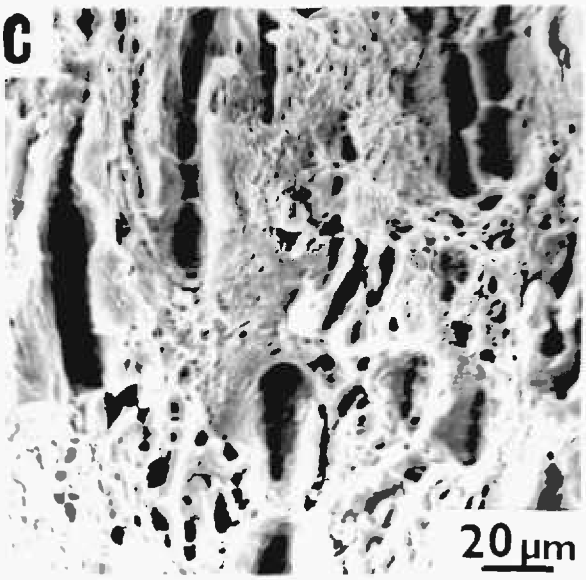
C
20µm

annealed specimen under anodic conditions was identical to that of the 2 and 24 hour specimens. Failure was entirely ductile (Micrograph C).

The results of the cathodically polarised tests were consistent for the heat treatments and solutions examined, but the behaviour of the sensitised specimens during the anodic tests was not in agreement with the predicted dissolution response. Further experiments were conducted in order to clarify this anomolous behaviour.

Additional anodic potential tests were performed to evaluate the effect of the chloride ion concentration on the SCC response of the sensitised material. Slow-strain rate tests on 72 hour specimens were conducted in pH=1 0.1 M H_2SO_4 + 0.002 M NaCl (NaCl concentration of the pH=2 solution), and in pH=2 0.01 M H_2SO_4 + 0.02 M NaCl (NaCl concentration of the original pH=1 solution) at -140 mV SCE. The experiments in the new pH=1 solution yielded identical results to those obtained in the 0.1 M H_2SO_4 + 0.02 M NaCl solution (complete intergranular failure with minimal plastic deformation).

The specimens tested in the pH=2 0.01 M H_2SO_4 + 0.02 M NaCl solution failed intergranularly, but not in the same manner as the pH=1 test specimens. SEM examination revealed fine, regular markings (∿ 1.5 to 0.5μm in spacing) across the intergranular faces as depicted in Figure 5.20, Micrograph A. These markings resembled fatigue striations. These striations were parallel grooves, extending across rrain boundaries (Micrograph B). Discrete carbides were

Figure 5.20 Striation Morphology Observed after Testing in pH=2 0.01M H_2SO_4 + 0.02M NaCl Solution Under Anodic Control (-140 mV SCE) (72 hrs. @ 675°C)

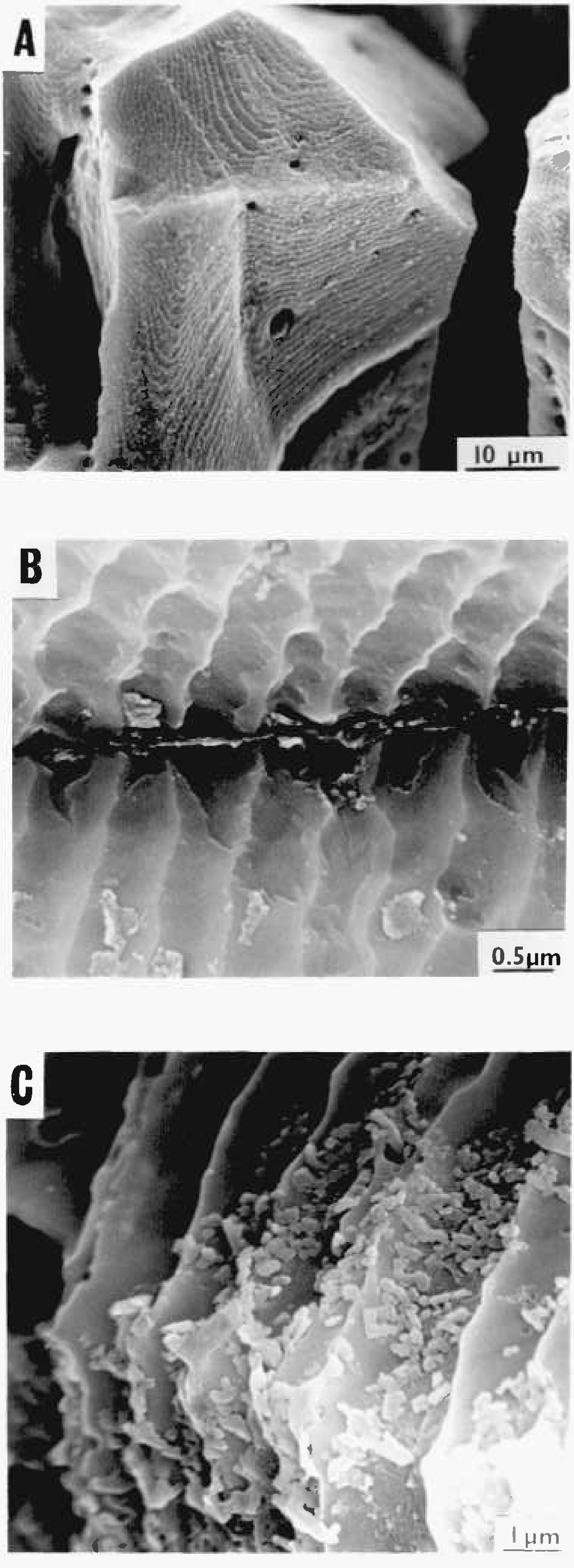
A
10 µm
B
0.5µm
C
1 µm

observed on some striations, as shown in Micrograph C. It was necessary to use stereo-microscopy in order to thoroughly examine these markings. A general intergranular area is contained in the upper streo pair in Figure 5.21. The striations do not indicate a brittle fracture, although the fracture surface, when viewed at low magnifications (∿500 X), did resemble a brittle intergranular fracture. In the central stereo-pair in Figure 5.21, fine slip lines can clearly be seen. These slip lines, however, appear to have been caused by plastic deformation after the crack had passed through that immediate area. The lower set of stereo micrographs in Figure 5.21 show other striations with some evidence of corrosion product. These striations appear as well defined steps.

In order to confirm that the striations are indeed 'crack arrest' markings, it is essential to demonstrate that the striations on opposite fracture surfaces match peak-to-peak. In Figure 5.22, two matching intergranular faces are presented. From those faces, detailed fracture matching has been successfully attempted. The features labelled A' and B' correspond to A and B from the opposite surface (Figure 5.23). The stereo micrographs included in Figure 5.23 illustrate that feature B is elevated while B' is a depression, and, most importantly, that the "striations" are peaks on each fracture surface. (For the stereo micrographs, B and B' have been rotated 90° in a clockwise direction with respect to the upper matched micrographs).

Figure 5.21 Various Stereomicrographs of Striation Features (tilt = 13°)

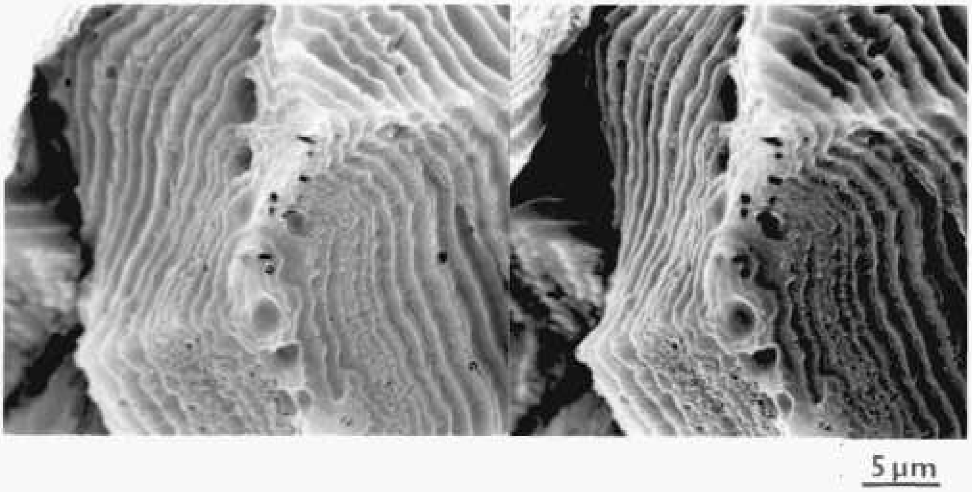
5 µm

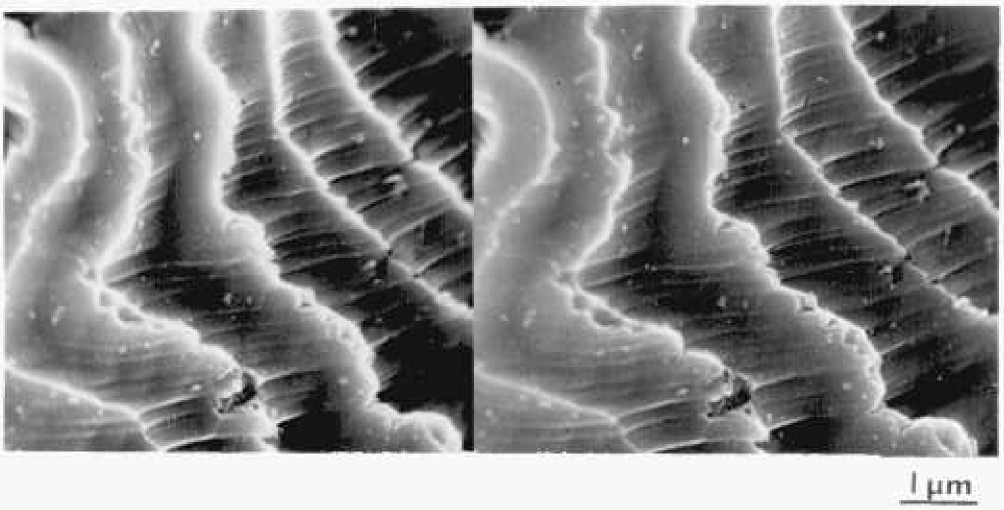
1 µm

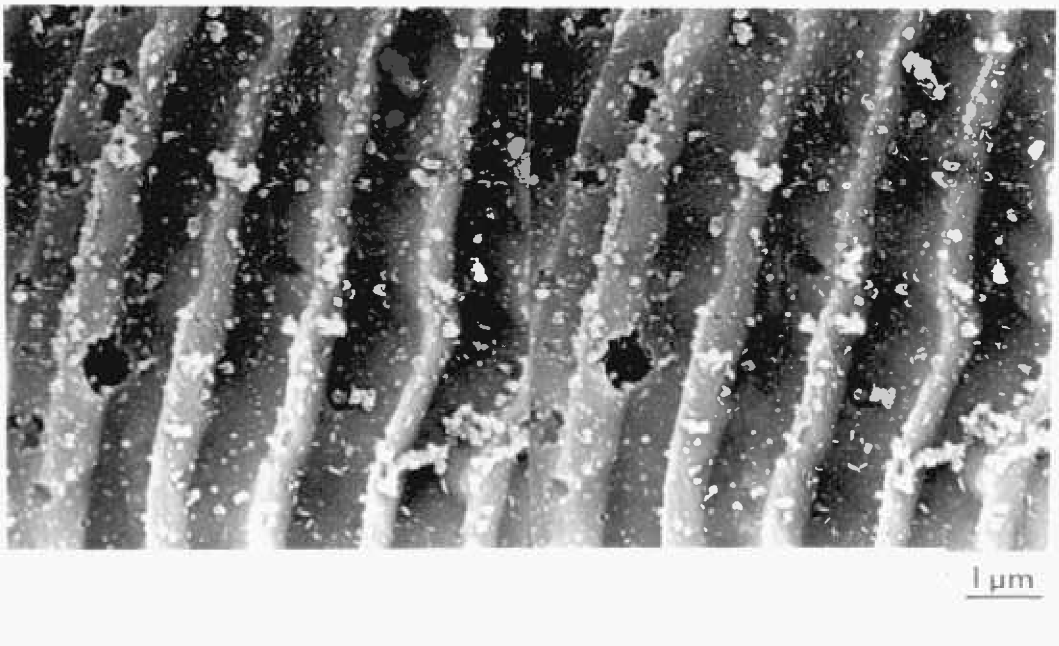
1 µm

Figure 5.22 Matching Fracture Surfaces of Specimen Tested in pH=2 0.01M H_2SO_4 + 0.02M NaCl Solution Under Anodic Control (-140 mV SCE).

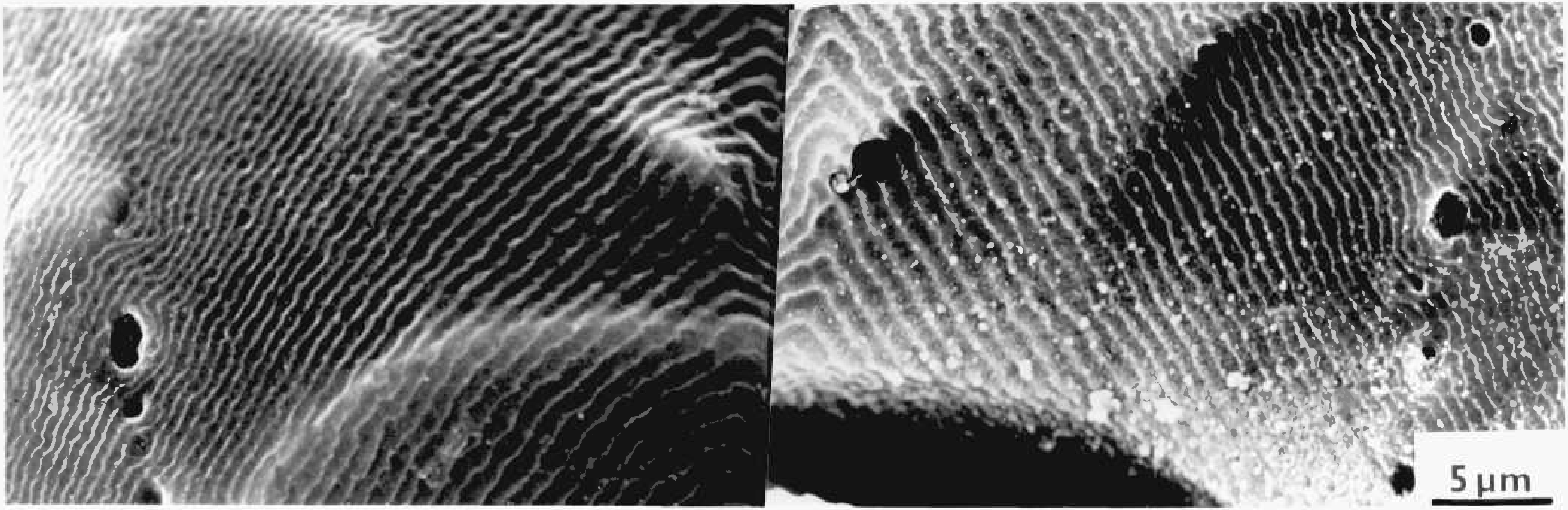
5 µm

Figure 5.23 Matching Fracture Surface and Stereo Micrographs Illustrating the Peak-to-Peak Matching of the Striations.
The matching features are A and A', and B and B'. The stereomicrographs depict B and B', and are rotated 90° with respect to the top matching fractographs.

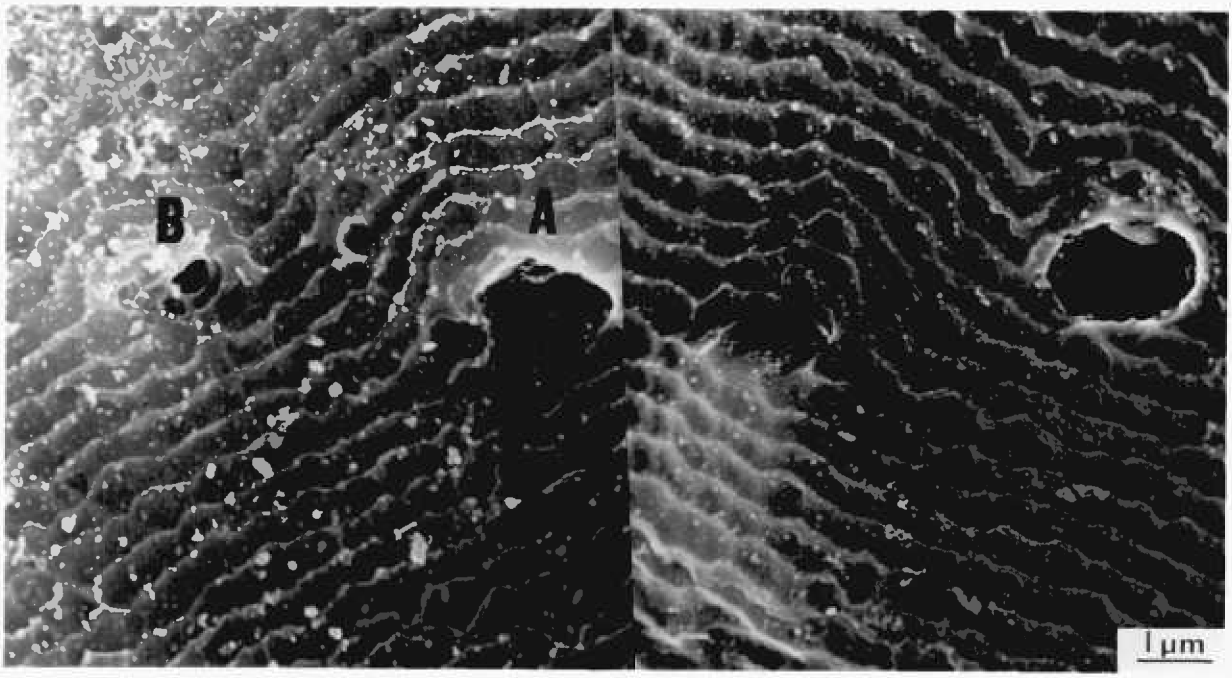
B
A
1 μm

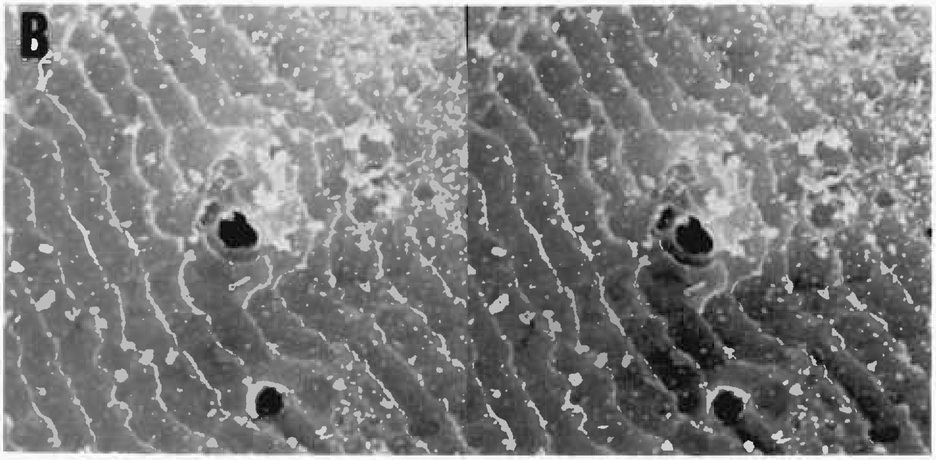
B

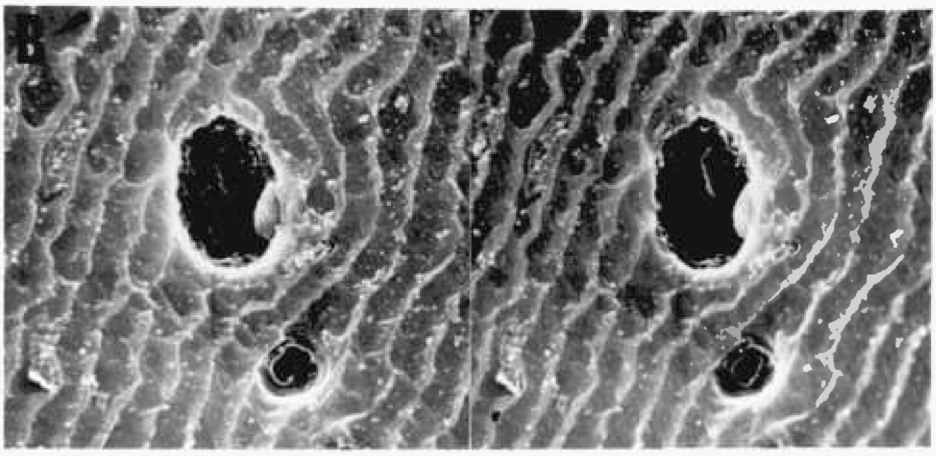
B

Areas which had been exposed to the SCC solution after the crack had passed developed extensive oxide and hydroxide coatings. Several micrographs of these oxides and hydroxides are presented in Figure 5.24. The upper micrograph illustrates the extent of the product and its formation over the crack-arrest markings. The plate-like structure (centre micrographs) of the coating was isomorphous with boehmite (AlOOH), and was morphologically identified as CrOOH (199). The lower micrograph depicts in detail corrosion product which has formed between the striation markings.

It was necessary to determine whether the "crack-arrest" markings were caused by the applied anodic potential or by the solution itself. Therefore, for comparison, slow strain rate tests were conducted in pH=2 0.01 M H_2SO_4 + 0.02 M NaCl at free corrosion conditions. Figure 5.25 includes representative micrographs of a fractured specimen. The fracture was predominantly intergranular with cleavage-like regions (Micrograph A). Micrographs B and C contain slip-line markings indicative of plastic deformation. No striations were observed. Failure strains were similar to those found for tests conducted in pH=2 0.01 M H_2SO_4 + 0.002 M NaCl solutions.

Figure 5.24 Micrographs of Fracture Surface with Corrosion Product

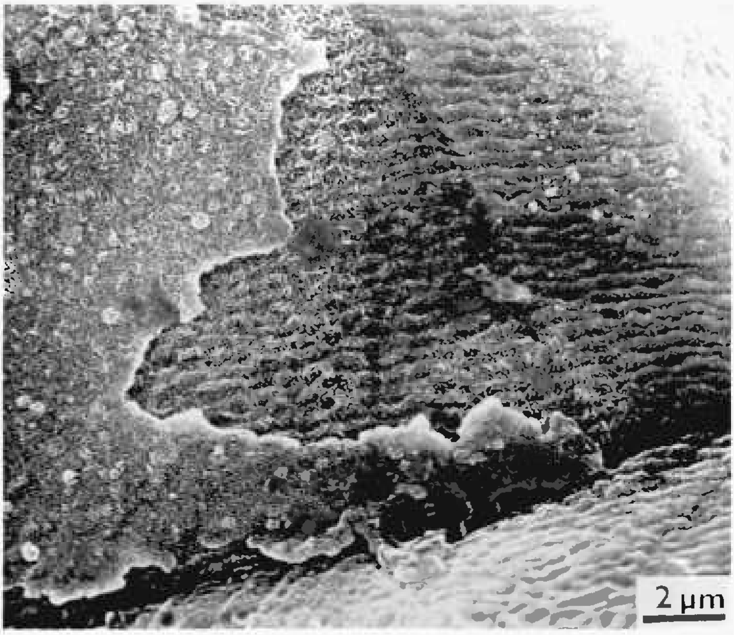
2 μm

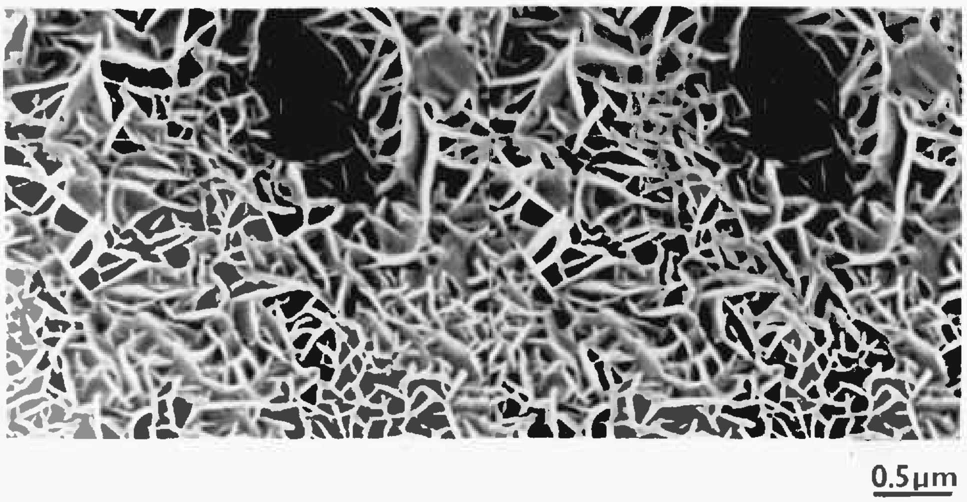
0.5μm

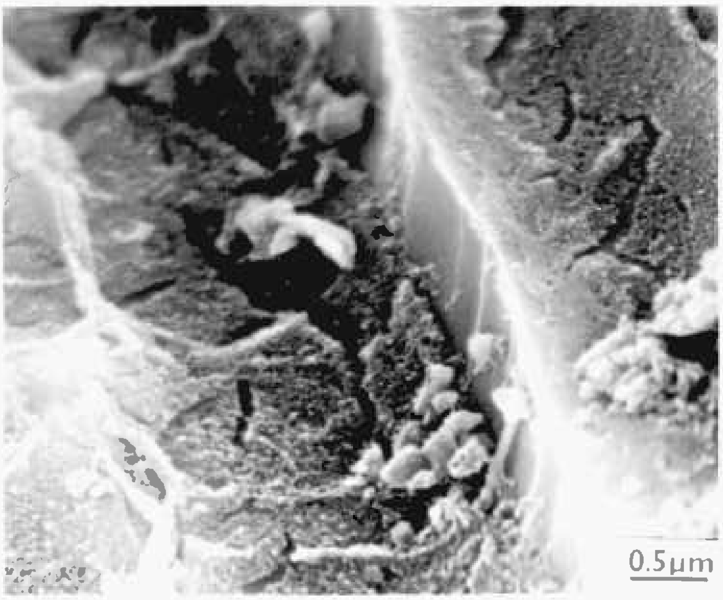
0.5μm

Figure 5.25 Fractographs of a Sensitised Specimen (72 hrs. @ 675°C) Stress Corroded in pH=2 0.01M H_2SO_4 + 0.02M NaCl Solution Under Free Corrosion Conditions.

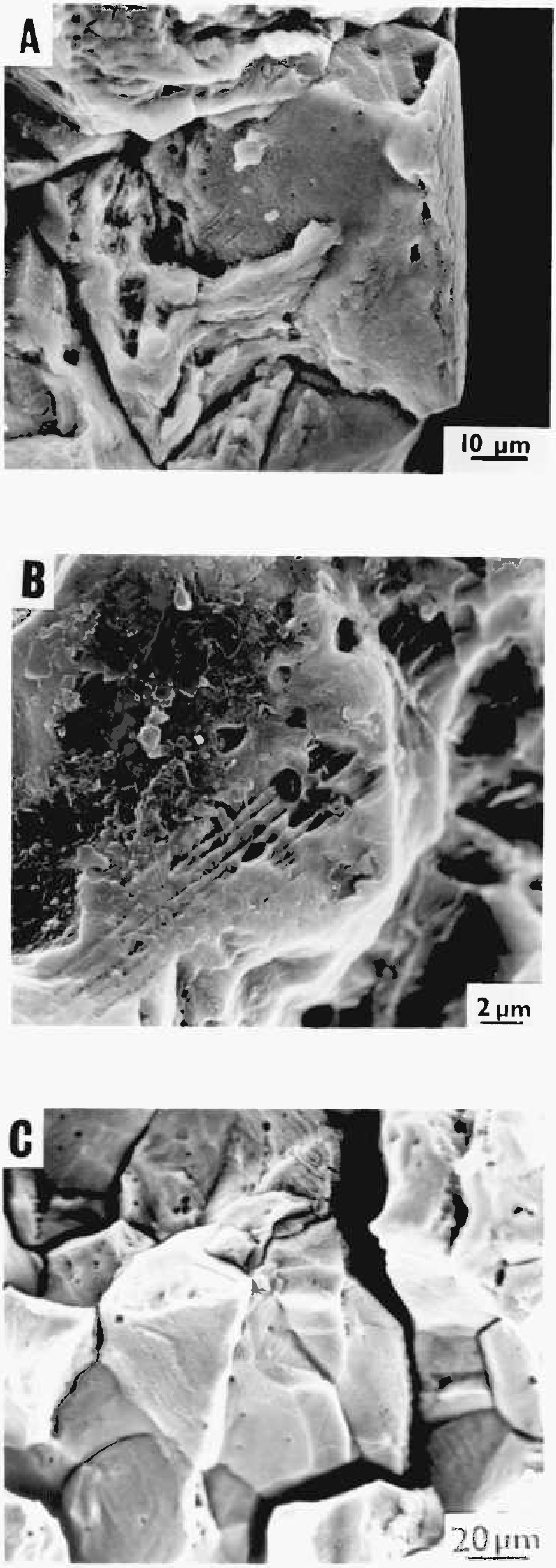
A
10 µm
B
2 µm
C
20 µm

5.4 DISCUSSION OF SLOW STRAIN RATE RESULTS

The results of the SCC experiments conducted at free corrosion conditions demonstrated a strong dependence of strain to failure on pH of the solution. Generally, as the pH of the solution increased, the failure strain increased. The corresponding fractographic evidence indicated that brittle intergranular and cleavage-like fracture were characteristic of SCC in low pH solutions. A transition in fracture mode occurred as the pH increased. The high fracture strains were associated with ductile failure. The type of dependence on pH would be expected for a hydrogen embrittlement or active path mechanism of SCC. The lower the pH of the solution, the greater the concentration of hydrogen ions and therefore hydrogen embrittlement of the metal would be enhanced. An acidic solution also affects the dissolution behaviour of the metal, so that a more acidic solution (lower pH) should be more susceptible to dissolution.

By conducting cathodic and anodic controlled potential tests, the susceptibility of the material to hydrogen embrittlement and anodic dissolution could be evaluated. Material susceptible to hydrogen embrittlement would be expected to fail prematurely under cathodic polarisation, while that prone to dissolution would fail more rapidly under an anodic potential. The data obtained under free corrosion and controlled potential conditions were combined in a graph of hydrogen activity as strain to failure (Figure 5.26). Hydrogen activity is related to the pH of the solution and the applied potential by the following expression:

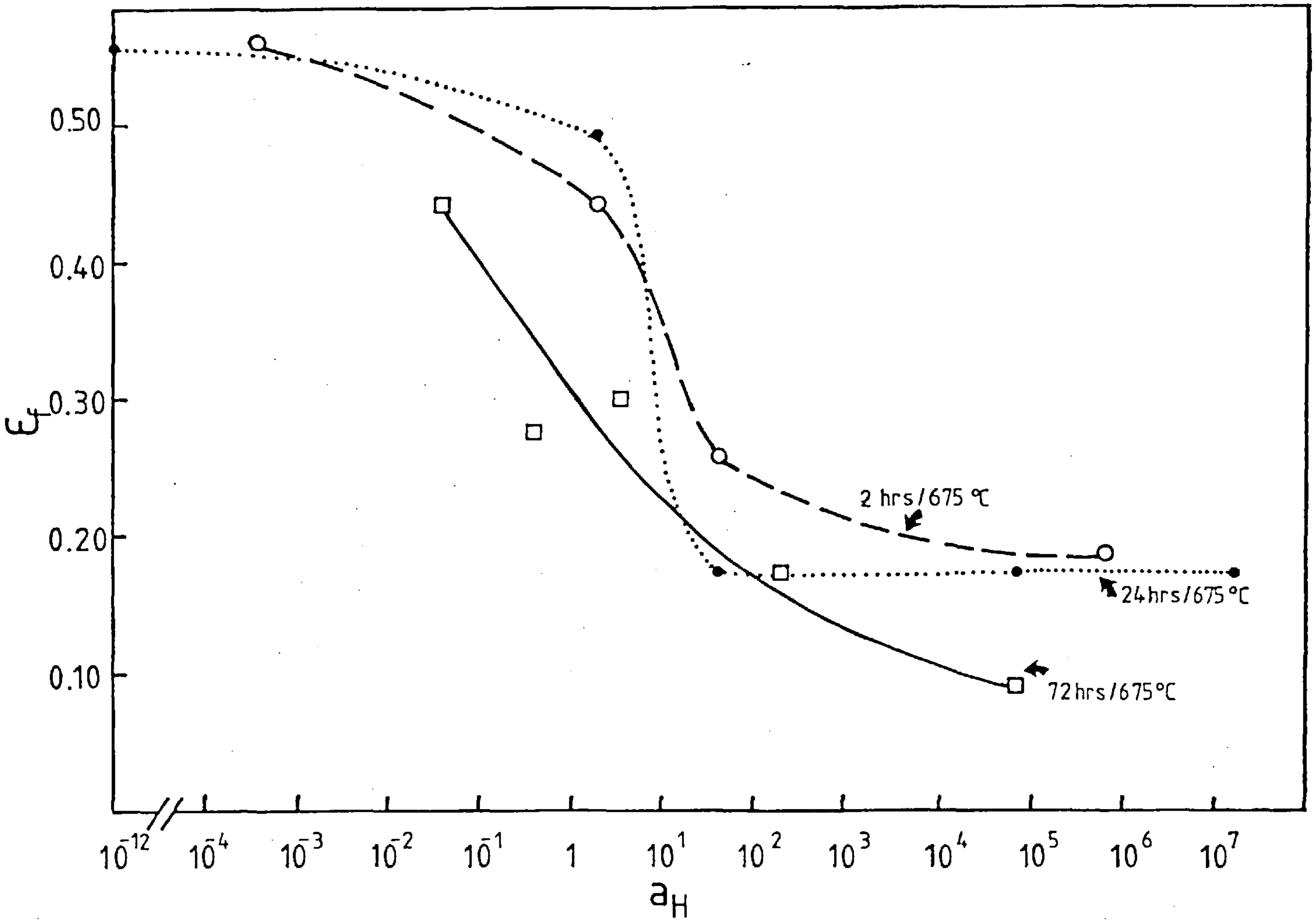

Figure 5.26 True Strain to Failure (ε_f) vs. Hydrogen Activity (a_H) For Free Corrosion and Controlled Potential Slow Strain Rate Tests.

$$a_{H_2} = 10^{-\left(\frac{244 + mV\ SCE}{59} + (pH) \right)}$$

All sensitisation treatments exhibited a similar trend. It was noted, however, that the 72 hour specimens were most susceptible to the a_{H_2} and SCC, while the 2 hour specimens were not as strongly affected. The family of curves for the 2 and 24 hour sensitisation treatments indicates that there is a substantial decrease in ductility (fracture strain) between hydrogen activities of 1 and 10. The transition regions for the 72 hour specimens occurs between values of 0.1 and 1. The hydrogen activity indicates whether there may be a tendency towards hydrogen embrittlement (high values of a_{H_2}) or dissolution (low values of a_{H_2}). It is not meant to be an absolute criterion for distinguishing between hydrogen embrittlement or dissolution. Fractographic observations and the SCC response of the material to applied potentials are required before a conclusion can be drawn.

In the region where $a_{H_2} << 1$, no intergranular SCC was observed for the 2 and 24 hour sensitisation treatments in the pH=2 solution at -140mV SCE. All failures were ductile. Altering the experimental conditions (by reducing the pH and increasing the potential) to produce the equivalent hydrogen activity as in the pH=2 tests resulted in intergranular failure at approximately the yield stress. Clearly, the acidity of the solution, rather than the hydrogen activity, is responsible for the rapid dissolution failure of the specimen. The polarisation curves obtained for the similated Cr-depleted austenite indicated that there was a slight shift to more noble values of E_{corr} with increasing pH. On the basis of the curves, the potentials chosen for the anodic experiments should favour dissolution.

By superimposing a graph of the failure strain vs. potential on a polarisation curve of an experimental Fe-Ni-10Cr alloy (simulating the low chromium austenite adjacent to the sensitised grain boundary), the relative importance of dissolution (anodic side) or hydrogen embrittlement (cathodic side) on the SCC behaviour could be observed. A significant decrease in fracture strain occurs at cathodic potentials, whereas anodic potentials appear to have little if any effect on SCC susceptibility in the pH=2 solution. As the application of an anodic potential accelerates dissolution while a cathodic potential promotes hydrogen embrittlement, the results of the controlled potential tests (as plotted in Figure 5. 27) indicate that failure is due to hydrogen embrittlement.

The chloride ion concentration was found to exhibit a marked effect on the stress corrosion behaviour in the pH=2 solution. As the chloride ion concentration increased, the strain to failure decreased, particularly under conditions of anodic control. By employing the pH=2 0.01 M H_2SO_4 + 0.02 M NaCl solution, it was possible to drastically reduce the additional acid attack which was observed to occur in the pH=1 solution in the -140mV SCE experiments.

The existence of striation markings over the intergranular fracture surface under the anodic conditions examined

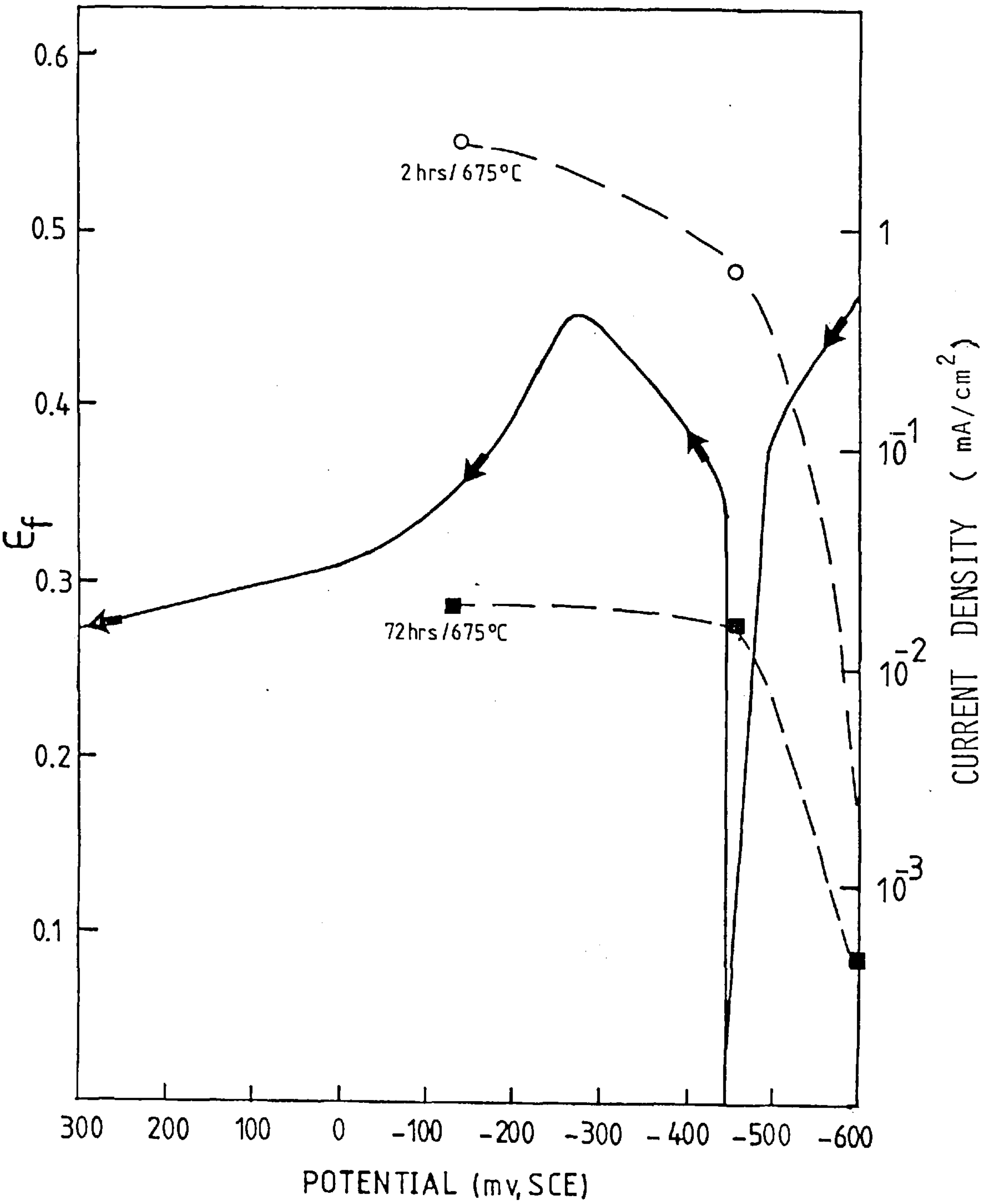

Figure 5.27 The Effect of Applied Potential on the SCC Behaviour of Sensitised 304. The polarisation curve depicts the response of the Cr depleted grain boundary region (∿10 wt.% Cr) in 0.01M H_2SO_4 + 0.002M NaCl solution.

in this study indicated that stress corrosion crack propagation was discontinuous. The matching of opposite fracture surfaces provided a peak-to-peak type fit of the striations. This confirmed that the striations were crack-arrest markings (87).

Striation formation was only observed in the 0.01 M H_2SO_4 + 0.02M NaCl (pH=2) solution at -140mV SCE. and was directly related to the chloride ion concentration (no striations were detected in pH=2 0.01M H_2SO_4+ 0.002M NaCl at -140mV SCE). As the striations appeared at parallel grooves, it is most likely that they are formed at the result of localised dissolution of clean metal which is exposed to the solution. A crack advances by some mechanism, and blunts, with the clean metal crack walls available for subsequent dissolution. The applied anodic potential of -140 mV SCE is located in the negative slope region of the anodic peak (Figure 5.27). When clean metal is exposed to the solution, the potential shifts to the right towards the active peak, and dissolution is promoted. The potential then drifts to the left and the metal passivates (200). The resultant morphology would be similar to that depicted in the fractographs in Figures 5.20 - 23. The striations merely accentuate the crack arrest markings. Striation formation is proposed to be a post-crack advance dissolution process accompanying discontinuous crack propagation. The promotion of striation formation by the high chloride ion concentration of the solution is consistent with the reported effect of chloride ions on dissolution behaviour (197).

No striations were observed in specimens tested in the 0.002M NaCl pH=2 solution at -140mV SCE. This does not imply that different mechanisms of crack propagation may be operating. It is possible that the crack is still advancing discontinuously, with clean metal being exposed to the solution. Since the chloride ion concentration is lower (solution is not as aggressive), dissolution of the clean metal is a slower process, and the resultant fracture surface appears to be the result of intergranular dissolution. Any indications of crack-arrest markings would be masked by the subsequent dissolution.

The mechanism by which the crack propagates discontinuously will be discussed in Section 7.1.

Stress corrosion cracking in dilute H_2SO_4+ NaCl solutions was not accompanied by any features which were indicative of discontinuous crack propagation under free corrosion conditions or under cathodic control. An extensive fractographic examination revealed distinct similarities between free corrosion SCC failures and cathodically polarised (hydrogen embrittled) specimens. Fracture matching has indicated that, indeed, an embrittlement mechanism is operative. The example presented in Figure 5.28 illustrates the variety of fracture modes observed in a sensitised (72 hours @ $600^{\circ}C$) specimen which had failed in a pH=3 (0.001 M H_2SO_4 + 200 ppm NaCl) solution. A brittle intergranular region existed near the specimen surface. A zone of cleavage-like fracture separated the intergranular fracture from the central ductile region. Figure 5.29 contains two examples of this transgranular fracture. Micrograph A represents a portion of the cleavage-like fracture observed in Figure 5.28. An identical fracture mode is contained in Micrograph B. Unlike Micrograph A, however, this fractograph was obtained from a cathodically polarised specimen (2 hours @ 675°C) tested in a pH=1 solution. Clearly, on the basis of the fractographic evidence and the response of the material to applied potential, both fractographs are manifestations of hydrogen embrittlement.

It appears, therefore, that excessive dissolution can mask evidence of cleavage-like fracture. Both processes of hydrogen embrittlement and anodic dissolution may occur at the same time, but at different rates as indicated in Figure 5.5. A discussion of the mechanism of SCC in sensitised 304 is presented in Chapter 7.

Figure 5.28 Matching Fracture Surfaces Sensitised Specimen (72 hrs. @ 600°C) Stress-Corroded in pH=3 H_2SO_4 + NaCl Solution.

Figure 5.29 Fractographs of Sensitised Specimens After Testing in:

A) pH=3 0.001M H_2SO_4 + 0.0002M NaCl Solution Under Free Corrosion Conditions (72 hrs. @ 600°C)

B) pH=1 0.1M H_2SO_4 + 0.02M NaCl Solution Under Cathodic Control (-650 mV SCE) (2 hrs. @ 675°C)

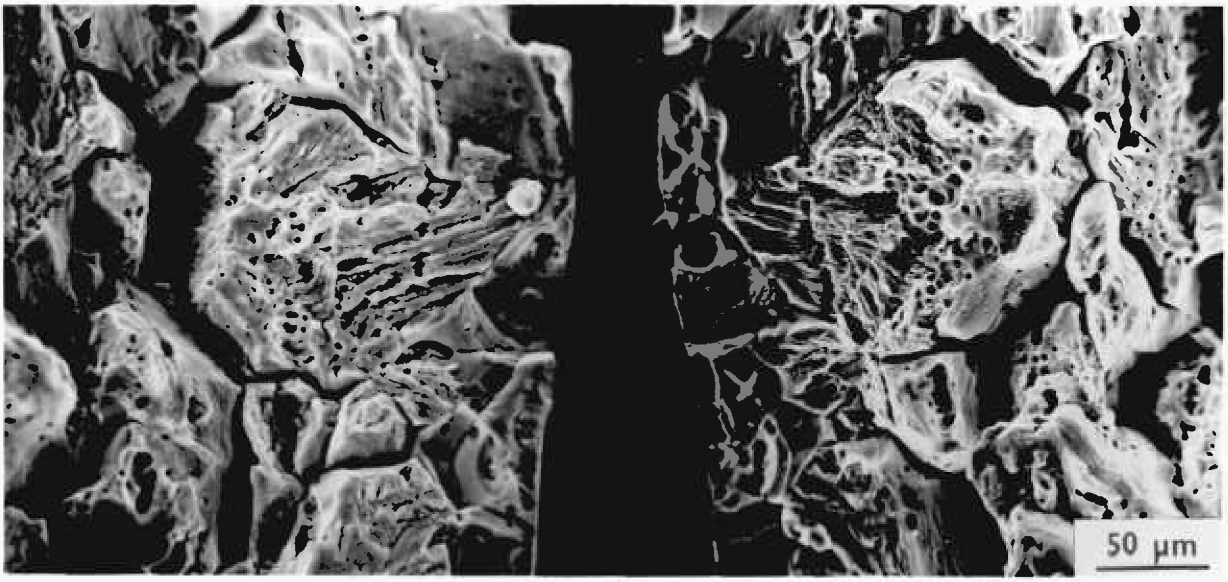
50 µm

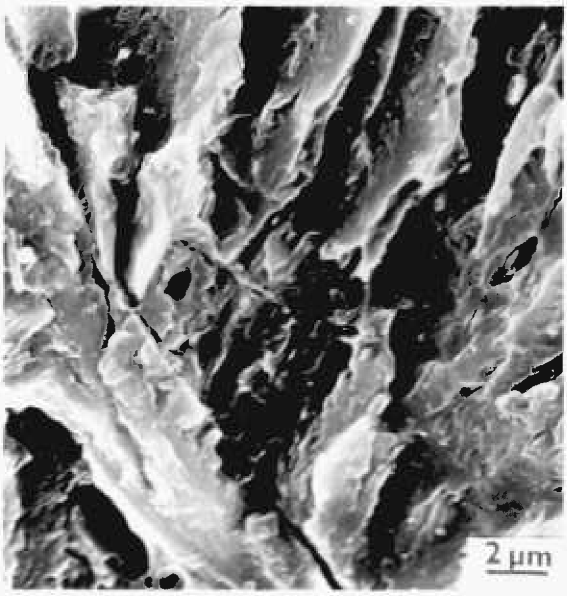
2 µm

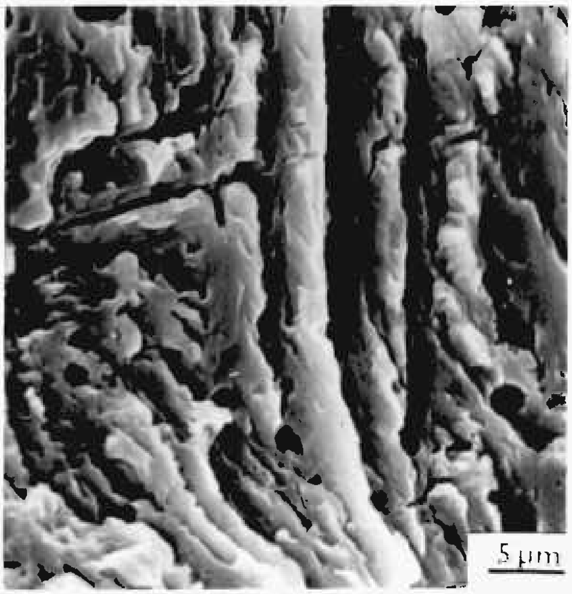
5 µm

CHAPTER 6

THE INFLUENCE OF HYDROGEN ON THE MICROSTRUCTURE AND PROPERTIES OF SENSITISED AUSTENITIC STAINLESS STEEL

6.1 "IN-SITU" OBSERVATIONS IN THE GAS REACTION CELL

As the susceptibility of sensitised type 304 stainless steel to hydrogen embrittlement has been documented (100, 201), it was proposed to examine the microstructural nature of the hydrogen-metal reaction by employing HVEM and the Gas Reaction Cell (GRC). This technique has proved to be most successful for studies of hydrogen embrittlement of aluminium alloys in water vapour (155,202). The environment selected for this investigation was H_2O vapour-saturated helium at 20°C. A pressure of approximately 100 torr was maintained in the GRC. Sensitised specimens, prepared by the technique described in Section 2.4.2, were examined in the as-heat treated or as-deformed condition. By studying the deformed material, the influence of the 'grain boundary' martensite on any hydrogen-metal reaction could be evaluated.

The results of the "in-situ" GRC experiments revealed that no microstructural changes occurred when the specimens were exposed to H_2O vapour environments. Only a small degree of surface reaction was observed as depicted in Figure 6.1. There was no preferential reaction at the grain boundary regions in either the strained or unstrained

Figure 6.1 Micrograph of Sensitised Specimen After Exposure for 10 Minutes in the GRC.

Figure 6.2 Radiation Damage After 20 Minutes Exposure in the GRC (operating voltage = 1 MeV)


0.5µm

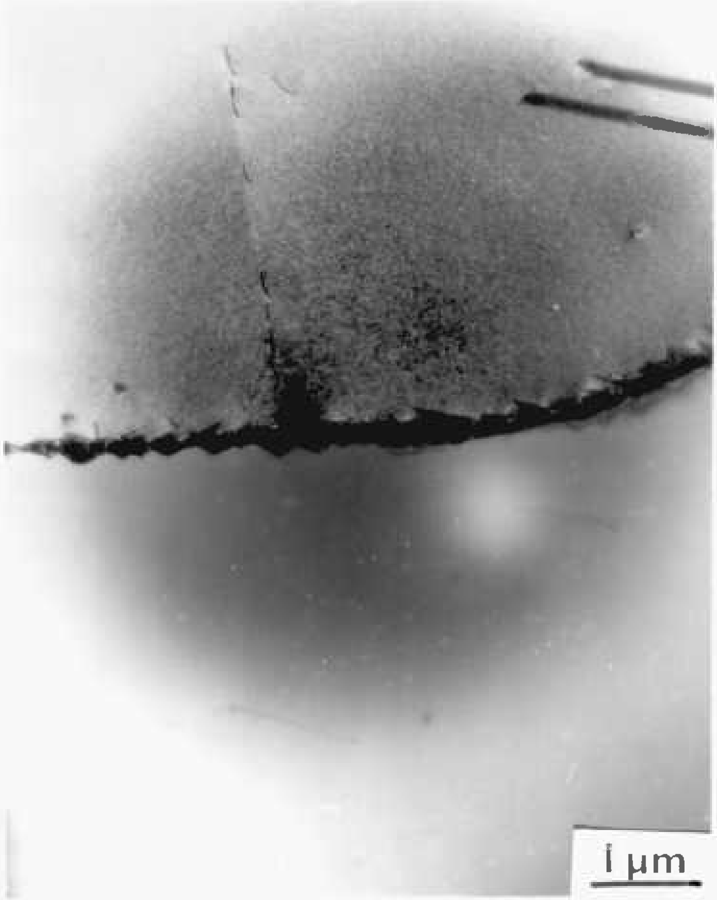
1 µm

material for exposure times up to 30 minutes. The accelerating voltages used for these experiments were 500kV and 1MeV. Increasing the accelerating voltage promoted radiation damage of the metal. The extent of the radiation damage induced in a sensitised specimen is illustrated in Figure 6.2.

6.2 EFFECT OF HIGH-TEMPERATURE STEAM ON THE BEHAVIOUR OF SENSITISED TYPE 304 STEEL

Although no microstructural changes were observed during the exposure of steel to water vapour in the GRC the reported failures of sensitised 304 in BWR environments(15, 37,203) prompted an investigation into the behaviour of the material in steam at elevated temperatures.

Initial results of mechanical properties of sensitised specimens 'pre-exposed' to steam at 120°C (pressure of 2.06 bars) for 90 days revealed no decrease in ductility or any fractographic evidence of hydrogen embrittlement. As conditions in BWR environments (343°C H_2O) are more severe than those in the 120°C autoclave, it was decided to "pre-expose" specimens in steam at 320°C and one atmosphere pressure. A steam cell, described in Section 2.5.2, was designed to accommodate "pre-exposure" and "U-bend" type tests in high temperature, dry steam.

No embrittlement was detected for any specimens tested at 340°C for prolonged periods (40 days). All specimens, unstressed or pre-strained, failed in a ductile manner. Typical fracture morphologies are presented in

Figure 6.3 Representative Fractographs of Sensitised Specimens Tested After Exposure to Dry Steam (340°C) for 40 Days.

A) Sensitised for 2 hrs. @ 675°C

B) Sensitised for 24 hrs. @ 675°C

C) Sensitised for 72 hrs. @ 675°C

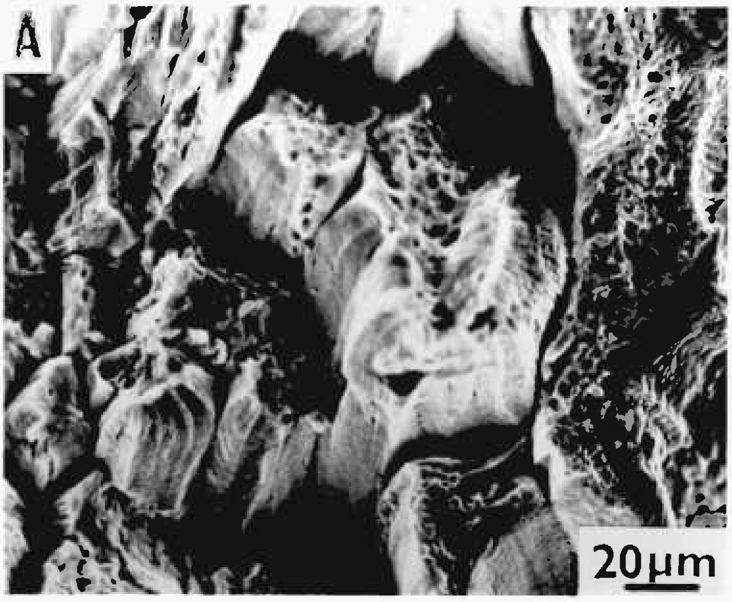
A
20µm

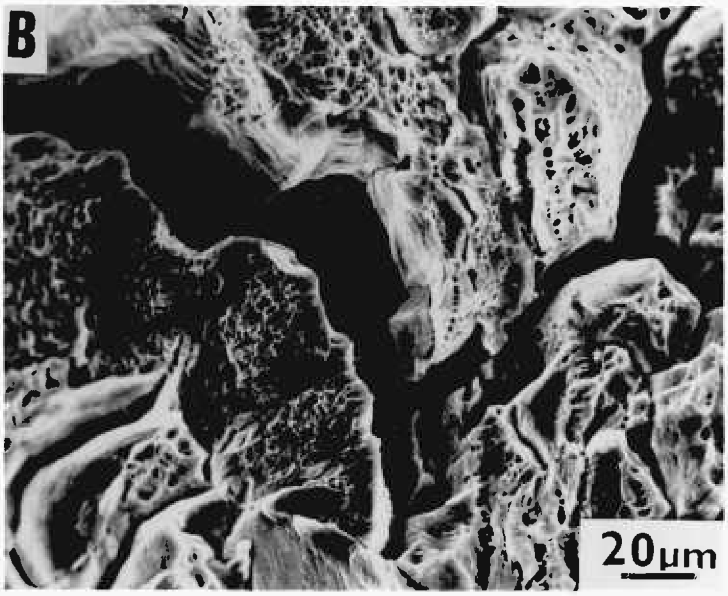
B
20µm

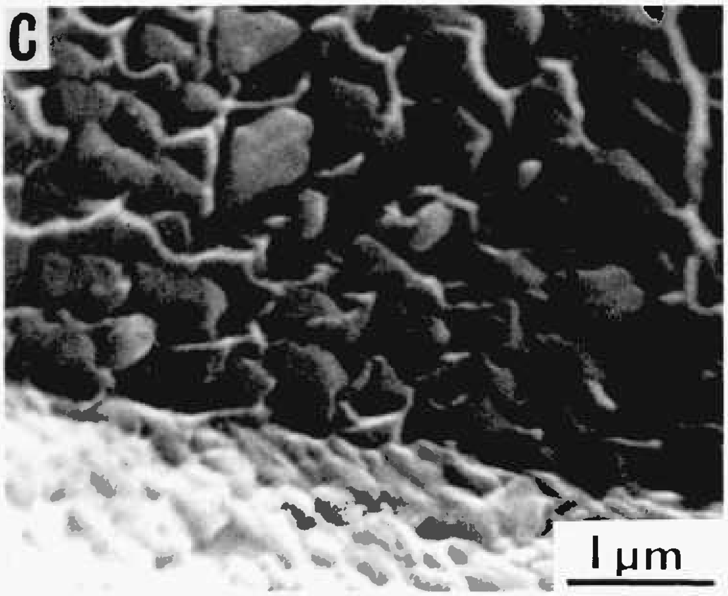
C
1 µm

Figure 6.3. Micrograph A depicts the type of fracture in the unstressed specimens, while B and C represent the pre-strained material. Intergranular tearing, characteristic of ductile failure in an inert environment, occurred in addition to dimpling. Micrograph C illustrates a region of intergranular tearing caused by the presence of carbides at the grain boundaries.

6.3 EFFECT OF CATHODICALLY PRODUCED HYDROGEN ON THE MICROSTRUCTURE OF SENSITISED TYPE 304 STEEL

Numerous studies have been conducted on cathodically-charged solution annealed type 304 steel to determine the effect of dissolved hydrogen on the microstructure and mechanical behaviour (127, 147, 204). It has been reported that the presence of hydrogen leads to severe internal stresses in the austenite (126, 150), and can induce the $\gamma\rightarrow\varepsilon$ or $\gamma\rightarrow\alpha'$ transformation. Hydrogen also reduces the stacking fault energy in austenitic stainless steels (205).

The microstructural effect of hydrogen in sensitised austenitic stainless steel was evaluated through examination of cathodically charged specimens. Electrolytic charging was conducted in a 2 vol.% H_2SO_4 solution containing $\sim$250 mg/ℓ of sodium arsenate as a hydrogen recombination poison. Thin foil specimens were charged for periods of 3 to 15 min. at a current density of approximately 70 mA/cm^2 at 25°C. Examination of the charged specimens in the transmission electron microscope revealed extensive faulting

Figure 6.4 Representative Micrographs of Heavily Sensitised Specimens (72 hrs. @ 675°C) After Cathodic Charging at 25°C .

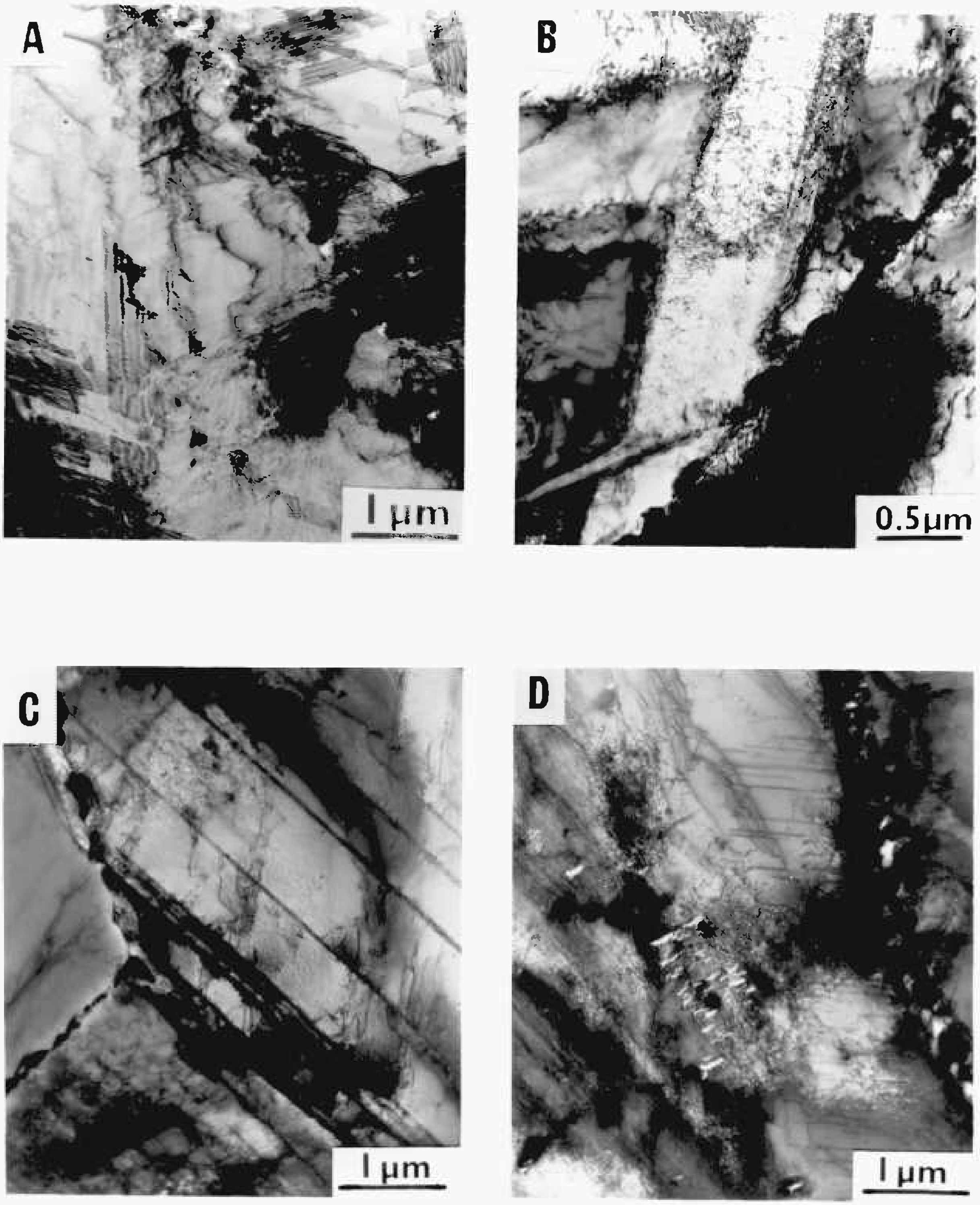
A
1 µm
B
0.5µm
C
1 µm
D
1 µm

and twinning in the austenite (Figure 6.4, A). This rather high degree of deformation induced the transformation of $\gamma \rightarrow \alpha'$ at many grain boundaries (Micrograph B). Regions of ε martensite were observed in the γ after charging (Micrographs A and C). In addition to the deformation structures, intragranular cracking was detected (Micrograph D). The cracks were crystallographic in nature and appear to grow in $<111>$ directions. The observed crack morphology and crystallography are remarkably similar to the slotted dissolution morphology observed by Scamans in studies of SCC initiation in LiCl (61).

6.4 DISCUSSION

6.4.1 "Pre-Exposure" Results

Austenitic stainless steel is susceptible to hydrogen embrittlement in the solution annealed or sensitised condition. In this investigation, however, no embrittlement effects have been detected in specimens which were pre-exposed to water vapour. Although numerous examples of intergranular cracking of sensitised 304 in BWR environments have been reported in the literature, due to the inability to obtain the high temperature (288°C) and high pressure ($\sim$ 100 atm) H_2O environment in the laboratory, it was not possible to duplicate the BWR conditions.

Two important factors which may account for the low reactivity of the metal with water vapour in the laboratory test conditions are the hydrogen fugacity, and the presence of the oxide film on stainless steel.

6.4.1a Hydrogen Fugacity

Austenitic stainless steel can become embrittled when tested in hydrogen gas or by the introduction of hydrogen electrolytically (cathodic charging). Briant (100) has recently reported instances of hydrogen-assisted cracking of sensitised Type 304 steel in one atmosphere of H_2. This is equivalent to a hydrogen fugacity of 1. The hydrogen fugacity can also be increased by cathodically charging the steel. Introduction of hydrogen into the steel in this manner results in embrittlement.

In the high temperature steam cell, sensitised specimens were exposed to 320°C dry steam at one atmosphere. Thermodynamic calculations indicate that the partial pressure of H_2 is equilibrium with H_2O under these conditions in approximately 10^{-38}atm. This corresponds to a comparably low fugacity of hydrogen. It is anticipated that the hydrogen fugacity in the GRC is substantially lower than that in the steam cell. These values are significantly lower than the values of the hydrogen activity calculated for the stress corrosion test conditons. If the reactivity of hydrogen with the metal is dependent upon fugacity, then the observed behaviour is consistent with the role of hydrogen fugacity in embrittlement.

6.4.1b Oxide Film

The oxide film formed on austenitic stainless steel is an effective barrier to hydrogen penetration (60).

This is particularly so in a pre-exposure test where film rupture due to straining cannot occur. Piggott and Siarkowski (60) have shown that the diffusivity of hydrogen in the oxide is very dependent upon composition, with films of α-Fe_2O_3 having a much lower D_H ($1 \times 10^{-18} cm^2/sec$) than Cr_2O_3($9.2 \times .0^{-16} cm^2/sec$). The hydrogen diffusivity (in the oxide) was observed to change with increasing thickness as a result of compositional variations in the oxide. Oxide films approximately 1000Å or less in thickness were most effective in inhibiting the flux of hydrogen through the oxide. Piggott and Siarkowski noted that the hydrogen flux through thick (> 1000Å) oxide films was very similar to results obtained on clean metal, indicating that cracking of the oxide had occurred. The importance of the oxide film in hydrogen permeation studies was also reported by Louthan and Derrick (206). Electropolished stainless steel were more effective in reducing hydrogen permeation than were mechanically polished specimens. Exposure of austenitic stainless steel to water vapour resulted in a dramatic reduction of hydrogen permeability.

The experimental observations regarding the influence of hydrogen on the microstructure and properties of sensitised 304 described in Sections 6.1 - 6.2 can be readily explained by the low hydrogen fugacity and the inhibiting effect of the oxide film (particularly in wet environments) on hydrogen permeation. Hydrogen introduced by cathodic charging techniques did induce microstructural changes. The absence of any hydrogen-effects in the "pre-exposure" tests indicates that very little hydrogen - if any -

could enter the metal.

6.4.2 Cathodic Charging Results

The primary objective of cathodically charging sensitised specimens with hydrogen was to determine whether the stresses involved in introducing hydrogen into the metal would be sufficient to promote the $\gamma\rightarrow\alpha'$ and $\gamma\rightarrow\varepsilon$ transformations. This was successfully accomplished.

An additional feature of cathodic charging at room temperature is the formation of fine, crystallographic, intragranular cracks in the austenite. This preliminary study indicates that these cracks are not related to α' or ε martensite, but may be due to hydrogen embrittlement of the austenite, a view shared by other investigators (138 ,207). The similarity of the crack morphology + crystallography with the dissolution attack observed by Scamans (61) in his investigation on SCC of austenitic stainless steels is 150^{o}C LiCl suggests that the two types of attack may be related. It is possible, of course, that hydrogen cracking and dissolution proceed in the same mode in this system. Clearly, this area requires further investigation.

CHAPTER 7

DISCUSSION

7.1 SUMMARY OF MAIN RESULTS

7.1.1 Microanalysis and Microstructure

The existence of a chromium depleted zone adjacent to sensitised grain boundaries has been directly confirmed by quantitative energy-dispersive microanalysis. This investigation has revealed that the chromium content in the zone falls below the ∿ 12 wt % required for passive film formation. It was observed that the extent of the depleted region was directly related to the temperature and time of sensitisation. As predicted by thermodynamic analysis, the minimum chromium content at the grain boundary (carbide-austenite interface) decreased as the sensitisation temperature decreased. This was reflected by the presence of martensite in the chromium depleted zone along certain grain boundaries. Martensite was found to form more readily in specimens sensitised at lower temperatures. However, the martensite transformation could also be induced by plastic deformation.

7.1.2 IGSCC Results

Results of the slow strain rate (SSR) tests in dilute H_2SO_4 + NaCl solutions have indicated that IGSCC is dependent upon pH. SCC failure was found to be mainly intergranular with small regions of "feathery" cleavage-like fracture. This "feathery" fracture was characteristic of the hydrogen embrittlement failures in the SSR tests conducted under cathodic potential. Anodically polarised specimens failed intergranularly in the most acidic solutions (pH=1), however, no evidence of IGSCC was detected in the more dilute solutions. (Failure was completely ductile).

The results of the free corrosion and controlled potential SSR tests, presented in a graph of ε_f vs. a_{H_2} (hydrogen activity) - Figure 5.26- revealed that a transition in SCC behaviour occurred at a hydrogen activity of approximately 1 for all sensitisation treatments. The regime of hydrogen embrittlement was defined as $a_{H_2} > 1$, while the $a_{H_2} < 10^{-1}$ was characterised by dissolution.

Conclusive evidence of the discontinuous nature of IG crack propagation was obtained from SSR tests conducted under anodic control in pH=2 0.01 M H_2SO_4 + 0.02 M NaCl. By increasing the Cl^- concentration in the pH=2 solution, it was possible to observe crack arrest markings over the intergranular SC surface. These features were not detectable in the pH=1 0.1 M H_2SO_4 + 0.02 M NaCl solution.

7.1.3 "Pre-exposure" and Hydrogen-Charging Results

Although sensitised Type 304 steel is susceptible to hydrogen embrittlement, no "pre-exposure" embrittlement effects were observed in specimens exposed to 120°C steam at 2 bar , or dry steam at 320°C and 1 atmosphere.

Cathodically charging thin foils of the metal with hydrogen did promote microstructural changes. The stresses involved in hydrogen charging were sufficient to induce the $\gamma \rightarrow \alpha$ transformation. In addition to causing plastic deformation of the γ, ε martensite was also formed in the matrix. Shallow intragranular cracks were observed in the charged material. These appeared to grow in <111> directions.

7.2 ACTIVE PATH MECHANISMS

Active path mechanisms include those in which crack progagation is proposed to occur as the result of localised anodic dissolution. Although a variety of theories have been proposed to explain SCC (Section 1.4), the film-rupture (also known as "slip-dissolution") is the most widely invoked active path mechanism. The film-rupture theory (75 ,76) is based upon the rupture of a passive film by localised deformation at the crack tip and the subsequent dissolution of the exposed substrate. The crack walls are protected by a passive film. SCC susceptibility is dependent upon the rate of repassivation of the clean (exposed) material. The dissolution at the crack tip serves to sharpen the crack, thereby increasing the stress and promoting more deformation. By assuming that the crack tip does not repassivate, continuous crack propagation is expected. If the crack tip repassivates, discontinuous cracking occurs. Vermilyea (76, 77) proposed a sequence of events in which dissolution at the crack tip proceeds until repassivation is complete, and then, as the strain in the film increased, the film ruptures, resulting in additional dissolution at the crack tip. The same series of steps is involved in Staehle's model (49, 205), but the rupture of the film is proposed to occur as the result of emergent slip steps caused by plastic deformation in the metal.

This model is generally employed in discussing SCC in passivating solutions, and for intergranular SCC failures. The observation that cracking is enhanced by the application of anodic potentials and inhibited by cathodic potentials is taken as conclusive evidence that an active path mechanism is dominant in SCC. Transgranular SCC, however, is not readily explained by this model. Matching TG SCC fracture surfaces would not be predicted by the film-rupture mechanism, yet they have been observed in a variety of metal/environment systems (87).

From the characterisation of the chromium depletion in regions adjacent to sensitised grain boundaries, and the polarisation behaviour of the "grain boundary composition" Fe-Ni-Cr alloys, it was concluded in this investigation that the Cr- depleted zone was susceptible to preferential (intergranular) dissolution. Since the chromium content of the austenite in equilibrium with the $(Cr, Fe)_{23}C_6$ precipitates is less than 12 wt.%, the tip of an intergranular crack would not repassivate, and continuous cracking would be expected. The fracture mode should be completely intergranular.

The fractographic and SSR results do not support an active path mechanism for SCC propagation. Although the zone adjacent to the sensitised grain boundaries is depleted in chromium, a mixed mode (inter and trans granular) fracture was observed. The results of the controlled potential SSR tests in the 0.01 M H_2SO_4 + 0.002 M NaCl(pH=2) solution indicated that all sensitised specimens failed at lower strains under cathodic polarisation while tests under anodic control only promoted premature failure in the heavily sensitised specimens (72 hours). Only under the most aggressive conditions (pH=1 solution, -140mV SCE) did rapid intergranular failure occur. This anomaly is reconciled with the previous (pH=2) SSR data in that the failure was not a manifestation of SCC, but merely an example of intergranular dissolution. Dissolution proceeded in the absence of an applied stress. The behaviour observed in the pH=2 solution is not predicted by active path models. As the slow strain rate test is a dynamic SCC test, there should be a continuous rupture of any film in the crack tip region by emerging slip steps, and the subsequent exposure of this clean metal to the environment. This type of SCC test should enhance the propagation of cracks occurring by a slip-dissolution mechanism.

The occurrence of striations in specimens which had been stress-corroded under anodic control in pH=2 0.01 M H_2SO_4 + 0.02 M NaCl solution was directly related to the chloride ion concentration of the solution. These intergranular striations have been shown to be indications of discontinuous crack propagation. Vermilyea (77) observed such crack arrest markings in SSR experiments on sensitised Inconel 600 in pH=2.5 H_2SO_4 at 0 V SHE. He interpreted the striations as support for the film-rupture model of SCC. The indications of plastic deformation (fine slip lines) between some striations in this investigation can be explained by Vermilyea's film-rupture model.

It is important to note that this fractography was only observed for SCC specimens tested under an anodic potential and for $\frac{SO_4^{-2}}{Cl^{-1}} < 1$. Curley-Fiorino and Schmid (209), in their investigation of the effect of chloride ions on the passive film formed on type 304 steel, concluded that the $\frac{SO_4^{-2}}{Cl^{-}}$ ratio was important. For $\frac{SO_4^{-2}}{Cl^{-1}} < 1$, under anodic potentials, there was a breakdown of the passive state, with the onset of pitting. This would support the film-rupture mode of crack propagation for solution annealed steels, but does not rationalise the discontinuous cracking in sensitised material.

Although the film-rupture/slip-dissolution mechanism has been widely applied to SCC, the results of this investigation can not be adequately explained by this mechanism. The existence of striations appears to support Vermilyea (76), but it is only that particular fractographic pbservation which could possibly be explained by the film-rupture mechanism. Clearly, another mechanism is operative in the SCC of sensitised Type 304 steel in dilute H_2SO_4+ NaCl solutions.

7.3 HYDROGEN EMBRITTLEMENT MECHANISMS

It has been shown that active path models for IGSCC in dilute H_2SO_4 + NaCl colutions do not adequately explain the SCC results in this investigation. The similarities in mechanical behaviour and fractography of the stress corroded and cathodically polarised SSR specimens strongly indicated that the two types of failure were indeed related. Stress corroded specimens were characterised by intergranular fracture with small regions of "feathery" or cleavage-like fracture. In the cathodically controlled SSR samples, a mixed-mode cleavage-like and intergranular fracture morphology was observed. The existence of the intergranular fracture was related to the degree of sensitisation of the steel, with the most IG fracture associated with long term sensitisation treatments. Unsensitised specimens failed in a transgranular cleavage-like mode under cathodic potentials. This characteristic "feathery" or cleavage-like fracture morphology observed in SCC and HE failures was indicative of hydrogen assisted fracture (87 , 121,125).

The relationship between hydrogen activity and the true strain to failure, and the effect of applied anodic potential strongly suggests that the consideration of a hydrogen embrittlement mechanism to explain the experimental observations is appropriate. The two hydrogen embrittlement models which are applicable to materials exhibiting brittle fracture are : 1) the adsorption mechanism; and 2) the lattice decohesion mechanism.

7.3.1 Hydrogen Adsorption Mechanism

In order for a metal to become embrittled by hydrogen, hydrogen (atomic or ionic) must first be adsorbed by the metal. The adsorption theory attempts to explain the embrittling effect of hydrogen on the basis of a reduction in the surface energy of the material (Section 1.5.1b). This model predicts that hydrogen cracking should be a continuous process.

The absence of crack-arrest markings on the fracture surfaces of specimens tested under cathodic or free corrosion condition in this investigation is consistent with an adsorption mechanism. The lack of such markings, however, does not conclusively prove that crack propagation is continuous. The observed effect of hydrogen activity on true strain to fracture does conform to the hydrogen adsorption model. The existence of striations on the + 0.02 M NaCl solution cannot be explained by this mechanism.

7.3.2 Lattice Decohesion Mechanism

In the lattice decohesion theory, hydrogen is proposed to reduce the cohesive strength of the metal. A critical hydrogen concentration is attained in the plastic zone ahead of the crack tip which is a favourable site for hydrogen accumulation due to the state of stress. Fracture then occurs when the local stress exceeds the interatomic cohesive strength (substantially reduced by hydrogen). This model, discussed in detail in Section 1.5.1a, predicts that crack propagation will be discontinuous.

The dependence of true strain to fracture on pH and hydrogen activity observed in this study is consistent with the decohesion model. When more hydrogen is available to enter the material (i.e. in low pH solutions or under cathodic polarisation), the critical hydrogen concentration ahead of the crack tip should be reached rapidly. The intervals between cracking correspond to periods during which hydrogen accumulates in the region of high triaxial stress. Upon reaching the critical hydrogen concentration in the plastic zone, the crack will advance, but is stopped as it enters the unembrittled metal (crack blunting will occur in austenitic stainless steel).

The observation of striations in specimens tested at -140mV SCE in the 0.01M H_2SO_4 + 0.02 M NaCl solution (increased Cl^- concentration) is indicative of discontinuous crack propagation. The formation of these crack arrest markings is proposed to be post-crack advance dissolution of the clean metal which is exposed to the solution. Dissolution of the metal proceeds as described in Section 5.4, and merely serves to accentuate the discontinuous nature of crack propagation.

Shively et al.(53) have demonstrated that hydrogen absorption and permeation can occur in austenitic stainless steel under anodic polarisation, so it is still possible for the material to fail by hydrogen embrittlement. They observed significant hydrogen permeation in anodically polarised specimens whose surfaces had been previously activated (prior cathodic polarisation). No prior surface activation was required for specimens tested in Cl^- solutions. Only in H_2SO_4 solutions without chloride additions did the hydrogen permeation decrease as the anodic potential was applied. This was the result of complete repassivation of the metal surface.

The absence of striations at lower chloride ion concentrations does not invalidate the decohesion mechanism. The low chloride ion solution (0.002 M NaCl) is less aggressive, so gradual dissolution of the clean (hydrogen-embrittled) metal would be anticipated, the result of which would be a fairly "smooth" fracture surface with corrosion product.

In the free corrosion and cathodic potential SCC tests, there were no indications of crack arrest markings. As in the case of the 0.002 M NaCl pH=2 solution at -140mV SCE, no striations would be expected under these conditions because the clean metal is not readily attacked in the free corrosion condition, and is protected under cathodic polarisation. The high concentration of hydrogen ions in the crack tip region, and the high activity of hydrogen are more favourable for hydrogen entry into the metal than are the conditions during the anodic tests. For the free corrosion and cathodic potential tests, more hydrogen is available to embrittle the steel, so the intervals between crack advance events should be shorter than those under anodic potential SSR tests, i.e. shorter failure times and lower $_f$.

The failure times of the anodically polarised specimens tested in the pH=2 solutions were slightly less than those for specimens tested in free corrosion conditions. The difference can be explained in terms of enhanced crack initiation under anodic potential control.

It is generally agreed that the initiation of SCC is controlled by dissolution (14, 61,210). Pitting may precede cracking. The protective oxide film is attacked and the exposed metal is rapidly dissolved. It is possible for the pits to act as stress concentrators, thus increasing the stress intensity at the base of the pit. In the pit, conditions are favourable for anodic dissolution and hydrogen embrittlement. It has been proposed that the two processes can occur simultaneously (94,124) .

The presence of chloride ions greatly affects the SCC behaviour of austenitic stainless steels. The role of the chloride ions is to breakdown the passive oxide film and prevent repassivation. Scully (197) has postulated that the chloride ions chemisorb to the clean surface, and are then involved in complex ion formation which favours subsequent hydration of the metal and easy electron transfer. The entry of hydrogen into ferrous metals can also be promoted by the addition of chloride ions, as a result of a reduction in the Metal - $H_{ads.}$ bond energy (211).

Clearly, the decohesion mechanism of hydrogen embrittlement is the only mechanism which can explain all of the experimental SCC results. The transition from inter to transgranular (cleavage-like) fracture in the free corrosion and cathodically polarised SSR tests is a definite feature of hydrogen embrittlement failure in this material, and is dependent upon the stability of the austenite. This influence of microstructure (i.e. degree of sensitisation) is discussed separately in the following section.

Hydrogen and Sensitised Austenitic Stainless Steel

It has been demonstrated by the results of this investigation that sensitisation promotes the formation of martensite in the chromium depleted zone adjacent to certain grain boundaries, the relative amount being a function of the particular sensitisation treatment. While this transformation does not alter the electrochemical response of the low chromium metal, the susceptibility of the material to hydrogen embrittlement was significantly increased. The observation that the $\gamma \rightarrow \alpha'$ transformation could be enhanced by plastic deformation indicated that the high stress within the plastic zone associated with a propagating crack would be sufficient to induce the martensitic transformation of the low Cr austenite in the vicinity of the sensitised grain boundaries.

Whether the primary role of the plastic zone in sensitised 304 is to induce the $\gamma \rightarrow \alpha'$ transformation or to enhance hydrogen segregation (as proposed in the decohesion theory) is not known. In sensitised austenitic stainless steel, the preference of the grain boundary as the crack path appears to be dependent upon the existence of grain boundary martensite which is subsequently embrittled by hydrogen.

A recent investigation by Pritcher (205) has dealt with the influence of hydrogen in austenitic stainless steels. It was found that the stacking fault energy decreased by approximately 15% in Type 304L, and ∿ 25% in ype 310 steel after cathodic charging, thereby enhancing the formation of stacking faults and ε martensite. The presence of hydrogen, however, appeared to stabilise the austenite rather than promote the $\gamma \rightarrow \alpha'$ transformation. It was proposed that high concentrations of hydrogen would develop as a result of hydrogen enhanced planar slip (and Suzuki segregation), which would, in turn, lead to localised stress concentrations. The reduction of the fracture stress in the presence of hydrogen was attributed to hydrogen's effect on the electronic structure of the material, i.e. the reduction in the cohesive strength of the metal atoms. Pritcher concluded that highly localised H concentrations at grain boundaries promotes brittle intergranular fracture, while hydrogen accumulation at twin and ε boundaries results in transgranular fracture. The observations of Hanninen and Hakkarainen (125) on the effect of α' in hydrogen embrittlement failures of type 304 stainless steel are in agreement with Pritcher's results. Recent TEM studies of hydrogen-charged 304 and 316 steels by Hänninen, Hakkarainen and Nenonen (127) have demonstrated that preferential cracking occurs at deformation twin boundaries and ε martensite. The results described in Section 6.3 also have shown that intragranular hydrogen cracking can occur in austenite in the absence of α'. Also

Burke et al.(150) have revealed that hydrogen does not affect the M_s significantly, so that α' transformation is not expected to be enhanced by it. Their results, however, did suggest that hydrogen transport by dislocations occurs, with hydrogen accumulating at dislocation obstacles.

Clearly, α' martensite is not a prerequisite for hydrogen assisted fracture.

7.4 PROPOSED MECHANISM FOR SCC OF SENSITISED AUSTENITIC STAINLESS STEEL IN DILUTE H_2SO_4 + NaCl SOLUTIONS

From this research and information in the literature, the following sequence of events is proposed to occur:

In the acidic environment, initial dissolution attack occurs at sensitised grain boundaries as a result of the chromium depletion, leading to the formation of a pit. The pits act as stress concentrators, and, as the stress increases, the grain boundary material is transformed to a narrow band of α' martensite. The acidic solution containing Cl^- ions breaks down the passive film in the pit, thereby permitting hydrogen to enter the metal. Hydrogen entry is also enhanced by the increased hydrogen activity at thecrack tip due to the beneficial effect of the Cl^- ions (211).

Once hydrogen is absorbed and is accumulated in the plastic zone (in which is located the sensitised grain boundary), the strain-induced martensite fractures along the grain boundary, which is the weakest link in the metal. The crack advance, but blunts as it enters the unembrittled material. (Under extremely aggressive conditions -0.01 M H_2SO_4 + 0.02 M NaCl, -140m V SCE - rapid dissolution of the clean metal would now occur, resulting in striation formation .) As the stress increases, hydrogen will preferentially segregate in the plastic zone (particularly in the martensite), and upon attaining the critical hydrogen concentration, the crack advances once again. The transition from inter to transgranular cracking can be explained in view of the results of Hänninen et al. (125,127) in that the austenite or ε martensite may become embrittled. The observation that fracture is predominantly intergranular rather than transgranular in sensitised austenitic stainless steels is dependent upon the existence of α' in the chromium depleted zone. This model is summarised in Figure 7.1.

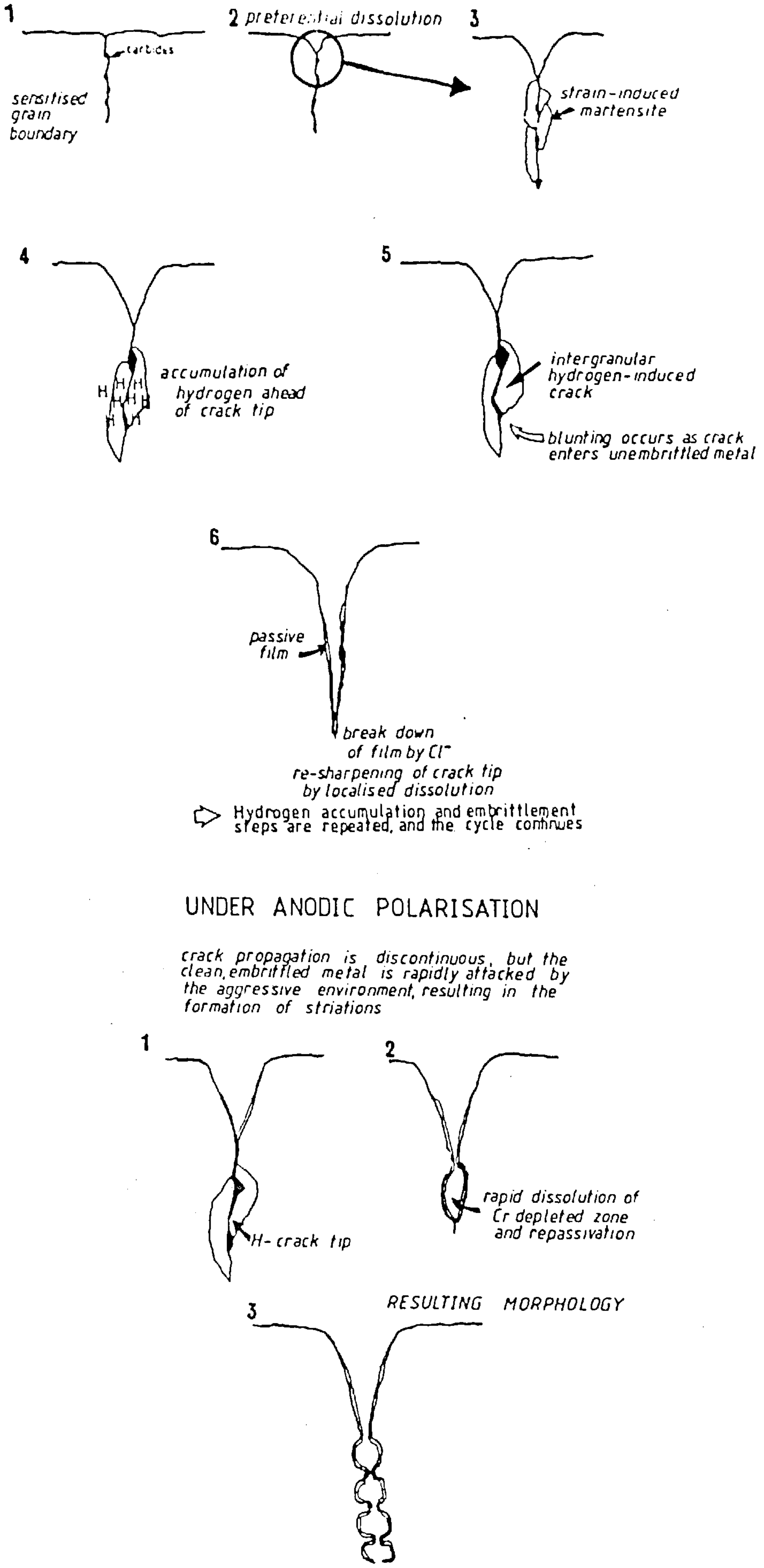

⇨ Hydrogen accumulation and embrittlement steps are repeated, and the cycle continues

crack propagation is discontinuous, but the clean, embrittled metal is rapidly attacked by the aggressive environment, resulting in the formation of striations

Figure 7.1 Schematic Diagram of Proposed Events in the Stress Corrosion Cracking of Sensitised Austenitic Stainless Steel in Dilute H_2SO_4+ NaCl Solutions.

CHAPTER 8

CONCLUSIONS AND SUGGESTIONS FOR FUTURE RESEARCH

8.1 CONCLUSIONS

In this investigation, it has been shown that hydrogen embrittlement is the mechanism of stress corrosion cracking of sensitised type 304 stainless steel in dilute H_2SO_4+ NaCl solutions. Although it is possible for dissolution to occur in these solutions, it appears to be of secondary importance, with the crack advancing as the result of hydrogen embrittlement.

The results of this research are summarised as follows:

1) STEM quantitative microanalytical techniques have been successfully applied to characterise the development of the Cr-depleted zone which accompanies the precipitation of chromium-rich carbides. It has been confirmed that the chromium content in the vicinity of the grain boundary can fall below 12 wt.%.
2) The reduction in chromium content promotes the preferential formation of martensite along some sensitised grain boundaries.
3) No unique solute profile could adequately characterise a particular sensitisation treatment. Profiles were related to the extent of precipitation and nature of the grain boundary. Asymmetric solute profiles were also detected.
4) Stress corroded specimens of sensitised 304 were characterised by intergranular and cleavage-like fracture,the extent of which was related to the degree of sensitisation.

5) As the pH of the solution is increased, the true strain to failure (ductility) also increases.

6) Results of the controlled potential SSR tests have shown that the application of a cathodic potential did not stop stress corrosion, but enhanced failure. The effect of applied anodic potentials was dependent upon the concentration of the solution, with the most acidic solutions favouring intergranular dissolution. The results of the SSR tests in the pH=2 solutions showed that anodic polarisation did not accelerate SCC.

7) Under an anodic potential (-140 mv SCE), heavily sensitised specimens tested in 0.01M H_2SO_4+ 0.02M NaCl solution showed evidence of discontinuous crack propagation in the form of intergranular striations. These were not observed in the 0.002M NaCl solutions, and have been interpreted in terms of the effect of chloride ions on the dissolution behaviour of the metal.

8) Fractographic observations of the SSR-tested specimens, and the SCC behaviour indicates that failure was the result of hydrogen embrittlement.

9) Austenitic stainless steels are not prone to "pre-exposure" embrittlement effects in dry steam at 343°C (1 atm.). 'In-situ' observations in the Gas Reaction Cell in the HVEM did not reveal any preferential reaction of the H_2O vapour with the metal. No H_2 bubble formation was observed at the s sensitised grain boundaries.

10) Cathodically charging sensitised thin foils with hydrogen promoted the $\gamma \rightarrow \alpha' + \varepsilon$ transformation, and resulted in the formation of crystallographic intragranular cracks in the austenite.

All of the results of this investigation are consistent with a hydrogen embrittlement mechanism of SCC in this metal/environment system.

8.2 SUGGESTIONS FOR FUTURE RESEARCH

It has been the aim of this research to provide information regarding the mechanism(s) of SCC in sensitised austenitic stainless steel. There is still a great need for further work in this area. Some possible aspects of this problem to be studied include:

1) Additional tests to extend the a_H vs. ε_f graph, and in particular to provide additional information on the transition region from Dissolution to Hydrogen Embrittlement.
2) To continue the SCC tests in dilute H_2SO_4+ NaCl solutions using fracture mechanics specimens so that crack propagation and K data can be obtained.
3) Striation Formation: study the SCC behaviour at other anodic potentials and other chloride ion concentrations. Does the striation spacing vary with potential and Cl^- ?
4) Strain rate effects on striation formation and spacing.
5) Continue the high temperature steam research using a dynamic straining apparatus so that the protective oxide film would be ruptured, thus enabling hydrogen to interact with the metal. In order to break down the oxide film, Cl^- could be added to the solution.
6) As it has recently been shown by Birnbaum (212) that Ni-H can be studied in the GRC using an H_2 environment, it would be most interesting to examine the behaviour of sensitised 304 in H_2 in the GRC.

7) Microanalytical studies of chromium carbide precipitation at additional temperatures; further research into the asymmetric nature of the Cr depletion.

8) Additional research into the preferential formation of martensite in the chromium depleted zone. What factors are responsible for martensite formation?

ACKNOWLEDGEMENTS

I would like to sincerely thank my supervisor, Dr.F.J. Humphreys for his interest, encouragement, and helpful discussions during the course of this investigation. I am also very grateful to Dr.E.P. Butler for invaluable discussions and expertise (particularly in the areas of precipitation and martensite formation), interest and friendship.

I would like to thank my colleagues in the EM Group over the past three years for their help and friendship, particularly R.A.H. Edwards for stimulating discussions on stress corrosion, and K. Richter for his expertise in STEM and microanalytical techniques.

For valuable discussions and encouragement, I wish to thank J.M. Silcock, and P. Doig (CEGB), E.H.Phelps and A. Loginow (U.S. Steel Research Laboratory).

The excellent typing of Miss V. Collins, and her patience during the compilation of this manuscript are greatly appreciated. Thanks are also due to the Photography Section for their production of the composite micrographs.

The financial support of the U.S. Army Research Office is gratefully acknowledged.

Finally, I would like to thank my fiance, Michael, for his constant encouragement, advice and understanding, without which it would not have been possible to complete this program.

REFERENCES

1. G.M. Gordon, *SCC and HE of Iron Base Alloys* INACE, (1977) p.893.

2. J.Nutting, *JISI*, *207* (1969) p.872

3. S. Floreen, *Met.Rev.*, *13* (1968) p.115

4. R.P.Reed, *Acta Met.*, *10* (1962) p.865

5. P.L. Mangonon, Ph.D. Thesis, U.C. Berkely, 1968

6. P.L.Mangonon and G.Thomas, *Met.Trans.*, *1* (1970) p.1577

7. R.L.Cowan and C.S. Tedmon, *Advances in Corrosion Science and Technology: Vol.3,* ed.M.G. Fontana and R.W.Stachel (Plenum Press, New York) 1973.

8. R.J. Bendure, L.C. Ikenberry and J.H.Waxweiler, *Trans.Met. Soc.AIME*, *221*, (1961) p.1032.

9. E.M. Mahla and N.A. Nielsen, *ASM Trans Quart.*, *43* (1951) p.290.

10. R.Stickler and A.Vinckier, *Corros.Sci.*, *3*, (1963) p.1.

11. V.Cihal and I.Kosova, *Corros.Sci.*, 10 (1970) p.875.

12. R.N. Younger, R.G. Baker and R. Littlewood, *Corros.Sci.*, *2*, (1962) p.157.

13. E.E. Denhard, *Corrosion*, *16* (1960) p.131.

14. H.Hanninen, Licentiate Thesis, Helsinki University of of Technology, 1977.

15. W.E. Berry, E.L.White and W.K. Boyd, *Corrosion*, *29* (1973) p.451.

16. G.J. Theus and J.R. Cels, *Corrosion Problems in Energy Conversion and Generation*, (The Electrochem.Soc., New York) 1974.

17. M.Hishida and H. Nakada, *Corrosion*, *33* (1977) p.403.

18. M.Kowaka and H.Fujikawa, *The Sumitomo Search*, *7* (1972)

19. T. Kondo, Y. Ogawa and H.Nakajima, *Corrosion Problems in Energy Conversion and Generation*, (The Electrochem. Soc., New York) 1974.

20. H.R. Copson, *Physical Metallurgy of Stress Corrosion Fracture* (Interscience, New York) 1959.

21. G.J. Theus and R.W. Staehle, *SCC and HE of Iron Base Alloys,* (NACE, 1977) p.845.

22. T.Murata, E.Sato and H.Okada, Passivity and Its Breadkown on Iron and Iron Base Alloys, ed H.Okada and R.W.Staehle (NACE, 1976) p.186.

23. R.W. Staehle, J.J. Royvela, T.L. Raredon, E.Serrate, C.R.Morin and R.V. Farrar, Corrosion, 26, (1970) p.451

24. R.M. Latanision and R.W. Staehle, Fundamental Aspects of SCC, ed R.W.Stachle (NACE, 1969) p.214.

25. N.A. Nielsen, J.Materials, 5 (1970) p.749

26. P.R. Swann, Memo No.993, U.S. Steel Corp. Research Centre (Oct, 1962).

27. K.C. Thomas, R.Stickler and R.J. Allio, Corros.Sci., 5 (1963) p.71.

28. M.O. Speidel, Corrosion, 33 (1977) p.19

29. M.O.Speidel, Draft Chapters: Stress Corrosion Cracking of Austenitic Stainless Steels, ARPA Handbook on Stress Corrosion Cracking, 1977.

30. B.F. Brown, The Theory of SCC in Alloys, ed. J.C. Scully (NATO, Brussels, 1971).

31. H. Lefakis and W.Rostoker, Corrosion, 33 (1977) p.178.

32. H.Pickering, F.H. Beck and M.G. Fontana, Corrosion, 18 (1962) p.230.

33. J.M. Silcock and P.R. Swann, Mechanisms of Environment Sensitive Cracking of Materials, ed P.R.Swann, F.P.Ford and A.R.C. Westwood (The Metals Society, London, 1977) p.66.

34. J.A. Honkasalo and H.E. Hanninen, Mechanisms of Environment Sensisitive Cracking of Materials, ed. P.R. Swann, F.P.Ford. and A.R.C. Westwood (The Metals Society, London, 1977) p.83.

35. P.R.Rhodes, Corrosion, 25 (1969) p.462.

36. S.W.Dean, Stress Corrosion-New Approaches: ASTM STP 610, ed. H.L.Craig (ASTM, 1976) p.308.

37. W.L. Clarke and G.M. Gordon, Corrosion, 29 (1973) p.1

38. F.P.Ford and M.J.Povich, Corrosion, 35, (1979) p.569.

39. M.R. Louthan, Corrosion, 21 (1965) p.288

40. C.T. Ward, D.L. Mathis and R.W. Staehle, Corrosion, 25 (1969) p.394.

41. G.J. Theus and J.R.Cels, Babcock and Wilcox Report RDTPA- 74-16 (1974)

42. G.Sandoz, C.T. Fujii and B.F. Brown, Corros.Sci., 10 (1970) p.839

43. H.R.Baker, M.C. Bloom, R.N. Bolster and C.R.Singleterry, Corrosion, 26 (1970) P.420.

44. T.Suzuki, M.Yamaha and Y.Kitamura, Corrosion, 29 (1973) p.18.

45. B.E. Wilde, J.Electrochem.Soc., 118 (1971) p.1717

46. H.J. Engell, The Theory of SCC in Alloys, ed. J.C. Scully (NATO, 19) p.86.

47. S.Shimodaira, Passivity and Its Breakdown in Iron Base Alloys (NACE, 1976) p.38.

48. Z. Szklarska-Smialowska and N.Lukomski, Corrosion, 34 (1978) p.177.

49. R.W. Staehle, The Theory of SCC in Alloys, ed.J.C. Scully (NATO, 1971) p.493.

50. T.P.Hoar, The Theory of SCC in Alloys, ed. J.C. Scully (NATO, 1971) p.218.

51. T.P.Hoar and J.G.Hines, JISI, 176 (1956) p.124.

52. J.C. Scully, Fundamentals of Corrosion (Pergamon Press, New York) 1966.

53. J.H. Shively, R.F. Hehemann and A.R. Troiano, Corrosion, 23 (1967) p.215.

54. C.F.Barth, E.A. Steigerwald and A.R.Troiano, Corrosion, 23 (1969) p.353.

55. E.H.Dix, Trans. AIME, 137 (1940) p.137

56. C.F. Barth and A.R. Troiano, Corrosion, 28 (1972) p.259.

57. B.E.Wilde and C.D.Kim, Corrosion, 28 (1972) p.350.

58. C.D.Kim and B.E.Wilde, Corros.Sci., 10 (1970) p.735.

59. H.Hanninen, Doctor of Technology Thesis, Helsinki University of Technology, 1980.

60. M.R.Piggott and A.C. Siarkowski, JISI, 210 (1972) p.901.

61. G.M. Scamans, Ph.D. Thesis, Imperial College of Science and Technology, U.of London, 1974.

62. H.Hanninen, Mechanisms of Environment Sensitive Cracking of Materials, ed. P.R.Swann, F.P. Ford, and A.R.C.Westwood, (The Metals Society, 1977) p.168.

63. J.M. Silcock and P.R.Swann, Environment-Sensitive Fracture of Engineering Materials, ed. Z.A. Foroulis (AIME, 1979)p133.

64. E.C. Bain, R.H. Aborn, and J.J.B. Rutherford, Trans.Amer. Soc.Steel Treating, 21 (1933) p.481.

65. C.D. Tedmon, D.A. Vermilyea and J.H. Rosolowski, J. Electrochem.Soc., 118 (1971) p.192.

67. R.Stickler and A. Vinckier, Trans.ASM., 54 (1961) p.362.

68. K.T. Aust, J.S. Armijo and J.H.Westbrook, Trans.ASM, 59 (1966) p.544.

69. K.T. Aust, J.H.Armijo, E.F.Koch and J.H. Westbrook Trans ASM, 60 (1967) p.360.

70. K.T. Aust, Trans.Met.Soc. AIME, 245 (1969) p.2117

71. J.S. Armijo, Corrosion, 21 (1965) p.235

72. T.P.Hoar, Corrosion, 19 (1963) p.331.

73. D.A. Vermilyea and R.B.Diegle, Corrosion, 32 (1976) p.26.

74. R.B.Diegle and D.A. Vermilyea, Corrosion, 32 (1976) p.353

75. F.A. Champion, Symposium on Internal Stresses in Metals and Alloys (Institute of Metals, 1948) p.468.

76. D.A. Vermilyea, J.Electrochem.Soc., 119 (1972) p.405.

77. D.A. Vermilyea, Corrosion, 29 (1973) p.442

78. J.C. Scully, Environment Sensitive Cracking of Materials, ed. P.R.Swann, F.P.Ford, and A.R.C. Westwood (The Metals Society, 1977) p.7

79. M.Ahlers and E.Riecke, Corros.Sci., 18, (1978) p.21.

80. P.R.Swann and J.D. Embury, High Strength Materials, ed V.Zackay (John Wiley and Sons, 1965) p.327.

81. F.P.Ford and M.Silverman, "Mechanisms of Environmentally Enhanced Cracking in Alloy/Environment Systems Peculiar to Power Generatkon Industries" Contract No.RP 1332-1, First Semi-Annual Report, General Electric Re earch Center (1979).

82. F.P.Ford and M.J. Povich, NACE Corrosion 79- Atlanta, Georgia, (1979) paper 94

66. C. Stawstrom and M. Hillert, JISI, 207 (1969) p. 77

83. F.P.Ford and M.J.Povich, Corrosion, 35 (1979) p.569

84. P.Doig and P.E.J.Flewitt, "An Electrochemical Model for Intergranular Stress Corrosion Cracking in Iron-Nickel Alloys" CEGB Report SSD/SE/R38/77 (1977).

85. P.Doig and P.E.J. Flewitt, Proc.Roy.Soc.A, 357 (1977) p.439

86. P.Doig and P.E.J.Flewitt, "A Theoretical Analysis of Stress Corrosion Crack Growth by Anodic Dissolution CEGB Report SSD/SE/R/80/036 (1980).

87. A.J.Bursle and E.N.Pugh, Environment Sensitive Fracture of Engineering Materials, ed. Z.A. Forousis (AIME, 1979)p.18.

88. A.Ronnquist, Corrosion, 20 (1964) p.110

89. H.H.Uhlig and E.W.Cook, J.Electrochem.Soc., 116 (1969) p.173

90. H.H.Lee and H.H. Uhlig, J.Electrochem.Soc., 117 (1970) p.18.

91. C.Edeleanu, JISI, 173 (1953) p.140.

92. H.Kamide and H.Sugawara, Corrosion, 35 (1979) p.456

93. H.E. Hanninen, Proc.7th Int'l. Congr.on Metallic Corrosion - Oct.1978, Rio de Janeiro (ABRACO, 1979). p.751.

94. A.W.Thompson, Environment Sensitive Fracture of Engineering Materials, ed.Z.A. Foroulis (AIME), (1979) p.379.

95. Hydrogen in Metals, ed. I.M. Bernstein and A.W.Thompson (ASM, 1974).

96. Effects of Hydrogen on the Behaviour of Materials, A.W.Thompson and I.M.Bernstien (AIME, 1976).

97. Second Int'l Congr.on Hydrogen in Metals (Int'l. Assoc.for Hydrogen Energy, 1977)

98. Third Int'l Conf.on Effects of Hydrogen on the Behaviour of Materials: Jackson Lake Lodge, August 1980, (to be published)

99. H.P. van Leeuwen, ref. 96., p.480.

100. C.L.Briant, Met.Trans., 9A (1978) p.731.

101. C.D.Kim and B.E. Wilde, J.Electrochem.Soc., 118 (1971) p.202.

102. T.Toya, Prog.Theoret.Phys.Kyoto Suppl, 23 (1963) p.250.

103. F.E. Fujita, in ref. 97, p.2B$_{10}$

104. A.R.Troiano, Trans.AIME, 52 (1960) p.54.

105. G.M.Boyd, Eng.Fract. Mech., 4 (1972) p.459.

106. G.M.Gilpin, D.H.Paul, S.K.Asunmaa and N.A. Tiner, Advances in Electron Metallography: ASTM STP 396 (ASTM, 1966) p.7.

107. R.A.Oriani and P.H.Josephic, Scripta Met., 6 (1972) p.681.

108. C.J.McMahon and J.R. Rellick, Met.Trans., 5 (1974) p.2439.

109. I.M. Bernstein, R.Garber, and G.M. Pressouyre, ref.96,p.37.

110. C.St.John and W.W. Gerberich, Met.Trans., 4 (1973) p.589.

111. W.W. Gerberich and C.E. Hartbower, Fundamental Aspects of Stress Corrosion Cracking (NACE, 1969) p.420.

112. H.P.van Leeuwen, Corrosion, 29 (1973) p.197.

113. J.R. Rice, ref.96, p.455.

114. N.J.Petch and P.Stables, Nature, 169 (1952) p.842.

115. R.B. Heady, Corrosion, 33 (1977) p.441.

116. J.R. Rice, Jap.Soc.for Strength and Fracture of Materials, 1 (1966) p.309.

117. R.B. Heady, Corrosion. 34 (1978) p.303

118. H.H. Johnson, J.G. Mortlet, and A.R. Troiano, Trans.Met.Soc. AIME, 234 (1958) p.528.

119. K. Sieradzki and P.Ficalora, Scripta Met., 14 (1980) p.641.

120. C.M.Ransom and P.J.Ficalora, Met.Trans., 11A (1980) p.801.

121. D.Eliezer, D.G. Chakrapani, C.J.Altstetter, and E.N.Pugh, Met.Trans., 10A (1979) p.935.

122. S.S. Birley and D.Tromans, Corrosion, 27 (197) p.63.

123. R.A. McCoy, ref. 95, p.169.

124. A.W. Thompson, ref. 95, p.179.

125. H.Hanninen and T.Hakkarainen, Corrosion, 36 (1980) p.47.

126. M.L.Holzworth and M.R.Louthan, Corrosion, 24 (1968) p.110

127. H.Hanninen, T.Hakkarainen, and P.Nenonen, ref.98, (to be published).

128. D.A.Vaughan, D.I. Phalen, C.L. Peterson and W.K.Boyd, Corrosion, 19 (1963) p.315t.

129. D.A. Vaughan and D.I.Phalen, Metals Engr.Quart (ASM), (1965) p.39.

130. A.Szummer and A.Janko, Corrosion, 35 (1979) p.461.

131. A.W. Thompson, ref.96, p.467.

132. A.S. Tetelman, ref.95, p.17.

133. F.E.Fujita, J.Jap.Inst.Metals, 40 (1976) p.230.

134. K.Kamachi, K.Akiyoshi and H.Hayashi, ref.97, p.2C$_{13}$

135. J.P.Hirth, Met.Trans., 11A (1980) p.861.

136. H.K.Birnbaum, Environment Sensitive Fracture of Engineering Materials, ed. Z.A. Foroulis (AIME, 1979) p.326.

137. J.K. Tien, ref. 96, p.309.

138. M.H. Whiteman and A.R. Troiano, Corrosion, 21 (1965) p.53.

139. H.H. Johnson, ref.95, p.35.

140. G.Caskey, Scripta Met., 11 (1977) p.1077.

141. D.A. Vaughan, D.I.Phalen, C.L. Peterson, and W.K.Boyd, Corrosion, 19 (1963) p.315t.

142. L.H.Keys, A.J. Bursle, H.R. Kemp and K.R.L.Thompson, ref.97, p.3f$_6$.

143. J.Green, H.Hayden, and W. Montague, ref.96, p.200.

144. M.R. Louthan, Rev. Coat.and Corr., (1978) p.103.

145. J.Kolts, Stress Corrosion-New Approaches: ASTM STP 610, ed H.L. Craig, Jr. (ASTM, 1976) p.366.

146. A. Szummer and A. Janko, Corrosion, 35 (1979) p.461.

147. K.Kamachi, M.Oka and M.Touge, Proc.1st Int'l Symp. on New Aspects of Martensitic Transformation: Trans JIM, 17 (1976) p.309.

148. H.Mathias, Y.Katz and S.Nadiv, ref.98 (in press).

149. C.Paes de Olivera, M.Aucouturier and P.Lacombe, Corrosion, 36 (1980) p.53.

150. J.Burke, A.Jickels, P.Maulik and M.I.Mehta, ref.96, p.102.

151. J.D.Hartson and J.C.Scully, Corrosion, 25 (1960) p.493.

152. Stress Corrosion Cracking - The Slow Strain Rate Technique ASTM STP 665, ed. G.M.Ugiansky and J.H.Payer (ASTM, 1979).

153. L.Montgrain, Ph.D. Thesis, Imperial College of Science and Technology, U.of London (1973).

154. R.Alani, Ph.D. Thesis, Imperial College of Science and Technology, U.of London (1976).

155. L.Christodoulou, Ph.D. Thesis, Imperial College of Science and Technology, U.of London (1980).

156. P.R. Swann, *Proc.5th European Congress on Electron Microscopy*, (1972) p.330.

157. H.M. Flower, *J.Microscopy*, *97* (1973) p.171.

158. H.M. Flower, *High Voltage Electron Microscopy*, ed.P.R.Swann C.J.Humphreys and M.J.Goringe (Academic Press, 1974) p.383.

159. E.P.Butler, *Rep.Prog.Physics*, *42* (1979) p.883.

160. P.Duncumb, *Proc.Symp.on X-ray Optics and X-ray Microanalysis (Stanford, 1963) p.431*

161. P.Doig, D.Lonsdale, and P.E.J.Flewitt. The Spatial Resolution of X-ray Microanalysis in the Scanning Transmission Electron Microscope" CEGB Report (draft)

162. P.Bovey, I.Wardell and P.M.Williams, *Proc.8th Int'l Conf. on X-ray Optics and Microanalysis / 12th Annual Conf.of the Microbeam Soc.*, (Boston, 1977) p.11 A

163. R.G. Faulkner and K.Norrgaird, *X-ray Spectrometery*, *7* (1978) p.184.

164. D.F.Kyser and R.H.Geiss, *Proc.8th Int'l Conf.on X-ray Optics and Microanalysis/ 12th Annual Conf.of Microbeam Soc. (Boston, 1977) p.110A*

165. S.J.B. Reed, *Link System Manual for Energy Dispersive Analysis Dispersive Analysis Systems* p.26.

166. J.V.P.Long, *Physical Methods in Determinative Mineralogy, ed. J.Zussman (Academic Press, 1977) p.273.*

167. P.J. Statham, *X-ray Spectrometery*, *5* (1976) p.154.

168. P.J. Statham, *X-ray Spectrometry*, *5*, (1976) p.16.

169. N.G.Ware and S.J.B. Reed, *J.Phys.E.*, *6* (1973) p.286.

170. E. Lifshin, *Proc. 9th Annual Conf. of the Microbeam Analysis Soc.*, (Ottawa, 1974) p.53A.

171. T.A.Hall, *Physical Techniques in Biological Research*, *1A* (Academic Press, 1971) p.157.

172. J.Philibert and R.Tixier, *Proc. 8th Nat'l. Conf.on Electron Probe Analysis* (1973) p.27.

173. J.Bently and E.A.Kenik, *Scripta Met.*, *11* (1977) p.261.

174. N.J.Zaluzec, J.B. Woodhouse and H.L.Fraser, *Scripta Met.*, *11* (1977) p.257.

175. J.I. Goldstein, J.L.Costley, G.W. Lorimer and S.J.B.Reed, SEM/1977, 1 ed. O.Johari (IITRI, 17) p.315.

176. P.L.Morris, M.D.Ball and P.J.Statham, Inst.Phys.Conf.Series No.52, (1980) p.413.

177. G.W. Lorimer, Proc.8th Int'l Conf.on X-ray Optics and Microanalysis/ 12th Annual Conf. of Microbeam Soc. (Boston, 1977) p.1 A.

178. C.Nockolds, M.J.Nasir, C.Cliff and G.W. Lorimer, Inst.Phys. Conf.Series No.52, (1980) p.417.

179. B. Bengtsson and K.E.Easterling, SEM/1978, 1 (1978) p.655.

180. G.Cliff and G.W. Lorimer, J.Microscopy, 103 (1975) p.203.

181. G.W. Lorimer, Private Communication, 1979.

182. P.Doig and P.E.J. Flewitt, J.Microscopy, 112, (1977) p.257.

183. N.J.Zaluzec and H.L.Fraser, 8th Int'l Conf.on X-ray Optics and Microanalysis/12th Annual Conf.of Microbeam Analysis Soc. (Boston, 1977) p.112A.

184. G.Cliff, Private Communication, 1980.

185. U.E.Wolff, Trans.TMS-AIME, 236, (1966) p.19.

186. L.K.Singhal and J.W. Martin, Trans Met.Soc. AIME, 242 (1968) p.814.

187. C.S. Pande, M.Suenaga, B.Vyas, H.Isaacs and D.F.Harling, Scripta Met., 11 (1977) p.140.

188. P.Rao and E. Lifshin, Proc.8th Int'l Conf.on X-ray Optics and Microanalysis/12th Annual Conf. of Microbeam Soc. (Boston, 1977) p.118.

189. E.P.Butler, Private Communication, 1980.

190. M.H.Lewis and B.Hattersly, Acta Met., 13 (1965) p.1159.

191. M. Hillert and R. Lagneborg, J.Mat.Sci., 6 (1971) p.208.

192. K.T. Aust, Surfaces and Interfaces I ed, J.J. Burke, N.L. Reed, and V. Weiss (Syracuse U. Press, 1967) p.431

193. E.P.Butler, M.G. Lackey and K.B. Guy, Proc.6th Int'l Conf. on HVEM ed. P.Brederoo and J.van Landuyt (SECEMF, 1980) p.306.

194. F.Lecroisey and A.Pineau, Met. Trans, 3 (1972) p.387.

195. T.Suzuki, H.Kojima, K.Suzuki, T.Hashimoto, S.Koike and M. Ichihava, New Aspects of Martensitic Transformatiion: Trans.JIM., 17, (1976) p.

196. W.Y.C. Chen and J.R. Stephens, Corrosion, 35 (1979) p.443.

197. J.C. Scully, Corros.Sci, 8 (1968) p.513.

198. J.A. Davis and B.E. Wilde, J. Electrochem. Soc., 117 (1970) p.1348.

199. ASTM Powder File

200. J.E. Reinoehl and F.H. Beck, Corrosion, 25 (1969) p. 233.

201. C.L. Briant, Scripta Met., 12 (1978) p.541

202. L. Christodoulou and H.M. Flower, Inst. Phys. Conf. Series No. 52, (1980) p.313.

203. S.H. Bush and R.L. Dillon, SCC and HE of Iron Base Alloys, (NACE,1977) p.61.

204. D. Eliezer, ref. 98, (in press)

205. P.D. Pritcher, Ph.D. Thesis, University of Wales, 1979.

206. M.R. Louthan and R.G. Derrick, Corros. Sci., 15 (1975) p.565.

207. H.E. Hanninen and T. Hakkarainen, Met. Trans.,10A (1979) p.1196.

208. R.W. Staehle, SCC and HE of Iron Base Alloys (NACE,1977) p.180.

209. M.E. Curley-Fiorno and G.M.Schmid, Corros. Sci., 20 (1980)p.313.

210. H.E. Hanninen, Int'l Met. Rev., No.3 (1979) p.85.

211. J. McBreen and M.A. Grenshaw, Fundamental Aspects of SCC, ed. R.W. Staehle (NACE,1969) p.51.

212. H. Birnbaum, ref.98, (in press)